UNIVERSITÀ
DEGLI STUDI
FIRENZE

DOTTORATO DI RICERCA IN
FISICA E ASTRONOMIA

CICLO XXX

COORDINATORE Prof. Raffaello D'Alessandro

Measurement of the cosmic-ray electron flux with the CALET experiment: simulation studies and data analysis.

Settore Scientifico Disciplinare FIS/04

Dottorando
Dott. Lorenzo Pacini

Tutori
Prof. Oscar Adriani

Dott. Nicola Mori

Coordinatore
Prof. Raffaello D'Alessandro

Anni 2014/2017

Ai miei genitori e ai miei nonni.

Contents

Introduction

Cosmic-rays (CRs) are one of the most important areas of current research on astroparticle physics. Direct measurements of CRs are important to understand the sites and the processes of acceleration and propagation in the interstellar medium of high-energy particles (up to 10^{15} eV). For example, electrons and positrons in CRs suffer from significant energy losses due to radiative emission along their path to Earth, so detailed measurements of the high-energy electron+positron (hereafter "electron") spectrum and of its anisotropy can provide information about nearby CR sources. The electron spectrum may also exhibit features from Dark Matter (DM) annihilation, as predicted by some theoretical models, and it is a viable channel for indirect DM searches.
The CALorimetric Electron Telescope (CALET) is a Japanese-led international space mission promoted by JAXA (Japanese AeroSpace Agency) in collaboration with the Italian Space Agency (ASI) and NASA. The apparatus was launched to the International Space Station on 19th August 2015. Its main objective is to perform precise direct measurements of the electron cosmic-ray spectrum in the energy region above 1 TeV; other scientific objectives are to measure the spectra of hadrons from proton to iron and above up to several hundreds TeV and to detect gamma ray emissions up to 10 TeV with a very good energy resolution. The detector consists of a deep homogeneous calorimeter (about 27 X_0, where X_0 indicates the radiation length), a sampling imaging calorimeter (3 X_0) and a charge detector. The on-orbit commissioning phase was successfully completed in the first days of October 2015, and CALET is now in science operation mode for a first initial period of two years with a target of five years.
In this Ph.D. thesis a preliminary version of the event reconstruction and the data analysis procedures used for the measurement of the electron spectrum are described. A brief review of the galactic CR physics, with the most recent measurements of the charged CR, is described in §1. The CALET experiment and its main scientific goals are

described in §2. In §3 the implementation and the validation of the complex geometry of the CALET detector within the Monte Carlo (MC) simulation based on GEANT4 package is discussed. A comparison with different MC codes is also presented. The data analysis developed for this Ph.D. thesis is described in §4. An evaluation of the performance of the described analysis techniques obtained with different MC simulations is presented. A preliminary validation of the MC simulation, which is based on comparisons with fight data, and an evaluation of the systematic errors due to the possible effects of physics processes that are not perfectly simulated are also discussed. Finally, the first published measurement of the electron flux by the CALET collaboration [88] is presented.

Chapter 1

The CALET scientific background: the galactic cosmic-ray physics

The discovery of CRs is commonly dated 1912 and attributed to Victor Hess, who conducted a series of experiments based on electroscopes. An electroscope discharges when exposed to a charged radiation coming e.g. from radioactive material. On ground, the discharge also happens when no radioactive elements are present inside the electroscope shielding: this suggests the presence of some penetrating background radiation at sea level. The open question about the terrestrial or extraterrestrial origin of such radiation was answered in 1912 when Victor Hess measured the rate of discharge in the atmosphere at an altitude of 5300 meters by using balloon flights. The results clearly showed that the electroscope discharge rate increased with height: it was then originated by a radiation coming from space.

After the discovery of CRs, a long debate about the composition of this radiation started: R.A. Millikan, who used for the first time the expression "cosmic rays", hypothesized that the radiation was due to extraterrestrial gamma rays produced during the formation of helium nuclei in the interstellar space. In 1927, J. Clay found that the CR abundance at sea level depends on the latitude. This feature was attributed to the interaction of charged primary CRs with the geomagnetic field. In 1932 Compton verified the Rossi prediction of the so called East-West effect: as CRs are mainly positively charged particles, a difference between the intensity of the radiation arriving from the East and the West is expected, again due to the interaction with the geomagnetic field.

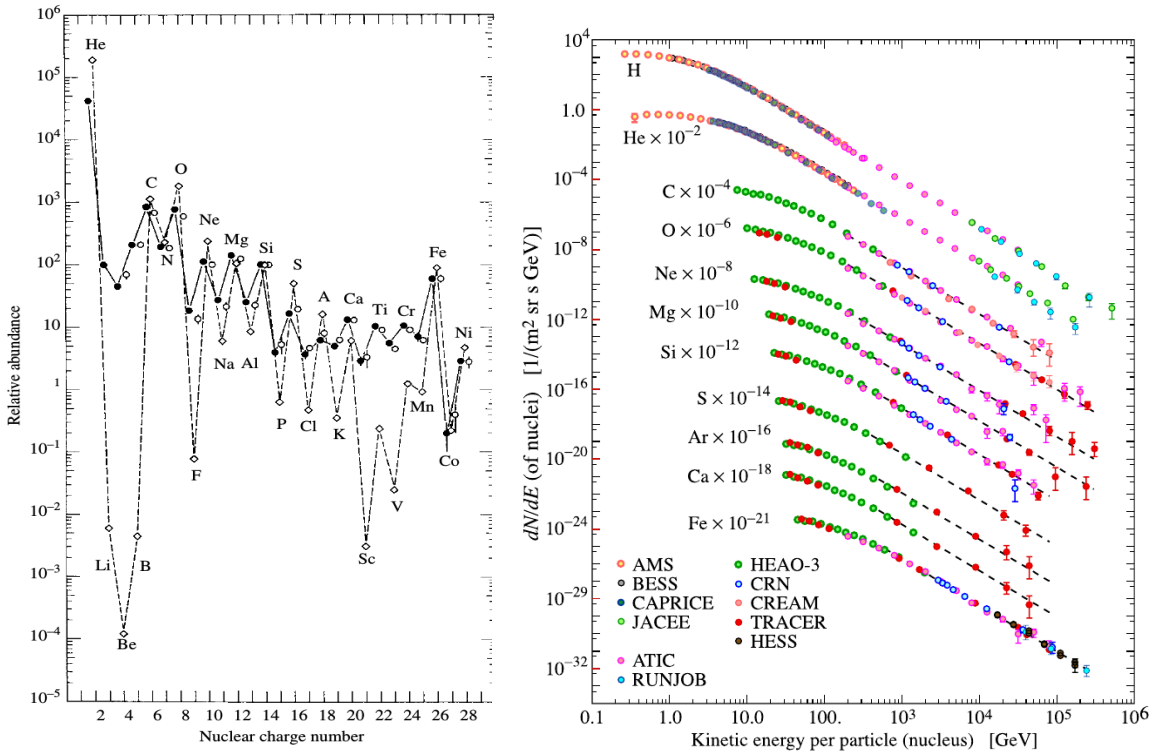

Figure 1.1. *Left: relative nuclei abundance with respect to carbon in CRs (solid line) compared with the relative abundance in the solar system (dashed line). The carbon abundance is assumed equal to 1000 [1]. Right: fluxes of the most abundant nuclei in CRs as a function of the energy per nucleon measured by different experiments [1].*

This chapter presents a brief description of the most important items of the modern CR physics focusing on the theoretical models and experimental measurements related to the CALET main objectives. In the following section the most important well-known CR measurements are presented, while some simplified theoretical models which explain these results are discussed in §1.2, §1.3 and §1.4. Finally, in §1.5 some recent measurements that open new interesting questions about the CR physics are discussed.

1.1 Cosmic rays: a general overview

The composition of CRs observed at the Earth depends on the energy but the most abundant charged species are protons ($\sim$ 85%), helium nuclei ($\sim$ 10%), electrons ($\sim$ 1%) and nuclei heavier than helium (few percent). There is also a very small portion ($\leq$ 0.1%) of positrons and antiprotons. Neutral particles consist of gamma rays, some of which can be identified as coming from point sources in the sky, and of neutrinos and

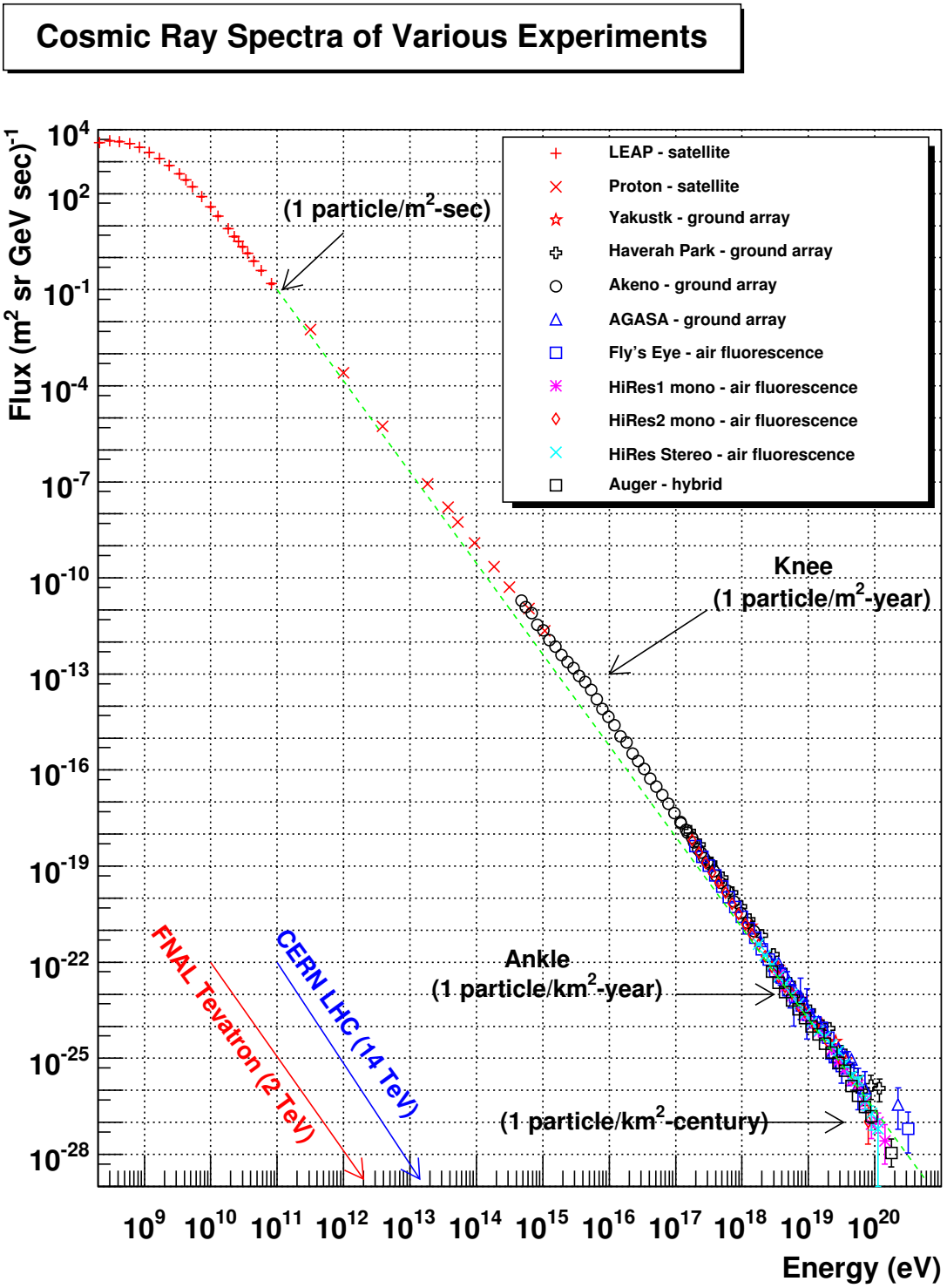

Figure 1.2. *All-particle CR flux as a function of the kinetic energy measured by different experiments [1].*

antineutrinos. The chemical composition of the CR nuclei exhibits remarkable similarities to the solar system abundances, but it also shows some significant differences as shown in fig. 1.1. The biggest differences between the cosmic and solar abundances are in Li, Be, and B. These elements are many orders of magnitude more abundant in CRs than in solar system material since they are essentially not produced in stellar nucleosynthesis [2] and their abundance in CRs is mainly due to spallation of carbon, oxygen and heavier nuclei as they traverse the interstellar medium, as discussed in §1.3.

Fig. 1.2 shows the CR all-particle spectrum ($\Phi(E)$) measured by different experiments: this is defined as the number of particles (dN) reaching the Earth per unit time (dt), surface (ds), solid angle ($d\Omega$), and energy (dE). For low energies, up to about few GeV per nucleon, the spectrum varies over time: experimental measurements (e.g. [3]) show that the low-energy CR abundance is related with the solar activity, increasing during periods of low activity. Above this low-energy region, up to 10^{15} eV, the all-particle spectrum is well approximated by a single power law:

$$\Phi(E) = \frac{dN}{dE \cdot dt \cdot ds \cdot d\Omega} = K \cdot \left(\frac{E}{1\ \mathrm{GeV}}\right)^{\alpha}, \tag{1.1}$$

where α is known as the *spectral index* and has a value of ~ -2.7 at these energies. Measurements of the CR spectrum with ground experiments show that it becomes suddenly steeper and the composition progressively heavier in the 10^{15} eV region [4]. This feature is known as the "knee", a possible common explanation of this structure is discussed in §1.2. The spectrum above the knee has a spectral index $\alpha \simeq -3.1$ but in the region of $5 \cdot 10^{18}$ eV another spectral structure known as the "ankle" is present and the spectral index decreases again to $\alpha \simeq -2.7$. Finally, for energies above $5 \cdot 10^{19}$ eV, there is a spectral cut-off, commonly associated to the GZK effect [5][6] due to the scattering of CR protons off the photons of the cosmic microwave background radiation (CMB). The spectra of the individual nuclear species as a function of the kinetic energy per nucleon (commonly measured in GeV/n) for the most abundant species are shown in the right panel of fig. 1.1. These spectra feature similarities with the all-particle spectrum and above 100 GeV/n can be approximated with a single power law with a spectral index ~ -2.7; see section 1.5.1 for a more detailed description of the recent measurements of the individual proton and helium spectra.

1.2 Acceleration mechanism in SuperNova Remnants

The origin of CRs is one of the most outstanding questions for the interpretation of the CR measurements. It is currently believed that particles with energy below the knee are probably accelerated by Galactic sources and the most quoted sources are the SuperNova Remnants (SNRs). The first motivation (explained by Baade and Zwicky in 1934) is the balance between the energy required for the CR acceleration and the energy provided by SN explosions. The kinetic energy density (ρ_E) of CRs above an energy $E_0 \sim 3$ GeV can be calculated using these values for the parameters of eq. 1.1 [8]:

$$K = 3.01 \ \frac{\text{particles}}{\text{cm}^2 \text{ sr GeV s}}; \ \alpha = -2.68.$$

The kinetic energy density is then:

$$\rho_E = \frac{1}{c} \int_{E_0}^{\infty} E\Phi(E) dE d\Omega \simeq 1 \text{ eV/cm}^3,$$

where c is the speed of light. By assuming galactic CR sources are uniformly distributed in the galaxy and a galaxy volume of $V_G \sim 5 \cdot 10^{66}$ cm^3, the total CR energy in the galaxy is $E_{CR} \sim 8 \cdot 10^{54}$ erg. As a first approximation, the CR escape time from the galaxy is $\tau_{esc} \sim 10^7$ years $\sim 3 \cdot 10^{14}$ s (see §1.3), which gives an energy loss rate of:

$$W_{CR} = \frac{E_{CR}}{\tau_{esc}} \sim 3 \cdot 10^{40} \text{ erg/s}.$$

A typical SN explosion with a mass equal to 10 solar masses releases about 10^{51} erg [7] of kinetic energy in the form of a shock wave. The expected rate of SN explosions is about 3 per century; assuming the CRs are accelerated by shock waves with an efficiency ϵ, the power transferred to the CRs is:

$$W_{SN} = \epsilon \cdot 10^{42} \text{ erg/s}.$$

In order to get $W_{CR} = W_{SN}$ an efficiency ϵ of few percent is required. This value of efficiency is consistent with the most common models related to the acceleration of charged particles in SN shock-waves [7]. In the following paragraphs, a simplified calculation of the expected CR spectrum ejected by the SNRs is described in order to compare the expected and experimental spectra.

Charged particles can be accelerated in SNRs thanks to the strong magnetic field surrounding the SN and the first efficient mechanism that describes the acceleration of charged particles in strongly magnetized cloud was proposed by Fermi in 1949 and is named *"The Second-Order Fermi Acceleration Mechanism"* [9]. This process is based on the scattering of the particle with magnetic field irregularities superimposed to a constant high magnetic field. A particle moving in a constant magnetic field B_0 parallel to the $\hat{z}$ direction rotates in the xy plane with a typical Larmor radius

$$r_L = \frac{pc}{ZeB_0},$$

where p is the momentum of the particle, c is the speed of light, Ze is the charge of the particle. The momentum in the $\hat{z}$ direction is conserved. If a small perturbation (ΔB) of the constant magnetic field B_0 is present the direction of the particle velocity changes according the following equation:

$$sin(\theta) \simeq sin(\theta_0)\sqrt{\frac{B_0 + \Delta B}{B_0}},$$

where θ_0 and θ are the starting and final values of the angle between the particle velocity and the magnetic field vector (see [11] for a complete calculation of this equation). Since the θ angle increase with an increasing magnetic perturbation, the particle can reverse the direction of its motion through multiple scattering off the perturbations. This simplified approach shows that is possible for a charged particle to be "reflected" by strong magnetic perturbations, which can behave like"magnetic mirrors". Furthermore, the distribution of the direction of charged particles in regions with strong magnetic field irregularities becomes isotropic and independent with respect to the initial trajectory [7].

Consider a particle with velocity $\vec{v}$ that collides with a magnetized cloud with velocity $\vec{u}$ which behaves as a magnetic mirror. The cloud velocity is assumed parallel to the direction $\hat{x}$. The energy E' and the momentum ${p_x}'$ in the reference frame in which the cloud is at rest is related to the energy E and the momentum p_x in the reference of the observer by the relations:

$$E' = \gamma(E + up_x); \quad {p_x}' = \gamma\left(p_x + \frac{u}{c^2}E\right),$$

where γ is the Lorentz factor. By assuming that the collisions are elastic, the momentum in $\hat{x}$ direction after the collision is $= -p_x{}'$ while the energy remains E'. The energy in the observer reference frame after the collision (E^*) is:

$$E^* = \gamma(E' - u(-p_x{}')) = \gamma^2 \left[(E + up_x) + u\left(p_x + \frac{u}{c^2}E\right)\right].$$

By using the relativistic relation between the momentum and the energy:

$$\frac{p_x}{E} = \frac{v}{c^2}\cos(\theta),$$

where θ is the angle between the particle and the cloud velocity, the previous equation becomes:

$$E^* = \gamma^2 E\left[1 + 2u\frac{v\cos(\theta)}{c^2} + \frac{u^2}{c^2}\right]. \tag{1.2}$$

For a not-relativistic cloud ($u << c$) one can approximate $\gamma \simeq 1 + (u/c)^2$, and thus the energy gain ($\Delta E = E^* - E$) is:

$$\Delta E = \left[2\frac{uv\cos(\theta)}{c^2} + 2\left(\frac{u}{c}\right)^2\right]E.$$

For an isotropic particle flux the first term is averaged to 0 and the final energy gain is proportional to the square of the cloud velocity u divided by the speed of light c: since $u << c$ the energy gain is small. Actually, the particle gains energy in head-on collisions ($cos(\theta) > 0$, eq. 1.2) while it loses energy in catching collisions ($cos(\theta) < 0$).

A more efficient process is obtained when a particle is accelerated in shock waves because all the collisions are head-on. As a simplified model, consider an infinite, planar shock wave which propagates with velocity v_s in a plasma treated as a simple mono-atomic fluid. By using the conservation of mass, momentum and energy across the shock, if the Much number of the shock is $M = (v_s/c_s) >> 1$, where c_s is the speed of sound in the fluid, the following equation is valid [7]:

$$\frac{\rho_2}{\rho_1} = \frac{u_1}{u_2} = 4,$$

where ρ_2, ρ_1 are the mean density of the down-stream and the up-stream material respectively and u_2, u_1 are the velocities. The mean relative velocity of the up-stream medium with respect to velocity of the sock front is equal to $-v_s$; thus according to the

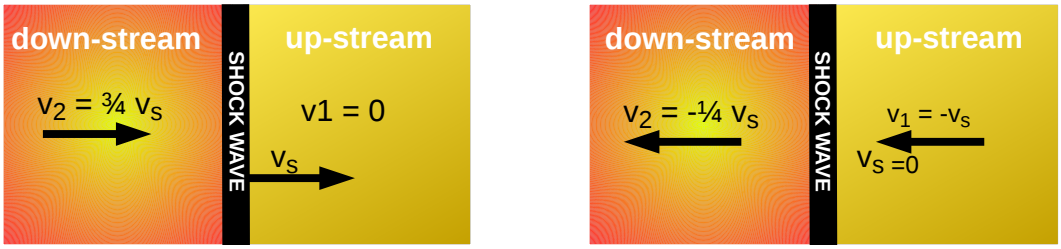

(a) *Up-stream reference frame* (b) *Shock wave reference frame*

Figure 1.3. *Schematic representation of a parallel shock wave (black vertical line) in a plasma with Mach number >> 1. The velocity v_2 of the down-stream (left), the velocity v_1 of the up-stream (right) and the velocity of the shock wave v_s values are calculated with the approximations described in section 1.2 for two different reference frames: the up-stream reference frame (image a) and the shock wave reference frame (image b).*

previous equation, the down-stream mean relative velocity is $-\frac{1}{4}v_s$, since the material in this plasma region is accelerated by the shock wave itself.

CRs are treated as test particles in the scheme described above, which is schematically shown in fig. 1.3. Since the particle direction is randomized due to the scattering with the magnetic field irregularities a particle from the upstream can collide with the down-stream across the shock wave. The collision is head-on and the relative velocity of the down-stream with respect to the up-stream is $u_2 - u_1 = (3/4)v_s$. The same argument is also valid for a particle in the down-stream that collide with the up-stream. Since the collisions are head-on only, when integrating eq. 1.2, the term $2E\left(\frac{u}{c}\right)^2$ is negligible. In an isotropic distribution with $\cos(\theta) > 0$ (head-on collisions) the average cosine angle is $< \cos(\theta) >= 2/3$ and the mean energy gain per shock crossing fro a relativistic particle ($v \sim c$) is:

$$< \Delta E >= \left(\frac{4}{3}\frac{(3/4)v_s}{c}\right) < E >= \frac{v_s}{c} < E > . \tag{1.3}$$

In this case the energy gain is higher than in the previous model because it is proportional to (v_s/c) instead of $(v_s/c)^2$; this acceleration process is named *"The First-Order Fermi Acceleration Mechanism"* [10]. For each collision between the particle and the shock-wave the particle energy increases until it escapes from the acceleration region. This mechanism is known as the "*diffusive shock acceleration*". The escape probability P_{esc} of a particle in the down-stream is constant with time and energy as a first approximation and for an isotropic distribution of relativistic particles is [12]

$$P_{esc} \simeq \frac{v_s}{c} \tag{1.4}$$

By using equation 1.3, after k cycles, the energy of a particle with the starting energy equal to E_0 is

$$E = E_0 \left(1 + \frac{v_s}{c}\right)^k .$$

The number of particle N with energy greater than E after k cycles is:

$$N = N_0(1 - P_{esc})^k = N_0(1 - \frac{v_s}{c})^k,$$

where N_0 is the starting number of particle with energy greater than E_0. The k parameter can be removed from the previous two equations:

$$N = N_0 \left(\frac{E}{E_0}\right)^{\frac{\ln(1-v_s/c)}{\ln(1+v_s/c)}} .$$

The expected integral flux of charged particles accelerated by the interaction with shock waves is a single power law $N \propto E^{\alpha_{int}}$ where

$$\alpha_{int} = \frac{\ln(1 - v_s/c)}{\ln(1 + v_s/c)}.$$

The expected spectrum for a non-relativistic shock ($v_s << c$) can be calculated by using the following approximation:

$$\alpha_{int} \simeq \frac{-v_s/c}{+v_s/c} = -1.$$

The differential flux ejected by this kind of CR sources (here indicated with $\phi_{source}(E)$) is related with the integral flux with the following integral:

$$N = \int_E^\infty \phi_{source}(E')dE',$$

then:

$$\phi_{source}(E) \propto E^{\alpha_{diff}},$$

where $\alpha_{diff} = \alpha_{int} - 1 = -2$. This is one of the most important results of the diffusive shock acceleration model: as discussed in §1.1, the all-particle spectrum (and the nuclei individual spectra too) can be approximated with a single power law up to the knee region. The discrepancy between the spectral index observed at the Earth (about -2.7) and the expected spectral index of the ejected spectrum can be explained tak-

ing into account that particles accelerated by galactic sources undergo several physical processes during their travel to the Earth that modify the injection spectrum. See §1.3 for a more detailed discussion.

Another considerable result is the maximum energy achieved with the described acceleration process. This is related to the finite extent in time and space of the acceleration process. Here a simplified derivation of this important parameter is described; a more complete treatment is explained in several theoretical works, e.g. [13]. Using the equation 1.3 the energy gain per unit time dE/dt can be approximated with:

$$\frac{dE}{dt} = \frac{v_s}{c}\frac{E}{T_{cycle}},$$

where T_{cycle} is the mean time interval between two collisions of the particle with the shock-wave. During the diffusion in the magnetic field the particle is confined in a region with dimensions of the order of the Larmor radius r_L so T_{cycle} can be approximated with:

$$T_{cycle} \sim \frac{r_L}{v_s} = \frac{E}{ZeBv_s}.$$

The maximum energy E_{max} is:

$$E_{max} \simeq \frac{dE}{dt}T_{SNR} = \frac{v_s^2 ZeB}{c}T_{SNR},$$

where T_{SNR} is the duration of the shock. The order of magnitude of T_{SNR} is about 10^3 years [14], the galactic magnetic field $B \sim 4 \cdot 10^6$ Gauss, the velocity of the shock $v_s \sim 10^{-2}c$, thus:

$$E_{max} \sim Z \cdot 300 \text{ TeV}.$$

In conclusion, the *diffusive shock acceleration* mechanism shows that charged CRs can be accelerated in SNRs up to the "knee" region and that the energy cut-off depends on the charge of the particle. This picture is in agreement with several indirect observations of CRs from ground that seem to confirm that the value of the cut-off for protons and light nuclei is smaller than the one for heavier nuclei [4].

1.3 Cosmic-ray propagation in the galaxy

The observed spectral indexes of the CR spectra on the Earth depend on both the acceleration and the propagation of CRs in the galaxy. During the propagation of CRs through the galaxy the charged particles are affected by the galactic magnetic field irregularities due to both the intrinsic fluctuations in the fields and to the instabilities generated by the scattering of CR particles with the fields itself. Furthermore, CRs interact with the materials distributed in the galaxy. Only a small fraction of space in the galaxy is occupied by matter in form of stars while the rest is occupied by large masses of gas and tiny solid particles (the interstellar dust). These materials are named InterStellar Matter (ISM); the density of the ISM is about 1 proton/cm^3 [15]. The ISM is mainly composed by neutral and molecular hydrogen and a very small fraction ($< 1\%$) of heavier elements is present.
The particle propagation in the galactic magnetic field can be considered as a diffusion motion and, by taking also into account the interaction with the ISM, can be described by the following equation (see [16] for the complete derivation):

$$\frac{dN_i}{dt} = D\nabla^2 N_i + \frac{\partial}{\partial E}\left[b(E)N_i(E)\right] + Q - \frac{N_i}{\tau_i} + \sum_{j=i+1}^{\infty} \frac{Pij}{\tau_j} N_j, \tag{1.5}$$

where:

- N_i is the density of the CR particle of species i per unit energy, usually measured in [eV^{-1}cm^{-3}]
- $D\nabla^2 N_i$ is the diffusion term that follows the so called *"coordinate space approach"*,
- $\frac{\partial}{\partial E}\left[b(E)N_i(E)\right]$ takes into account the particle energy gains and losses,
- Q is the injection rate per unit of volume describing the acceleration sources,
- $\frac{N_i}{\tau_i}$ is the rate of the spallation of the nucleus i with a spallation lifetime τ_i,
- $\sum_{j=i+1}^{\infty} \frac{Pij}{\tau_j} N_j$ is the gain in the nucleus i abundance due to the spallation of nuclei j with a charge greater than the one of the nucleus i, where Pij is the probability that an inelastic collision disrupts the nucleus j and creates the specie i.

This equation is known as the *"diffusion-loss equation"* and almost all the terms depend on the particle energy. Numerical solutions of the complete equation can be

found, depending on the boundary conditions, but are not discussed in this thesis: one of the most known codes for the solution of this equation is GALPROP [17].
A commonly adopted approximation of the diffusion-loss equation is the so-called *"Leaky Box Model"* (LBM): a charged particle can freely propagate in the galactic halo with a mean escape time τ_{esc} that depends on the energy, so the diffusion term can be replaced with:

$$D\nabla^2 N_i \rightarrow -\frac{N_i}{\tau_{esc}}.$$

By assuming the energy gain and loss term negligible (this approximation is discussed in §1.5.2), the stationary solution ($\frac{dN_i}{dt} = 0$) of equation 1.5 in the LBM approximation can be written as:

$$\frac{N_i}{\tau_{esc}} = Q_i(E) - \frac{N_i}{\tau_i} + \sum_{j=i+1}^{\infty} \frac{Pij}{\tau_j} N_j. \tag{1.6}$$

The value of the escape mean time τ_{esc} can be evaluated with the measurement of the *secondary* to *primary* nuclei (S/P) ratio in CRs. In this chapter the word "*primaries*" indicates the CRs originated and accelerated by astrophysical sources, for example SNRs: these particles interacting with the ISM could produce new particles named "*secondaries*". Elements like Li, Be and B are produced in very small quantities in stellar nucleosynthesis, thus their primary fraction is negligible with respect to the secondary fraction. The latter is generated mainly by the spallation of carbon and oxygen primaries on the ISM. For these purely secondary species the term $Q_i(E)$ in equation 1.6 is negligible. Consider a purely secondary nucleus S produced by a single primary nucleus P:

$$\frac{N_S}{\tau_{esc}} = -\frac{N_S}{\tau_S} + \frac{P_{PS}}{\tau_P} N_P. \tag{1.7}$$

The S/P ratio in this simple model is:

$$\frac{N_S}{N_P} = \frac{P_{PS}}{\tau_P} \left[\frac{1}{\tau_{esc}} + \frac{1}{\tau_S} \right]^{-1},$$

and if $\tau_S >> \tau_{esc}$:

$$\frac{N_S}{N_P} \sim \frac{P_{PS}}{\tau_P} \tau_{esc}.$$

The mean escape time τ_{esc} is proportional to the S/P ratio so the measurement of S/P can provide important information about the values of τ_{esc} in function of the nuclei energy. In several CR models it is common to substitute the τ_{esc} with the mean path length (also named *"grammage"*) of matter traversed by a particle $\lambda_{esc} = \rho_{ISM}\ c\ \tau_{esc}$

[g cm^{-2}] and the τ_P with the mean interaction length of the primary nucleus $\lambda_P = \rho_{ISM}\ c\ \tau_P$ [g cm^{-2}] obtaining the flowing relation:

$$\frac{N_S}{N_P} \sim \frac{P_{PS}}{\lambda_P}\lambda_{esc}.$$

The parameters P_{PS} and λ_P depend on the nuclear species and are measured at accelerator experiments.

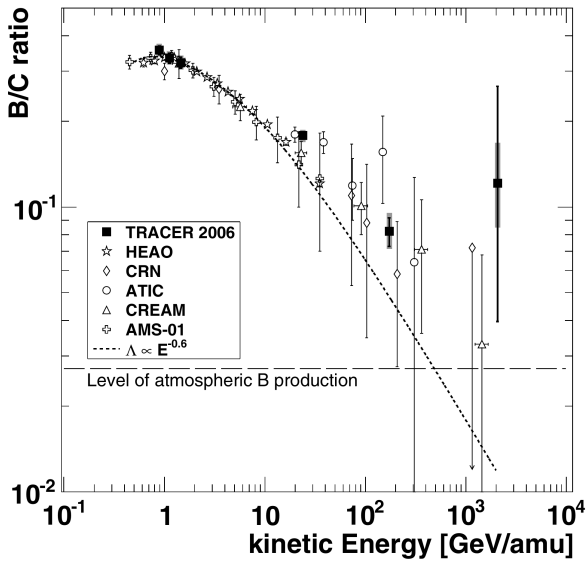

Figure 1.4. *Boron-to-carbon abundance ratio as a function of kinetic energy per nucleon measured by different experiments [18]: a fit of the data using equation 1.8 is shown with dotted line.*

As a first approximation, this scheme can be applied to the Boron to Carbon ratio (B/C ratio): B is mainly secondary and its main progenitor is C. Fig. 1.4 shows the B/C ration measured by different experiments: the dotted line is a fit to the data points using the relation between the B/C ratio and λ_{esc} as expected with the LBM and assuming the following parametrization of λ_{esc} [19]:

$$\lambda_{esc} = \frac{K\beta}{(\beta\frac{R}{1\ \mathrm{GV}})^{\delta} + (0.714\beta \cdot \frac{R}{1\ \mathrm{GV}})^{-1.4}}, \tag{1.8}$$

where β and R are the nucleus velocity and rigidity (momentum divided by the charge), K and δ are the parameters of the fit. The dotted line in fig. 1.4 corresponds to the

following values for the fit parameters:

$$K \simeq 27 \frac{\mathrm{g}}{\mathrm{cm}^2};\ \delta \simeq 0.6.$$

Equation 1.8 can be approximated at high-energy (> 5 GeV) with a single power law:

$$\lambda_{esc} = \lambda_0 \cdot \left(\frac{R}{5\ \mathrm{GeV}/c} \right)^{\delta},$$

where λ_0 is about 10 g cm^{-2}. By recalling the relation between the grammage and the escape time ($\tau_{esc} = \frac{\lambda_{esc}}{\rho_{ISM}\ c}$) and roughly approximating the density of the interstellar material as one hydrogen atom per cm^{-3} (equal to $\sim 1.6 \cdot 10^{-24}$g cm^{-3}), the escape time for particles with rigidity of about 5 GeV is $\tau_{esc} \sim 10^7$ years.

The trend of the mean escape time with energy affects the CR spectra measured at Earth, which become significantly different with respect to the spectra of particles ejected by the CR sources. For a primary nucleus, by neglecting the fragmentation and energy loss terms, the diffusive-loss equation 1.6 can be written as:

$$N_i = \frac{\tau_{esc} Q_i(E)}{1 + \tau_{esc}/\tau_i}.$$

For protons the mean traversed path length λ_{esc} is smaller than the interaction length λ_i ($\lambda_i > 50$ g cm^{-2}) thus as a first approximation the term $\frac{\tau_{esc}}{\tau_i} = \frac{\lambda_{esc}}{\lambda_i}$ can be neglected. The resulting particle spectrum Φ as a function of the energy is:

$$\Phi(E) \propto \tau_{esc} Q_i(E).$$

By using the results of §1.2 and the B/C ratio measurements, the source term Q_i for SNRs is proportional to E^{-2} and $\tau_{esc} \propto E^{-0.6}$:

$$\Phi \propto E^{-2} \cdot E^{-0.6} = E^{-2.6}.$$

In conclusion with this very simple approach the expected CR all-particle spectrum is a single power law with a spectral index of ~ -2.6. By taking into account all the approximations involved in the discussed models, this value fits reasonably the experimental observation of a power law spectrum with a spectral index of ~ -2.7.

1.3.1 Energy loss and electron propagation

In the previous description of the particle propagation in the galaxy the energy loss due to the interaction of CRs with the ISM has been considered negligible. The main energy loss processes involved in charged particle propagation are the synchrotron radiation and inverse Compton scattering and the energy-loss rate can be written as [20]:

$$\frac{dE}{dt} = -b_0 \cdot E^2 \; ; \; b_0 = \frac{4\sigma_T c}{3m^2c^4}\left(\frac{B^2}{8\pi} + w_{ph}\right), \tag{1.9}$$

where σ_T is the Thomson scattering cross section, c is the speed of light, m is the particle mass, B is the magnetic field surrounding the particle and w_{ph} is the energy density of interstellar photons (dominated by the photons of the CMB, re-emitted radiation from dust grains and stellar radiation). The first term in the definition of b_0 is related to the synchrotron radiation, that it is dominant for particles near the acceleration sites because the magnetic field is usually intense in those regions, while the second term is related to the inverse Compton scattering. Since dE/dx depends on m^{-2} the impact of the energy loss during the propagation of protons and nuclei is in fact negligible while for electrons (and positrons) it is very important due to the small mass. As a first approximation, by assuming the diffusion term negligible, the energy-loss term is dominant and the diffusion-loss equation for electrons in the steady state is:

$$\frac{\partial}{\partial E}\left[b(E)N_i(E)\right] = -Q(E).$$

By integrating this equation, assuming $N_i(E) \to 0$ when $E \to \infty$ and recalling that the expected source term $Q(E)$ for a diffusive shock acceleration source is $\propto E^{\alpha}$ and $b(E) = b_0 \cdot E^2$, the expected energy spectrum is:

$$\Phi(E) \propto E^{\alpha-1}.$$

Since the value of α is ~ -2 the expected spectral index for electrons is ~ -3: this value is in reasonable agreement with the direct measurements of CR electron spectrum as discussed in the §1.5.2.

The energy loss rate of electrons has an important role in the identification of nearby CR sources, since the maximum distance from which high-energy primary CR electrons can reach the Earth depends on this parameter. The amount of time T needed for a

high-energy electron ($E \sim \infty$) to lose its energy down to E_0 can be calculated by integrating the equation 1.9:

$$\int_{\infty}^{E_0} \frac{dE}{E^2} = -b \int_0^T dt.$$

The results is:

$$T = \frac{1}{bE_0},$$

thus T becomes shorter with an increasing final energy and by assuming a magnetic field $B \sim 5$ μG the mean time is $T \sim \frac{2.5 \cdot 10^5 \text{ yr}}{E \text{ (TeV)}}$. During this time interval, electrons propagate with a diffusion motion described with a diffusion coefficient that can be approximated within the LBM as:

$$D(E) \sim \frac{H^2}{\tau_{esc}(E)},$$

where H is the height of the galactic halo (about $5 \div 10$ kpc) and $\tau_{esc}(E)$ is the mean escape time in the LBM derived in section 1.3. For electrons at 1 TeV the diffusion coefficient is about 10^{29} cm^2 s^{-1} and the mean diffusion distance $l = \sqrt{2DT}$ is about 1 kpc. Thus, only electrons accelerated by nearby sources within a range of few kpc can reach the Earth with an energy above 1 TeV; therefore the direct measurement of high-energy electrons in CR provides important information about the nearby CR sources.

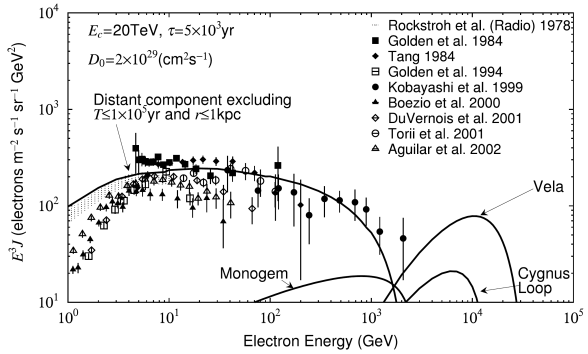

Figure 1.5. *Expected electron spectrum (solid line) as calculated in [20] by assuming a diffusion coefficient* $2 \cdot 10^{29}$ cm^2 s*, a cutoff of* 20 TeV *and a burst-like release at* $5 \cdot 10^3$ yr*. The contribution of 3 nearby source candidates (Vela, Monogem and Cygnus-Loop) and an approximation of the electron spectrum coming to the Earth from distant sources are taken into account. Some measurements of the electron spectrum are also shown.*

Since the amount of nearby CR sources such as SNR is small, it is possible, by developing detailed theoretical models, to obtain an estimate of the expected flux of high-energy electrons. As an example, the expected energy spectrum calculated in [20] is shown in fig. 1.5: here the model takes into account an energy cut-off $E_c = 20$ TeV in the injected spectrum of electrons released at once after the SNR explosions in a release time of $5 \cdot 10^3$ yr. An increase of the electron flux due to the contribution of the Vela SNR in the multi-TeV region is expected.

1.4 Solar modulation and geomagnetic cut-off

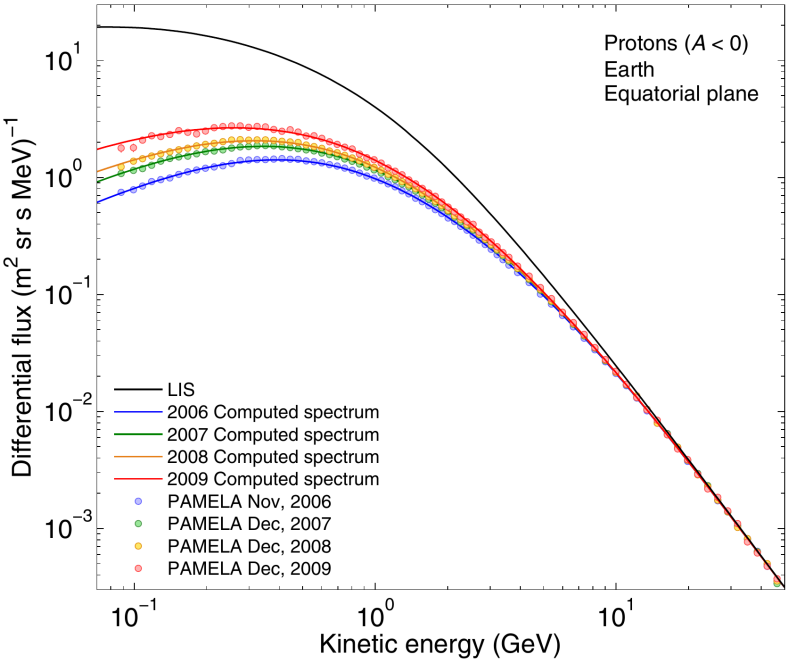

Figure 1.6. *Low-energy proton spectra measured by PAMELA for 2006 November (blue), 2007 December (green), 2008 December (yellow) and 2009 December (red) [3]. Coloured solid line are the expected proton spectra with the model described in [25] and the black solid line is the local interstellar spectrum (LIS) used for the computation.*

The low-energy CR spectra measured at the Earth are affected by the solar wind. The latter consists of charged particles, mostly electrons, protons and alpha particles, expelled from the upper atmosphere of the Sun with a kinetic energy between 1.5 and 10 keV. The solar wind carries the heliospheric magnetic field, that is an extension of the coronal magnetic field and is precisely described in [23]. Solar activity varies with time with a cycle of approximately 11 years. The heliospheric magnetic field decelerates

and partially excludes the lower energy particles from the inner solar system, thus the low-energy component of the CR flux (at a rigidity below some tens of GV) undergoes a variation over the solar activities; this effect is known as the "*solar modulation*".
The intensity of low-energy CRs can be tracked with neutron monitors at the ground level, which detect neutrons produced by the interactions of CRs with the atmospheric nuclei [24]. These experiments show a strong correlation between the low-energy neutron abundance and the solar activity, with the neutron counts reaching a maximum during periods with low solar activity. A direct observation of the effect of the solar modulation on the CR protons is shown in fig. 1.6 [3]: the higher proton flux (observed in 2009) corresponds to a minimum in the solar activities.

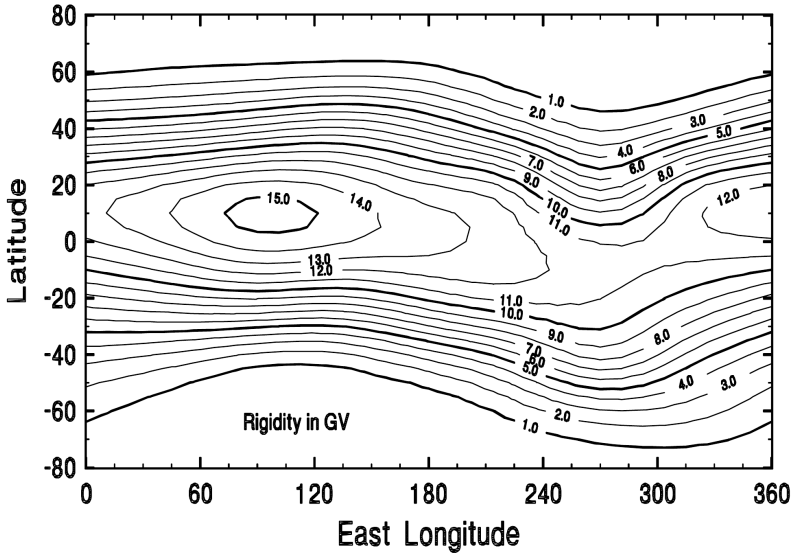

Figure 1.7. *Contour maps vertical rigidity cut-off (GV) at a height of* 450 km *above the Earth surface [22].*

Before reaching the top of the Earth's atmosphere, charged particles are affected by the geomagnetic field, which determines a dependency of the low-energy spectra on the position. The treatment of the orbits of particles incident on the Earth magnetic field is complex, and requires dedicated computer programs to take into account the details of the problem [22]: here a simplified approach is present in order to point out some important features.
The Earth magnetic field can be approximated with a dipole with the current N pole being located at longitude of about 101° W, latitude 75° N; the magnitude of the

magnetic field B is roughly approximated by:

$$B = \frac{\mu_0 M}{4\pi r^3},$$

where μ_0 is the permeability of the free space, M is the magnetic momentum and r is the distance from the magnetic dipole centre. The measured magnetic field at the Earth surface is about $\sim 0.310^{-4}$ T, therefore $M \sim 8 \cdot 10^{22}$ Am^2. The trajectory of a charged particle with mass m and charge Ze orbiting in the circular equatorial path of the dipole at radius r with velocity v curves according to the Lorentz force:

$$\frac{m\gamma v^2}{r} = Ze \cdot v \cdot B,$$

where γ is the Lorentz factor, and by rewriting the previous equation:

$$r = \sqrt{\frac{\mu_0}{4\pi}\frac{ZeM}{p}},$$

where p is the particle momentum. Due to the magnetic field, low-energy particles with positive charge coming from the Est are deflected outside the Earth atmosphere, while the trajectories of particles coming from the West are curved in the opposite direction. This is known as the Est-West effect and it was measured by Compton in 1932. The value of the minimum rigidity for an incoming particle to be able to reach the Earth is named "geomagnetic cut-off" and for particles in the equatorial plane coming from the East is approximated with the rigidity of a circular orbit with radius equal to the Earth radius r_E:

$$\frac{p}{Ze} = \frac{\mu_0}{4\pi}\frac{M}{r_E^2} \sim 50 \text{ GeV}.$$

With more complex calculations, first developed by Störmer (1955) [21], and recently updated and validated in [22], it is possible to derive an approximated formula to compute the rigidity cut-off as a function of the particle direction, the altitude, the latitude and the longitude. As an example, for an altitude of about 450 Km and a latitude ~ 0 the rigidity cut-off for vertical particles is about 15 GeV/c and decreases with an increasing latitude as shown in fig. 1.7 [22]. An approximated equation for the calculation of the rigidity cut-off R_{CV} for vertical particles, expressed in GV, is:

$$R_{CV} = 14.5\frac{\cos^4 \lambda}{r^2},$$

where λ is the latitude from the magnetic equator and r the distance from the dipole centre expressed in unit of Earth radius (6.371 km). According to this parametrization the rigidity cut-off decreases with the distance from the Earth and with the latitude, as observed by several experiments [22].

1.5 Recent measurements of cosmic-ray spectra

The simplified models for the acceleration and propagation of CRs in the galaxy described in the previous sections can reasonably explain the CR measurements discussed in §1.1, by taking also into account the geomagnetic cut-off and the solar modulation for low-energy CR spectra. Recently new precise measurements have shown new structures in CR individual spectra. The interpretation of these new features required both new theoretical models, beyond the diffusive shock acceleration and the standard diffusion propagation model, and more accurate measurements with a new generation of experiments. After a brief overview of the most common techniques for the CR measurements, some important results are discussed.

The observations of CRs can be indirect, by employing ground experiments, or direct, with balloon or space detectors. Direct observations of CRs by experiments installed on satellites and balloons provide precise information about single-particle spectra. These experiments undergo the typical limitations of balloon and space missions in terms of data taking time, mass and power consumption; the total exposure they achieve is usually too low to be able to study the high-energy, low-statistics region of the spectra with a reasonable statistical error. At present, only the region below the knee ($\sim$ PeV) has been studied with direct measurements. Experiments for the direct observation of CRs at energies from GeV to hundreds of TeV can be divided in two main classes: spectrometers and calorimetric experiments.
Space-borne spectrometers like the PAMELA [28] and AMS-02 [37] experiments have the capability to identify the sign of the charge of the observed particles by reconstructing the curvature of the trajectory inside the magnetic field of the instrument, and are primarily devoted to the study of the antimatter component of CRs. By employing a quite strong magnetic field (B) and a tracker with very good space resolution (σ_X) for the identification of the particle trajectory (e.g. $B \sim 0.5$ T and $\sigma_X < 3$ μm for PAMELA) these experiments estimate the momentum (p) of the particle by measuring

the track curvature (r). As an example, for a constant magnetic field the relation between the momentum and the curvature is:

$$p(\mathrm{GeV/c}) = 0.3 \cdot Z(\mathrm{C/e}) \cdot r(\mathrm{m}) \cdot B(\mathrm{T}),$$

where $Z(C/e)$ is the particle charge in unit of positron charge. In addition to the tracker, a segmented calorimeter is typically present and used not only for an independent measurement of the particle energy but also for the electron-hadron discrimination based on the topological analysis of the shower development. Due to the constraints in in terms of total weight, in spectrometric space experiments the calorimeter is typically thin, especially for hadronic shower (the vertical thickness of the PAMELA calorimeter is ~ 16.8 $\mathrm{X_0}$).
Calorimetric experiments like CREAM [29], ATIC [30] and CALET [31] (the latter described in details in §2) consist of a deep, large-acceptance calorimeter which can effectively contain the showers and provide precise energy measurements up to energy regions (multi-TeV) that are not accessible with spectrometers. On the other hand, they are not able to distinguish matter from antimatter, so only inclusive measurements (e.g. electrons+positrons) can be made. Above the top face of the calorimeter, a finely segmented detector can be present and used both as a tracker and as a charge detector.

Since the flux of CR is very steep, a large acceptance is required to achieve statistically significant measurements of high-energy CR flux (i.e. above the knee) and ground experiments achieve very large acceptance. Ground experiments observe the signals of the shower developed in the Earth atmosphere by the CRs, named "*Extended Air Showers*" (EASs). For the particle identification and the energy measurement these experiments needs a precise reconstruction of the EAS, thus they are affected by large systematic errors due to modelling of the interaction of particles with the atmosphere. EASs can be detected with arrays of sensors spread over a large area observing the most penetrating particles, mostly muon (e.g the KASCADE experiment [26]), detecting the photons emitted by the EASs through the Cherenkov effect (e.g. the HESS experiment [42]) and measuring the fluorescence emission associated to the excitation of nitrogen molecules by the particles in the EASs (e.g. in the Pierre Auger Observatory [27], in parallel to the surface detector, a modern fluorescence detector is used).

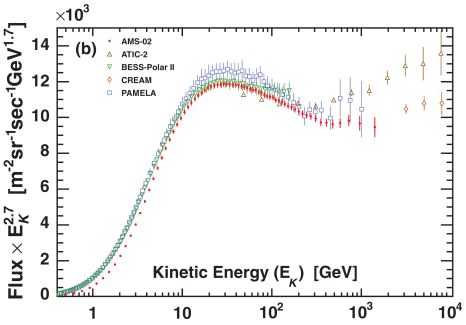

(a) *Proton spectrum [37]*

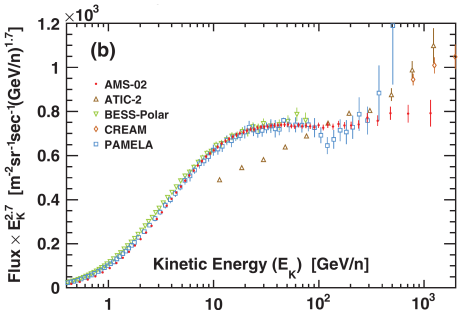

(b) *Helium spectrum [38]*

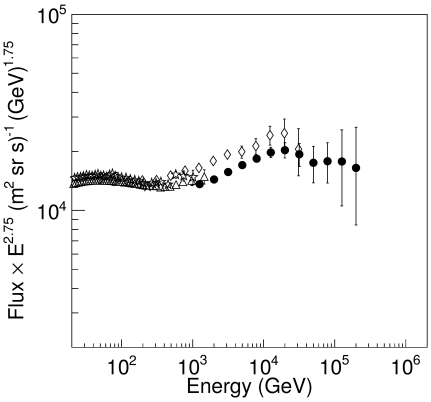

(c) *Proton spectrum [34]*

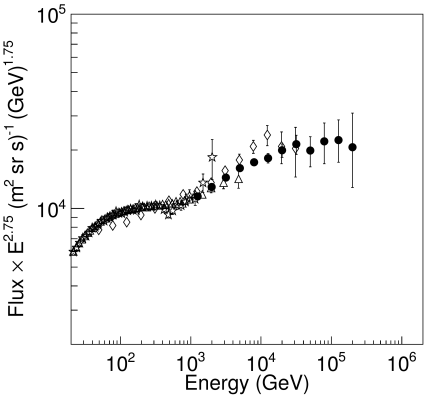

(d) *Helium spectrum [34]*

Figure 1.8. *Direct measurements of proton and helium spectra by different experiments: ATIC [32], BESS [33], CREAM-I and CREAM-III [34], AMS-02 [37] [38], PAMELA [36]. Proton and helium spectrum as functions of the kinetic energy per nucleon (E_k/n) multiplied by $(E_k/n)^{2.7}$ from AMS-02 data compared with other measurements are shown in (a) and (b). High-energy proton and helium spectrum as functions of the total energy per nucleon (E/n) multiplied by $(E/n)^{2.75}$ from the combined CREAM-I and CREAM-III data (filled circles), AMS-02 (triangles), ATIC-2 (diamonds), and PAMELA (stars) are shown in (c) and (d).*

1.5.1 Direct measurements of the proton and helium spectra

The proton flux up to some TeV is shown in fig. 1.8a. The spectrum (Φ) up to $40 \div 60$ GeV is affected by the solar modulation while from 60 GeV to ~ 200 GeV is well approximated by a single power law ($\Phi = K \cdot E^{\alpha}$) with a spectral index $\alpha \sim -2.85$. The CREAM-I measurement of the proton flux above 1 TeV [35] showed for the first time that the spectral index in this region is about -2.66. This result suggested that a hardening of the spectrum must occur in the sub-TeV region. After the CREAM-I measurement, the turnaround point was first directly observed by the PAMELA experiment at ~ 230 GeV, and subsequently confirmed by AMS-02 (event though at a slightly higher energy). Though the spectrum can be approximated with a broken power-law

by using the mentioned spectral index values, a more complex parametrization of the flux measured by AMS-02 above 50 GeV, proposed in [37], is:

$$\Phi = C \left(\frac{R}{45 \text{ GV}} \right)^{\gamma} \left[1 + \left(\frac{R}{R_0} \right)^{\Delta\gamma/s} \right]^{s},$$

where the Φ is the proton flux, R is the rigidity and R_0, γ, $\Delta\gamma$, C and s are the fit parameters. By fitting the AMS-02 data, these parameters assume the following values: $R_0 \sim 330$GV, $\gamma \sim -2.85$, $\Delta\gamma \sim 0.13$, $C \sim 0.45$ and $s \sim 0.024$. The change in spectral index has been investigated by different theoretical models related to the acceleration and propagation of CRs in the galaxy, e.g according to [39] the proton spectrum structure can be related to the interactions of CRs with a background of waves due to self-generation and to wave-wave turbulent cascading from a large scale. Indirect measurements with ground experiments feature a spectral cut-off of the proton flux above hundreds TeV in agreement with the model related to the acceleration in SNR (§1.2). The recent direct measurement of the proton flux above 1 TeV by the CREAM-III balloon experiment [34] is shown in fig. 1.8c. This measurement confirms the spectral breaks observed by CREAM-I. The errors at high-energy are large due to the limited statistics, typical of balloon experiments due to the short exposure time (29 days for CREAM-III) with respect to a satellite experiments (5 years for CALET, see chapter 2). More precise direct observations of the proton flux up to hundred TeV are needed to point out possible spectral features up to the expected proton knee.

The helium spectrum as measured by different direct experiments is shown in figure 1.8b and 1.8d. The trend is very similar with respect to the proton spectrum, with a spectral hardening around 200 GeV/n. The abundance of proton is about 5 times greater than the one of helium for a kinetic energy of ~ 30 GV but the proton/helium ratio becomes smaller with increasing energy [38]. Above 45 GV the proton/helium ratio measured by AMS is well approximated by single power-law with a spectral index of ~ -0.077. A cut-off in the helium spectrum is expected above hundred TeV per nucleon.

1.5.2 Electron spectrum

Fig. 1.9 [40] shows the electron spectrum measured by Fermi-LAT experiment compared with the AMS-02 and H.E.S.S measurements.

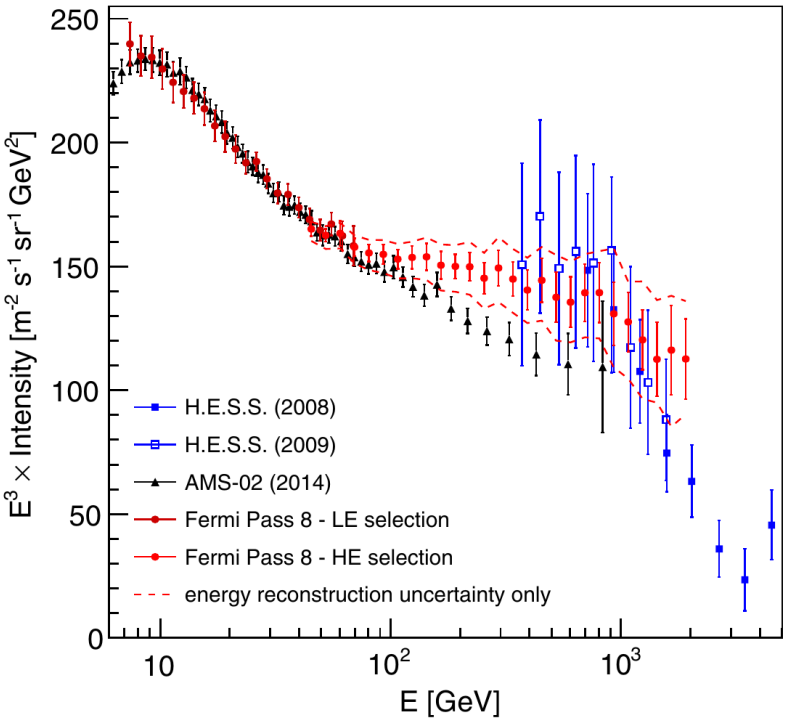

Figure 1.9. *CR electron spectrum multiplied by E^3 measured by the Fermi-LAT experiment [40] compared with AMS-02 [41] and H.E.S.S. [42]. All error bars represent the quadratic sum of statistical and systematic uncertainties. The area between the dashed lines corresponds to the uncertainty band due to the energy measurement uncertainty.*

The Fermi-LAT detector, installed on the Fermi Gamma-Ray Space Telescope spacecraft, is designed to detect gamma rays up to about a hundred GeV. It is also able to identify the CR electrons mainly thanks to a silicon-strip based tracker-converter and an imaging calorimeter consisting of 8 layers of CsI crystals. The vertical depth of the calorimeter is about 8.6 X_0, then the high-energy electromagnetic showers are not fully contained: above 1 TeV only $\sim$ 35% of the shower is on average contained in the calorimeter and the energy resolution is $\sim$ 20% [40]. The electron spectrum measured by Fermi-LAT (red points in figure 1.9) is in good agreement with those previously measured by AMS-02 (black points) below 100 GeV, while above a discrepancy is present. The Fermi-LAT measurement suggests that the electron spectrum is well approximated by a broken power-law with a spectral index α of ~ -3.21 below 50 GeV and $\alpha \sim -3.07$ above. The values of these spectral indexes are in reasonable agreement with respect to the one expected with the simplified calculation described in §1.3.1. Furthermore, the electron spectrum measured by HESS (blue points in figure 1.9), that is compatible with both Fermi-LAT and AMS-02 in the low-energy range, features a

steeper spectrum above 1 TeV and suggests the existence of a cut-off in the electron flux. New precise direct observations of CR electron spectrum above 2 TeV, where only indirect observations are available now, are needed in order to stress the model related to nearby CR sources discussed in §1.3.1 with more precise measurements.

1.5.3 B/C ratio

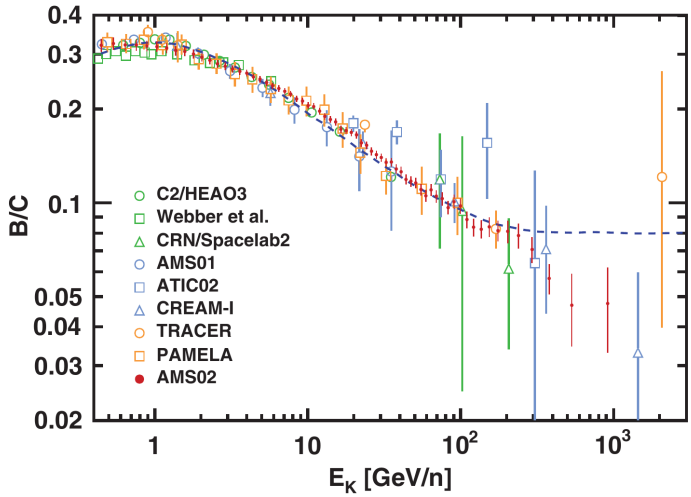

Figure 1.10. *Boron to carbon ration as a function of kinetic energy per nucleon E_K measured by AMS-02 [43] compared with previous measurements [18],[45]-[51]. The dashed line is the B/C ratio predicted by the model described [44].*

Fig. 1.10 shows the B/C ratio in kinetic energy per nucleon measured by AMS-02 [43] compared with previous experiments. The B/C ratio increases with the kinetic energy reaching a maximum at about 2 GeV/n then it decreases without any evident structure. Above 60 GeV/n it can be approximated with a single power law by using a spectral index of about 0.3 that is in good agreement with the Kolmogorov theory of turbulence [52] but it is different with respect to the value estimated by employing the data of older experiments, described in §1.3.

Since this parameter have a big impact in the galactic particle propagation models and also in the interpretation of the observed spectrum at Earth, direct measurement in the TeV region and above are needed to further investigate this problem and to look for possible structures in the ratio at very-high energies.

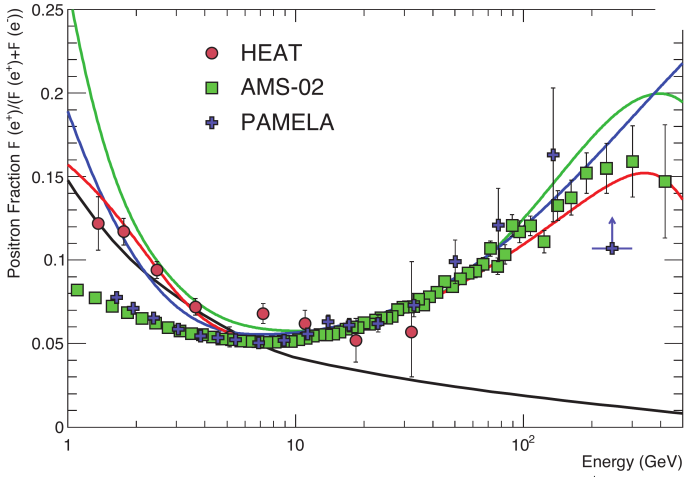

Figure 1.11. *Fraction of positron in the electron+positron flux measured by PAMELA [53], AMS-02 [54] and HEAT [55]. The black line is a model of pure secondary production [56] and the three thin lines show three representative attempts to model the positron excess with different phenomena; green: dark matter decay [57]; blue: propagation physics [58]; red: production in pulsars [59].*

1.5.4 Antimatter

Since in this section the antimatter component is discussed, here the word "electron" does not indicate the"electron+positron" component in CRs but only the electrons one. Currently there is no experimental evidence of the presence of anti-deuterium, anti-helium or heavier anti-matter nuclei in the CRs while positrons and anti-protons are present: the positron abundance at 100 GeV is about 10% with respect to the electron one and the anti-proton/proton ratio at 100 GeV is $\sim 2 \cdot 10^{-4}$. Before the PAMELA measurements it was commonly accepted that the anti-matter component of CRs was manly secondary, coming from the interaction of primary protons, electrons and nuclei with the ISM. According to the standard propagation and interaction model, e.g. [56], the electron/positron ratio decreases with an increasing energy. The PAMELA measurement [53] showed for the first time that the positron fraction $(e^+/(e^+ + e^-))$ increases above $\sim$ 10 GeV; this observation was also confirmed by AMS-02, as shown in fig. 1.11. Contrariwise the anti-proton fraction [60], above $\sim$ 50 GeV of kinetic energy, decreases with energy as expected by the propagation model.

Several explanations of the increasing e^-/e^+ has been investigated: this structure suggests the presence of primary positron sources and may be related to contributions of dark matter decay/annihilation processes (see for example [57]) or from individual

nearby sources, e.g. pulsar which are commonly considered efficiency sources of electrons and positrons [59]. Modified propagation models that not require additional electron and positron sources are also investigated but the most of these models (e.g. [44]) forecast an increase (or some structures) of the B/C ratio or the anti-proton/proton ratio, contrariwise to the recent experimental observations. In order to investigate the origin of the e^-/e^+ increase, it is important to extend at high-energy the e^-/e^+ measurement as well as to achieve precise measurements of the electron+positron spectrum for the search of dark matter or/and nearby source signatures, as described in 1.3.1

Chapter 2

The CALET experiment

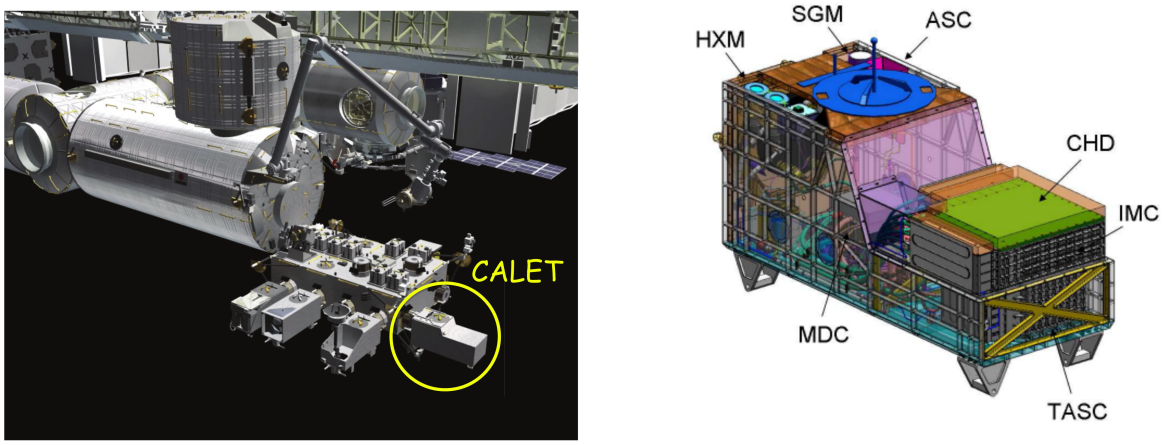

Figure 2.1. *Left: Japanese Experiment Module-Exposed Facility and CALET attached at the 9 port. Right: schematic view of the CALET payload with the main calorimeter and all the subsystems.*

The CALorimetric Electron Telescope (CALET) [61] is a space calorimetric experiment for the direct measurement of high-energy CR spectra. CALET is a Japanese-led international space mission by the Japanese AeroSpace Agency (JAXA) in collaboration with the Italian Space Agency (ASI) and NASA. The payload was launched to the International Space Station (ISS) on August 19 2015 by the Japanese H-II Transfer Vehicle (HTV-5) and docked at the Exposed Facility of the Japanese Experiment Module (JEM-EF) on August 25, 2015. Left panel of fig. 2.1 shows the CALET attach point on the JEM-EF. After a first commissioning period the CR observation operations started on October 13, 2015 for an initial period of 2 years, with a maximum target period of 5 years.

The CALET primary science goal is the measurement of the electron spectrum up to the multi-TeV region. Other important objectives are the measurement of the proton and nuclei spectra (from helium to iron) up to hundreds TeV per nucleon and the observation of high-energy gamma rays for the identification of the gamma sources. The detector is a deep electromagnetic calorimeter composed by three sub-detectors: a charge-detection device (CHD) composed of two layers of plastic scintillators, a finely-segmented sampling calorimeter (IMC) with imaging capabilities made of scintillating fibres and a deep (27 radiation lengths for vertical incident particles) homogeneous calorimeter (TASC) with $PbWO_4$ (lead tungstate, or PWO) scintillating logs. See the next section for a precise description of the calorimeter.

CALET also includes a detector for the identification of Gamma Ray Bursts (GRBs) signals, the *"CALET Gamma ray Burst Monitor"* (CGBM) [62], designed for the detection of photons from 7 keV to 20 MeV and consisting of 3 detectors: one *"Hard X-ray Monitor"* (HXM) composed by a $LaBr_3(Ce)$ scintillator for the detection of X-rays from 7 keV to 1 MeV, and two *"Soft Gamma ray Monitors"* (SGMs) $Bi_4Ge_3O_{12}$ (bismuth germanate, or BGO) scintillators optimized for low-energy gamma measurement from 100 keV to 20 MeV.

The CALET instrument also includes an *"Advanced Stellar Compass"* (ASC) for attitude determination and a *"Mission Data Controller"* (MDC) to manage the individual detector systems and handle the accumulated data. The right panel of fig. 2.1 shows the CALET payload.

2.1 The calorimeter

The CALET calorimeter is composed by three detectors (fig. 2.2): a *"CHarge Detector"* (CHD) placed at the top of the instrument, an *"IMaging Calorimeter"* (IMC) in the middle section and a *"Total AbSorption Calorimeter"* (TASC) at the bottom of CALET.

The CHD is designed to identify the charge of incident particles, by exploiting the Z^2 dependence of the ionization energy loss in plastic scintillators. The CHD consists of 28 plastic EJ-204 scintillator paddles of 10 mm thickness, 32 mm width, and 448 mm

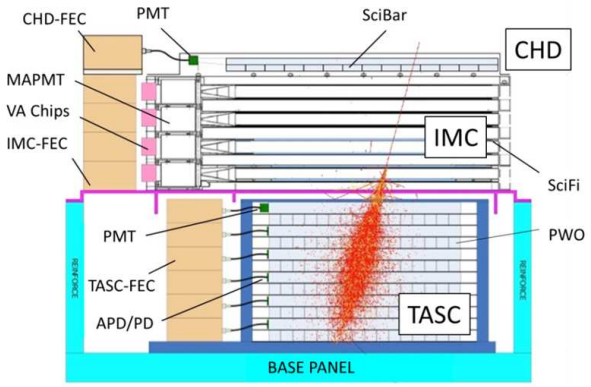

Figure 2.2. *Representation of the CALET main detectors. An electromagnetic shower simulated with MC simulation based on EPICS package [70] is also shown. The Z axis is the vertical direction.*

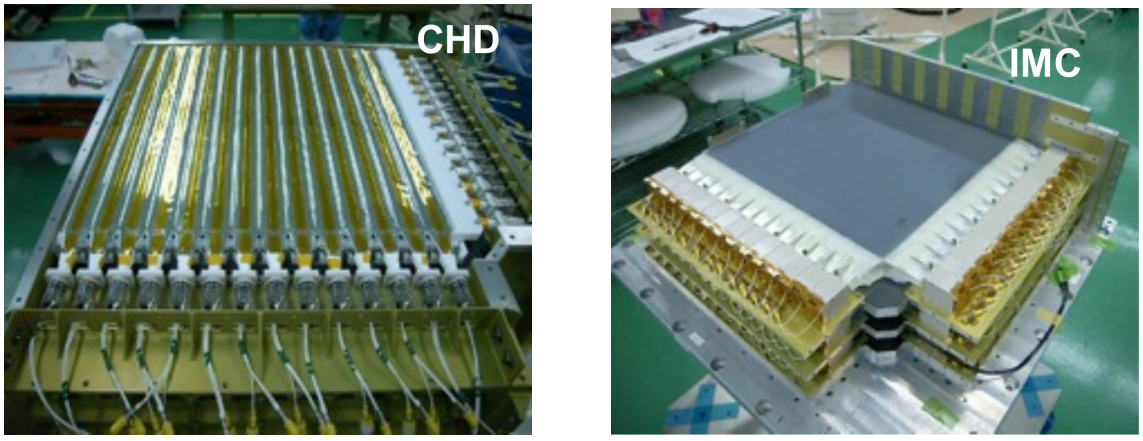

Figure 2.3. *Left: picture of the CALET CHD. Right: Picture of the CALET IMC.*

length, arranged in 2 layers of 14 paddles each. The paddles of the first layer are parallel to the Y direction, in order to achieve a rough measurement of the X coordinate (this layer is named CHDX), and the other one in the orthogonal direction (CHDY) (the Z axis goes from the top to the bottom of the detector). Each scintillating paddle is read-out at one-end by a light guide with one photo multiplier tube (PMT) Hamamatsu R11823; the paddles are wrapped with reflective 3M Vikuiti ESR films in order to increase the light collection. A picture of the CHD is shown in the left panel of fig. 2.3. According to the MC simulation [63], confirmed by beam test results [64], the CHD can resolve individual chemical elements from Z=1 to Z=40 with a charge resolution of about 0.15 e for B and C and ~ 0.3 e for Fe.

The IMC is an imaging preshower device which allows to precisely measure the

incident particle trajectory (see §4.6.2) and to identify the starting point of the shower as described in [66]. It is composed by 8 planes of Scintillating Fibres (SciFis) with a transverse section of 1 mm^2 and 448 mm. Two consecutive planes are spaced 2 cm apart by a honeycomb support structure. Seven tungsten sheets are placed directly on top of each plane except the first one. A SciFi plane consists of 448 fibres oriented in direction Y and 448 in direction X. The 448 SciFis are assembled into one belt and read-out with Hamamatsu R7600-M64 64 channels multi-anode photo-multiplier tubes (MaPMTs) [67]. The front-end electronics for the MaPMTs is based on a dedicated 32 channels Viking VA32-HDR14.3 high density ASIC [68]: it features a large dynamic range (up to 15 pC), low power consumption and low noise. All the tungsten plates have a squared shape: each tungsten plate of the first 5 layers, starting from the top, has a thickness of 0.7 mm equal to 0.2 X_0 while in the last 2 layers the plates have a thickness of 3.5 mm = 1 X_0 each one. The total thickness of the IMC tungsten layers is 3 X_0. The right panel of fig. 2.3 shows a picture of the IMC.
The IMC planes are named "IMCXN" and "IMCYN", where "IMCXN" indicates the 448 SciFis that measure the X coordinate in the N-th IMC plane, "IMCYN" indicates the SciFis oriented in the opposite direction, and N enumerates the planes from the top (N=1) to the bottom (N=8) of the IMC.

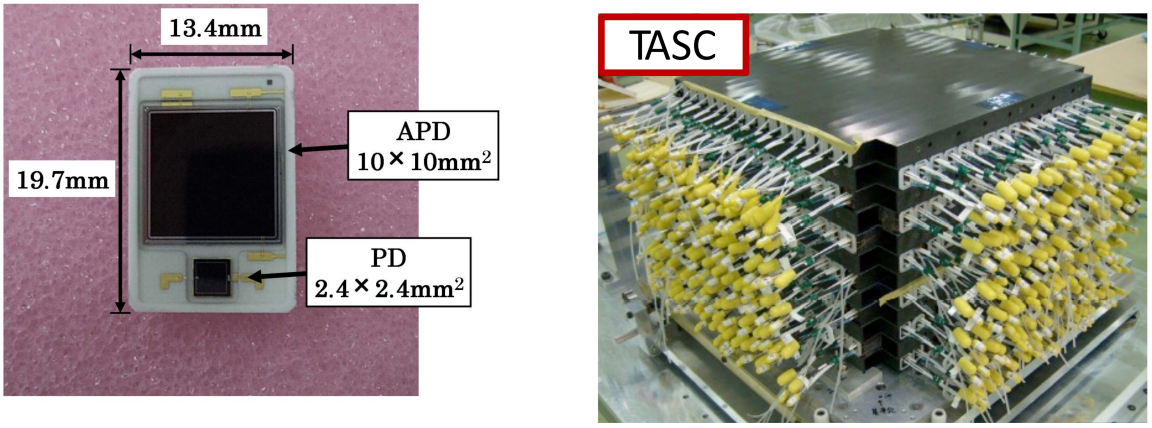

Figure 2.4. *Left: dual APD/PD package [65] used for the read-out of the PWO logs. Right: picture of the CALET TASC.*

The TASC is a homogeneous electromagnetic calorimeter made of 192 Lead-Tungstate (PWO) "logs" ($20\times19\times320$ mm^3) arranged in 12 layers, alternatively oriented in the X and Y directions. Since the Moliére radius of the PWO is about 2 cm, in each layer at

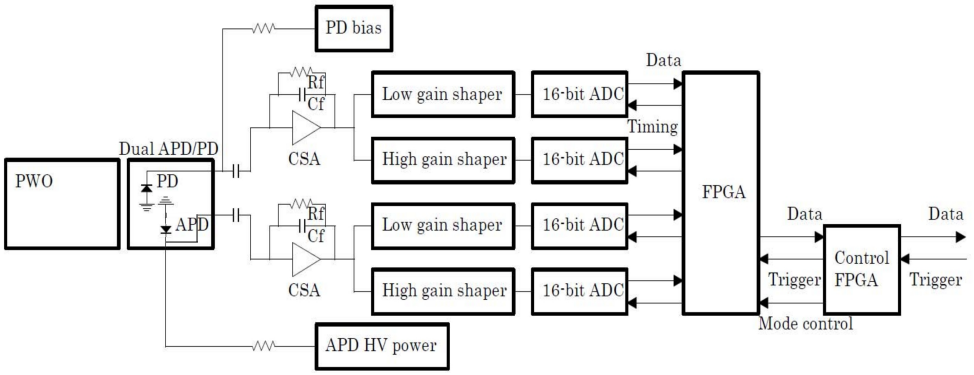

Figure 2.5. *A block diagram of the front-end circuit for the CALET-TASC.*

least the 90% of the electromagnetic shower is contained in 3 logs. The logs in the top layer are read-out by PMTs, in order to achieve a fast response since these signals are involved in the CALET trigger logics, while a dual photodiode/avalanche-photodiode (APD/PD) system is used for the read-out of the remaining layers. The right panel of fig. 2.4 displays the APD/PD package. The effective area of the APD is 20 times larger than the one of the PD and the APD has a gain of 50, thus the output signal of the APD is about one thousand times larger than that of the PD. Furthermore, each signal from the APD and the PD is amplified by two front-end circuits with different gains so a dynamic range of 10^6 for read-out of the PWO is obtained. The block diagram of the front-end circuit is shown in fig. 2.5. The outputs of the APD/PD are directly connected to two different Charge Sensitive Amplifiers (CSAs), which amplify the signals from each photo-diode. Two shaping amplifier circuits, with different gains, process the CSA output. Each shaping amplifier has two sections for each input channel with a gain ratio of 30:1, each one is then digitized by a 16-bit Analog to Digital Converter (ADC).

The right panel of fig. 2.4 shows a picture of the TASC. This device is specifically designed to measure the energy of incident particles with excellent energy resolution: $\sim$ 2% for $e^{\pm}$ and γ rays above 100 GeV, $\sim$ 40% for 1 TeV protons and $\sim$ 30% for nuclei above few hundreds of GeV/amu. Moreover, thanks to the segmentation of the detector, a high proton rejection power can be achieved by means of topological shower analysis, sufficient to keep the proton contamination below few percent in the observation of CR electrons up to 1 TeV. A precise description of the expected proton contamination and the energy resolution for electrons is discussed in §4.

The TASC layers are named "TASCX1, TASCY1, ..., TASCX6, TASCY6" with the same convention used for the IMC.

The total geometrical factor of CALET, defined in [69] is about 1040 cm^2sr, see §4.1 for a precise description and definition of the CALET acceptance and geometrical factor involved in the electron analysis.

2.2 The trigger logics

The CALET trigger logics is based on the coincidence of trigger counter signals that are generated by the discrimination of the analogical signals from several detector components. The analogical signals involved in the trigger logic and used as input of Thresholds Discriminator (TD) circuits are listed below.

- T_{CHDX} (T_{CHDY}): sum of the signals of the paddles of the CHDX (CHDY).
- T_{IMCX12} (T_{IMCY12}): sum of the signals of the SciFis of IMCX1 and IMCX2 (IMCY1 and IMCY2).
- T_{IMCX34} (T_{IMCY34}): sum of the signals of the SciFis of IMCX3 and IMCX4 (IMCY3 and IMCY4).
- T_{IMCX56} (T_{IMCY56}): sum of the signals of the SciFis of IMCX5 and IMCX6 (IMCY5 and IMCY6).
- T_{IMCX78} (T_{IMCY78}): sum of the signals of the SciFis of IMCX7 and IMCX8 (IMCY7 and IMCY8).
- T_{TASCX1}: sum of the signals of the logs of TASCX1.

The CALET trigger configuration listed below are defined by properly combining the discriminating signals.

High Energy Trigger (HET) This is the main trigger mode for CALET and it targets high-energy electrons and gammas above 10 GeV with high efficiency (see §4.6.1 for a precise description of the trigger efficiency). This trigger configuration requires a large energy deposit in the middle section of the detector like the one given by high-energy electromagnetic showers starting in the tungsten layers of the IMC. An event triggers the HET if both T_{IMCX78} and T_{IMCY78} are above 30 MIP and T_{TASCX1} is $>$ 90 MIP, where "MIP" indicates the energy deposit in the corresponding detector, i.e. a

SciFi for the IMC and a PWO log for TASC, by a vertical Minimum Ionizing Particle of charge —Z—=1. This configuration selects almost all the high-energy showers started in the IMC (and CHD), while it rejects most of those starting in the TASC. As a result, it is possible to maximize the trigger efficiency for the high-energy electrons, since the IMC thickness is about 3 X_0 and thus a large fraction of the electron showers start in the IMC itself, while strongly suppressing the low-energy particles. The proton and nuclei component is also suppressed since the thickness of the IMC is $\sim 0.2\ \lambda$ (where λ indicates the proton interaction length), thus only a small fraction of hadronic showers starts in the IMC.

Low Energy Trigger (LET) This trigger configuration is designed for the detection of low-energy electrons and gammas. The logic is the same of the HET but with smaller thresholds, in order to select electromagnetic showers in the range $1 - 50$ GeV. This trigger requires T_{IMCX78} and T_{IMCY78} signals above ~ 2.5 MIP and T_{TASCX1} greater than ~ 7 MIP. The LET can be modified with respect to the standard configuration in order to reject gamma events by requiring that all the trigger signals related to the IMC and CHD are above ~ 0.7 MIP. This trigger mode, named "Low Energy Trigger electron" (LETe) is useful for the measurement of the low-energy electron flux by employing a less restrictive selection with respect the HET.

Single Trigger (ST) This trigger mode is dedicated to penetrating charged particles for the detector calibration. It requires an energy deposit greater than 0.7 MIP (in order to select mainly protons) or 2 MIP (in order to select helium or heavier nuclei) for all the signals of the TDs. An additional software selection can be used in order to reject events with high-energy deposit in TASC, selecting not-interacting particles only.

All the described trigger modes can be modified by requiring a large (> 50 MIP) deposit in the CHD, in order to select heavy nuclei; the resulting configurations are referred to as "Heavy Ion Triggers".

2.3 The CALET main scientific goals

The main CALET scientific objective is the measurement of the electron spectrum up to the multi-TeV region. As described in §1.3.1 it is a sensitive probe of nearby high-energy cosmic accelerators. Thanks to its excellent energy resolution and capability

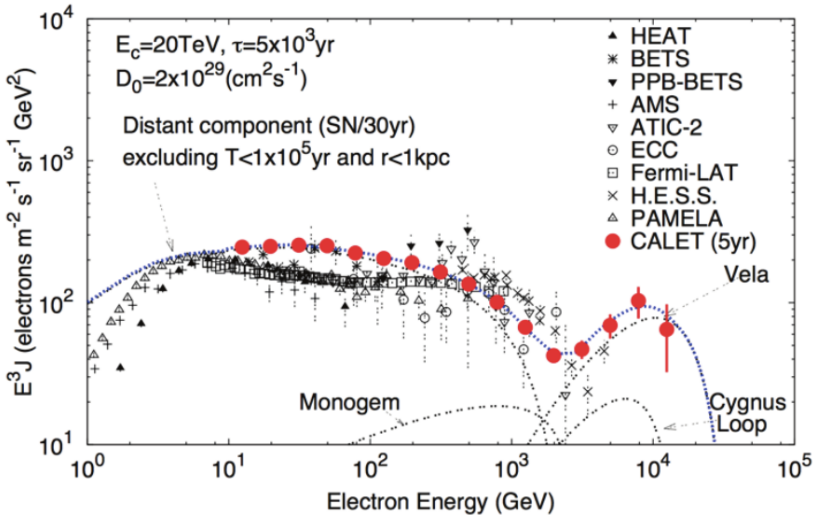

Figure 2.6. *Anticipated CALET measurement of the electron spectrum (red point) based on a model of the electron spectrum (dotted blue line), including the contribution from some known nearby objects, and compared with other measurements [61].*

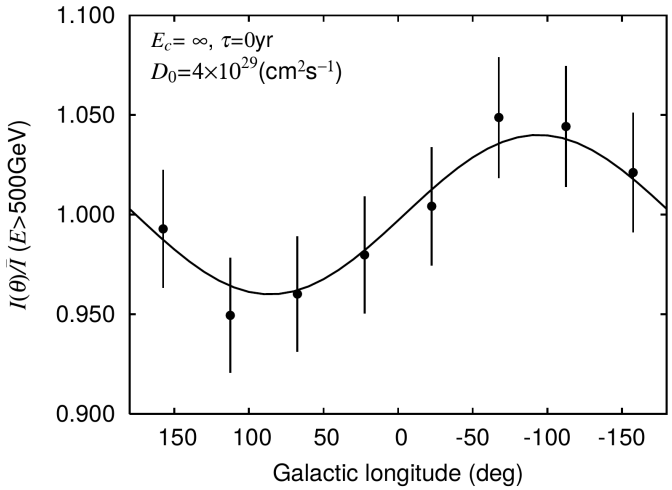

Figure 2.7. *Anticipated CALET measurement of the electron anisotropy above* 500 GeV *due to Vela [71].*

to discriminate electrons from hadrons, described in §4, CALET is able to investigate possible spectral structures by detecting very high-energy electrons and potentially provide experimental evidences of the presence of a nearby CR sources. As an example, fig. 2.6 shows the anticipated CALET measurement of the electron spectrum for a 5 years of exposure based on the model developed in [20] and briefly described in §1.3.1; it features an increase of the electron flux at high-energy due to the electrons ejected from the Vela SNR. In addition, CALET can provide a direct measurement of the electron anisotropy in high-energy region. As described in [71], CALET is capable

to detect the flux anisotropy due to the candidate CR source Vela. According to [20] the intensity of the electron flux above 500 GeV depends on the galactic longitude: fig. 2.7 shows the intensity of the expected electron flux in different bins of galactic longitude $I(\theta)$ divided by the mean intensity $\bar{I}$.

Moreover, the CALET measurement is also important for the search of Dark Matter signatures in the electron flux. As described in [72], by combining the measurement of the total electron+positron flux by CALET with the positron fraction data from the AMS-02 experiment, it will be possible to significantly constrain models of Dark Matter annihilating in the galactic halo.

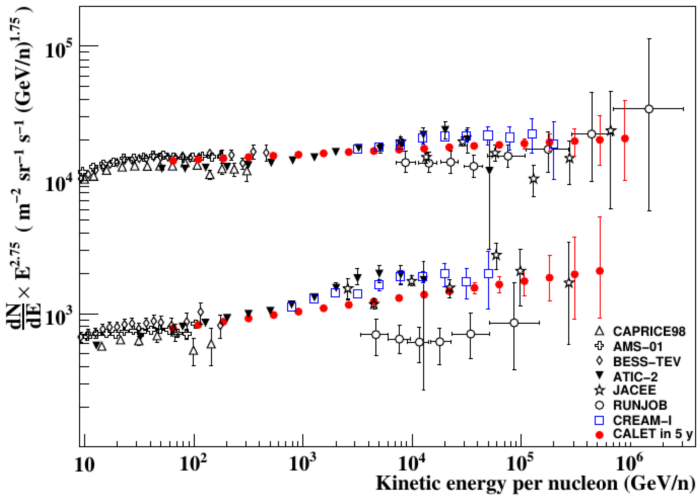

Figure 2.8. *Anticipated CALET measurement of the proton (upper) flux and helium (lower) flux (red point) compared with some experiment results.*

Another important scientific objective is the direct measurement of the high-energy spectra of individual CR nuclei up to hundreds of TeV per nucleon. This provides important complementary information to the one derived from electron observations for understanding CR physics. As described in §1.2 charge-dependent spectral softening in this energy region are expected by the SN diffusive shock acceleration model. In §1.5.1 the recent direct measurement of proton and helium flux above 10 TeV are discussed: in this energy region, only data from balloon experiments are available. Thanks to the long exposure time and the large acceptance, the CALET mission is capable to provide more precise direct measurement of CR nuclei spectra in an extended energy range. It can also investigate spectral features or deviations from a pure power-law spectrum, as observed by PAMELA [36] and AMS-02 [37][38] for proton and helium

spectra. The anticipated CALET measurement of the proton and helium spectra for 5 years of exposure time and assuming single power-law spectra is shown in fig. 2.8.

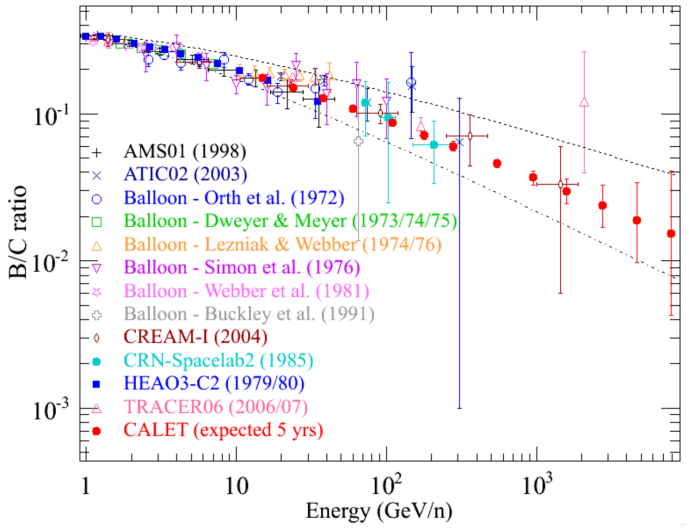

Figure 2.9. *Anticipated CALET measurement of the B/C ratio (red points) compared with other measurements.*

Furthermore, information on the CR propagation can be obtained by direct measurement of the secondary-to-primary flux ratios, most notably Boron/Carbon, as described in §1.3. The anticipated B/C ratio for 5 years of CALET exposure time is shown in fig. 2.9. Taking advantage of its long exposure in space, the CALET mission will provide new data in order to extend the more recent B/C measurement (see §1.5.3) above 1 TeV per nucleon.

In addition, to precise measurement of the CR electron and nuclei spectra, the CALET calorimeter is capable of gamma-ray observations in the energy range from 1 GeV (by employing the LET trigger mode) to 10 TeV (with the HET mode). Its excellent energy resolution and good angular resolution will allow for accurate measurements of diffuse gamma-ray emission and detection of bright sources. CALET will also monitor X-ray and gamma-ray transients in the energy region 7 keV to 20 MeV with the CGBM [62]. It will extend GRB studies carried out by other experiments (e.g. Swift and Fermi-LAT) and provide added exposure when the other instruments will not be available or pointing to a different direction. Furthermore, when a GRB triggers the CGBM, the calorimeter trigger configuration is automatically switched to LET mode, in order to optimize the observation of gamma-rays with energy > 1 GeV.

Thanks to the combination of the calorimeter and the CGBM observations, CALET is capable of detecting high-energy photons possibly associated with a burst event. It is also able to search possible electromagnetic counterparts of gravitational wave events, as described in [62].

Chapter 3

CALET GEANT4 simulation: implementation and validation

MC simulations are a very important tool for particle physics experiments. For CALET these are used, in parallel with the flight data, for the calculation of event selection efficiencies and contaminations due to possible background events. The first MC simulation developed for the CALET experiment was based on the EPICS package [70], implementing a simplified geometry of the CALET detector. This geometry includes just the active materials of the calorimeter, i.e. CHD paddles, IMC SciFis and TASC PWO logs, and the IMC tungsten layers as passive material. This EPICS simulation has been employed for a preliminary investigation of the CALET performance. In order to validate the EPICS results, two independent MC simulations, based on FLUKA [74] and GEANT4 [73] packages, have been developed with the same simplified geometry. A preliminary comparison among the three MC simulations is described in §4.2 of [75], focusing on the shower development in the TASC and on the electron/proton discrimination.

A more complex geometry, named "CALETCAD", that precisely reproduces all the material of the CALET detector, including all the passive materials of supporting structures, has been initially implemented in EPICS by employing the CAD project of the real detector. Afterwards the same geometry, with some simplifications, has been replicated in both FLUKA and GEANT4. The development of the CALETCAD geometry in GEANT4 with different comparisons between GEANT4 and the other MC simulations was addressed within this Ph.D. work.

3.1 CALETCAD simulation with GEANT4 package

GEANT4 [73] is a software toolkit, written in C++, for the simulation of the passage of particles through matter. It can be used in several applications, from particle physics to medical physics and radiation protection. The description of the geometry of the detectors, including the position and the material of each volume, is coded in C++ by using the GEANT4 API. For each event, information about the passage of particles trough each detector volume (i.e. the energy deposit, the impact point of the particle on the detector element, etc.) can be retrieved and saved in the output file.
For the implementation of the CALETCAD geometry in GEANT4 the shape and the size of the CALET structures have been extracted from the EPICS geometry configuration file, which in turn has been created in conformance with the complete CAD model of the instrument. Some volumes have been simplified with respect to the EPICS geometry, especially those not crossed by particles inside the CALET acceptance (see §4.1). The most important differences between the GEANT4 and the EPICS geometries are listed below.

- **Honeycomb supporting structures**. Below each CHD and IMC layers, a honeycomb aluminium supporting structure is present. These structures are crossed by particles in the CALET acceptance. The implementation of a detailed honeycomb structure in GEANT4 would consist of a very complicated set of volumes, which have a impact in terms of computation power for particle tracking and memory consumption; for this reason a simplified "mean honeycomb" has been implemented. By taking into account that the mean thickness of the honeycomb supporting structures is very small (about 0.15 X_0 in total with respect to the total thickness of the IMC which is equal to 3 X_0), these are replaced by homogeneous aluminium blocks with a density equal to the mean density of the honeycomb volumes, of about 0.24 g/cm^3.

- **Lateral and bottom aluminium panels of TASC**. The lateral and bottom sides of the TASC are surrounded by complex thin aluminium structures. Since these materials are not crossed by particles inside the CALET acceptance, the shape of these structures has little to no impact in the simulation of the interesting events. These panels are approximated with single aluminium boxes with a thickness equal to the mean thickness of the real structures.

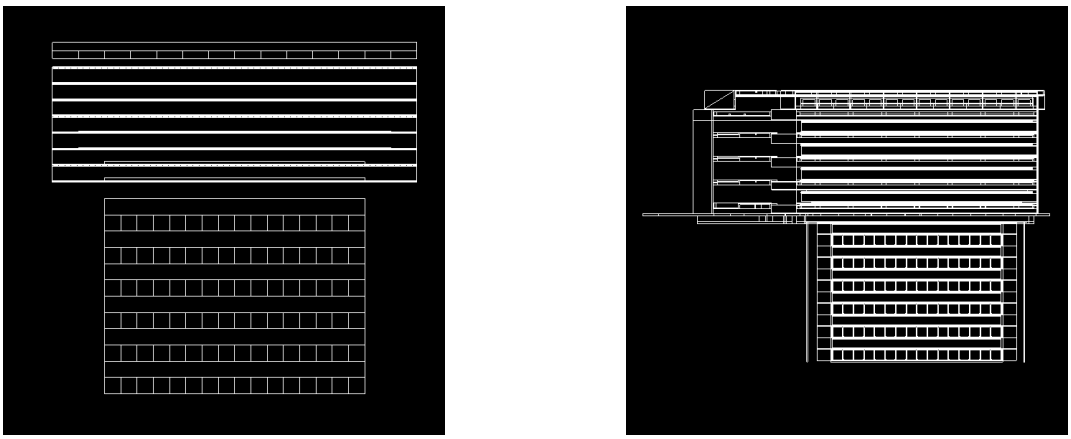

(a) *CALET simplified geometry.* (b) *CALETCAD geometry.*

Figure 3.1. *Images of the simplified geometry (left panel) and CALETCAD geometry (right panel) implemented in GEANT4, X view.*

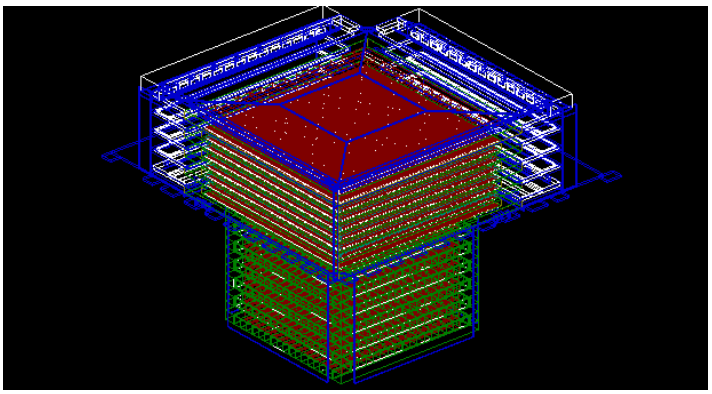

Figure 3.2. *Image of the CALETCAD geometry implemented in GEANT4. Here different materials are drawn with different colours: aluminium (blue), active materials (red), carbon fibre supporting structures (green), honeycomb structures (yellow) and other materials (white). In this image, the IMC tungsten layers are not visible.*

A comparison between the X view of the CALETCAD and the simplified geometry implemented in GEANT4 is shown in fig. 3.1: these images are extracted from the standard GEANT4 tool for the visualization of geometries. These images show that the CALETCAD geometry is more complex and detailed with respect to the previous one. Fig. 3.2 shows the CALETCAD geometry from a different angle: in this image, the colours represent different materials as described in the caption of the figure.

3.2 Monte Carlo performance benchmarks

The results discussed in this chapter concerning the GEANT4 simulations are obtained with the version 09.06.p02 and by employing the physics lists FTFP˙BERT. This specifies the hadronic models involved in the simulation and is recommended for high-energy particle calorimetric applications [76]; it includes the high-energy inelastic scattering of hadrons by nuclei using the Fritiof string model [77] applied to incident nucleons, pions, kaons and hyperons from $\sim$ 5 GeV/n to 100 TeV/n and the Bertini-style [78] cascade for hadrons below $\sim$ 5 GeV/n.

In order to validate the CALETCAD GEANT4 simulation and check the implementation of the CALETCAD geometry, comparisons with FLUKA (version 2011.2c.6) and EPICS (version 9.167, COSMOS 7.645) simulations were carried out. The output of the three simulations is written in a common format, named "UnifiedOutput", in order to apply the same analysis algorithms to data generated in different ways. The UnifiedOutput format contains information about the energy deposit in active materials, in tungsten, and some features of the generated particles like the initial trajectory, the particle type and momentum.
The common benchmarks used for comparison involve protons and electrons simulated at fixed energy: 10 GeV, 100 GeV, 1 TeV and 10 TeV. These particles are simulated with a vertical incident trajectory (parallel to the Z axis of CALET). The generation surface is a plane (4×4 cm^2) placed on the top of detector, with the centre of the plane coincident with the centre of the CHD. The comparison among the simulations involved the following variables:

- total energy deposit in the active material (scintillators) of the CHD, IMC and TASC,
- longitudinal profile of the shower in IMC and TASC,
- lateral profile of the shower in IMC and TASC,
- first hadronic interaction point, only for protons.

For these comparisons the longitudinal profile of the shower in TASC (and IMC) is simply defined as the mean energy deposit in the TASC (IMC) layers as a function of the depth, i.e. the Z coordinate of the layer. For the lateral profile, the TASC (IMC) layer with the maximum energy deposit is selected and the energy deposit in

each log (SciFi) of this layer is plotted as a function of the distance of the centre of the log (SciFi) from the intersection of the particle trajectory generated by the simulation with the layer. The position of the point of the first hadronic interaction is retrieved from the MC truth information; the distribution of the Z coordinate of this point is used for the comparison.

For these benchmarks an event selection called *"software HET"* (SW-HET) is applied in order to roughly replicate the hardware HET described in §2.2. The channels involved in the SW-HET are the same in the hardware HET but the thresholds are slightly higher (100 MIP for the TASC and 40 MIP for the IMC). This cut is effective in order to avoid the need for an accurate simulation of the discriminator thresholds implemented in the electronics and it has a high efficiency for electrons ($> 95\%$ for electrons at energies > 30 GeV) while it rejects about 60% of protons at 100 GeV. A more precise discussion of the MC efficiency of this selection is presented in §4.

3.2.1 TASC energy deposit benchmarks

Fig. 3.3 and 3.4 show the total energy deposit in TASC obtained with the EPICS, GEANT4 and FLUKA MC simulations for protons and electrons respectively. The 4 energies used for these benchmarks are shown from the top left panel (10 GeV) to the bottom right one (10 TeV). The counts divided by the total number of events are on the Y axis, the total energy deposit from MC simulations in TASC on the X axis. An overall good agreement among the simulations is present for both protons and electrons and the differences of the position of the maximum point of the distributions among the simulations are $\leqslant 5\%$ for all the energies. The shape of the electron distributions are in good agreement while for protons small discrepancies are present in GEANT4 distributions with respect to FLUKA and EPICS: EPICS and FLUKA employ the same hadronic interaction model, DPMJET-III [79], while in GEANT4 a different one is implemented, thus some differences in proton distributions are expected. The distribution of the total energy deposit in TASC for electrons above 100 GeV consists of a narrow peaks and a low-energy tail: the latter is due to electrons with trajectories that intercept the passive materials in TASC that separates the PWO logs. In these benchmarks, the number of those events is quite big because the generated particles have vertical directions. In the real situation of the measurement of CR electrons, where the particle direction is isotropic, this effect does not affect so much the energy

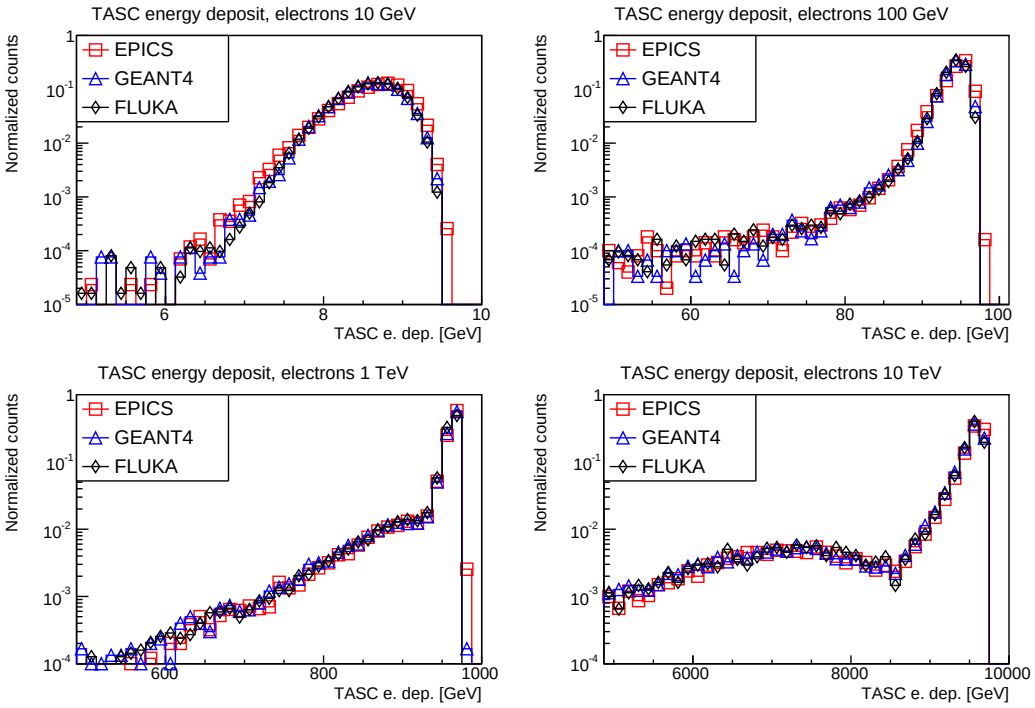

Figure 3.3. *Total energy deposit in TASC for electrons at different energies obtained with EPICS (red), GEANT4 (blue) and FLUKA (black) MC simulations.*

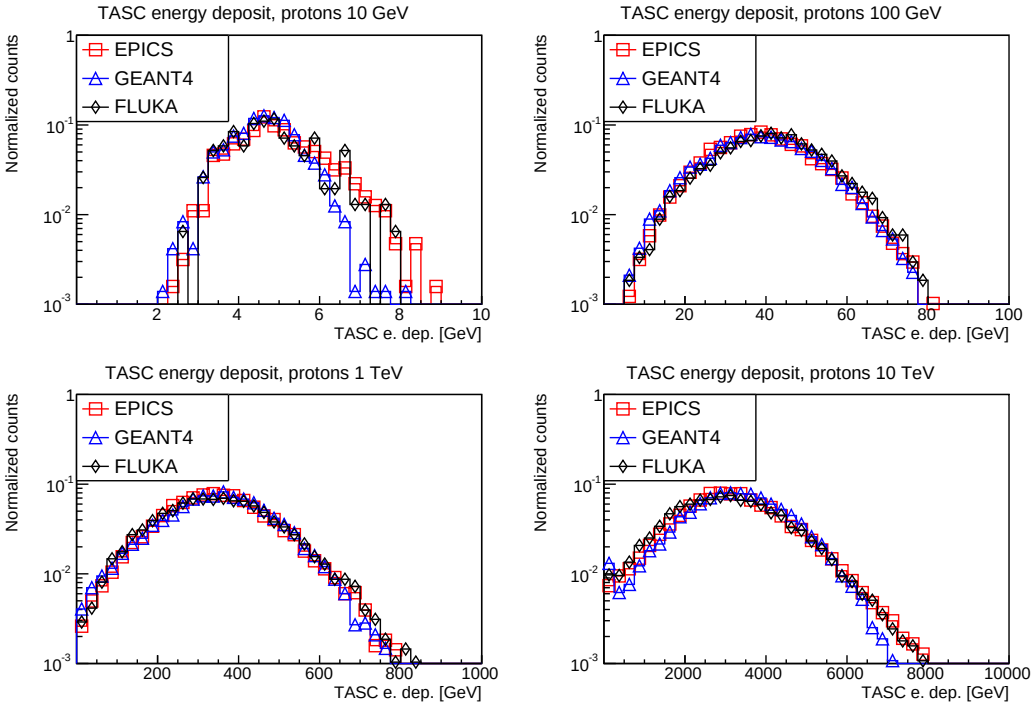

Figure 3.4. *Total energy deposit in TASC for protons at different energies obtained with EPICS (red), GEANT4 (blue) and FLUKA (black) MC simulations.*

resolution (see §4.5). The distribution for protons is larger than electrons as expected for this kind of calorimeter, and the energy resolution estimated with the Root Mean Square (RMS) of the distribution is about 35% for protons at 1 TeV.

The longitudinal distribution for electrons and protons are shown in fig. 3.5 and 3.6. The X axis shows the Z coordinate of the TASC layer and the Y axis the mean of the energy deposit in each layer divided by the mean of the total energy deposit in TASC. Fig. 3.7 and 3.8 show the lateral profile of the shower in the TASC layer with the maximum energy deposit. The X axis shows the distance of the centre of the TASC log from the intersection of the particle trajectory with the TASC layer while the Y axis shows the mean of the energy deposit in the log divided by the mean of the total energy deposit in the layer. An overall reasonable agreement is shown in both the longitudinal and lateral distribution for both protons and electrons. The electron longitudinal profiles are shorter than the proton ones, and the lateral profiles are narrower around zero as expected for electromagnetic showers.

In conclusion, for the TASC, big discrepancies among the simulations are not found, but some small differences are present, especially in proton benchmarks. These discrepancies are probably related to differences in the hadronic models employed in the simulations since the electrons benchmarks show a better agreement than the proton ones.

3.2.2 IMC and CHD energy deposit benchmarks

Fig. 3.9 and 3.10 show the total energy deposit for protons and electrons in IMC while fig. 3.11 and 3.12 show the total energy deposit in the CHD. The agreement among the simulations is quite good at 10 GeV while noticeable discrepancies are present especially at 1 TeV and 10 TeV for both protons and electrons. The overall agreement between FLUKA and GEANT4 is reasonable, a considerable discrepancy is present only in the CHD for electrons at 10 TeV. The EPICS simulation features instead a different behaviour: the mean energy deposit in the CHD and IMC is systematically smaller than those obtained with FLUKA and GEANT4. The difference between the position of the maximum of the CHD energy deposit estimated with EPICS with respect to FLUKA and GEANT4 is less than 10% at 10 GeV but it increases with energy and becomes greater than 40% at 10 TeV for both protons and electrons. A similar

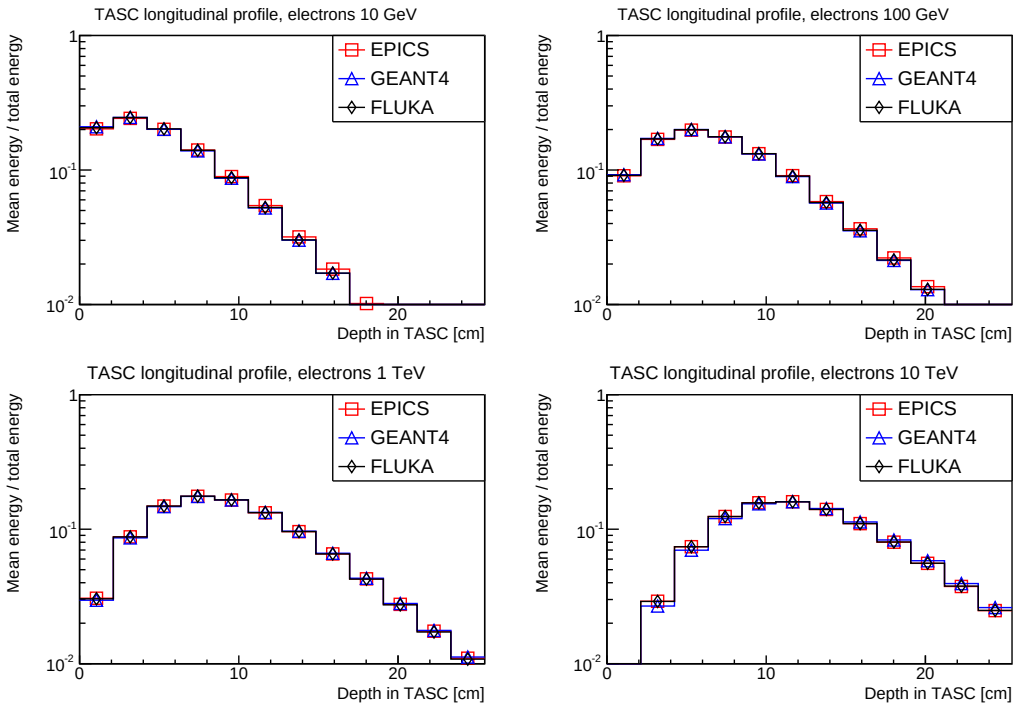

Figure 3.5. *Longitudinal profile of the shower in TASC for electrons at different energies obtained with EPICS (red), GEANT4 (blue) and FLUKA (black) MC simulations.*

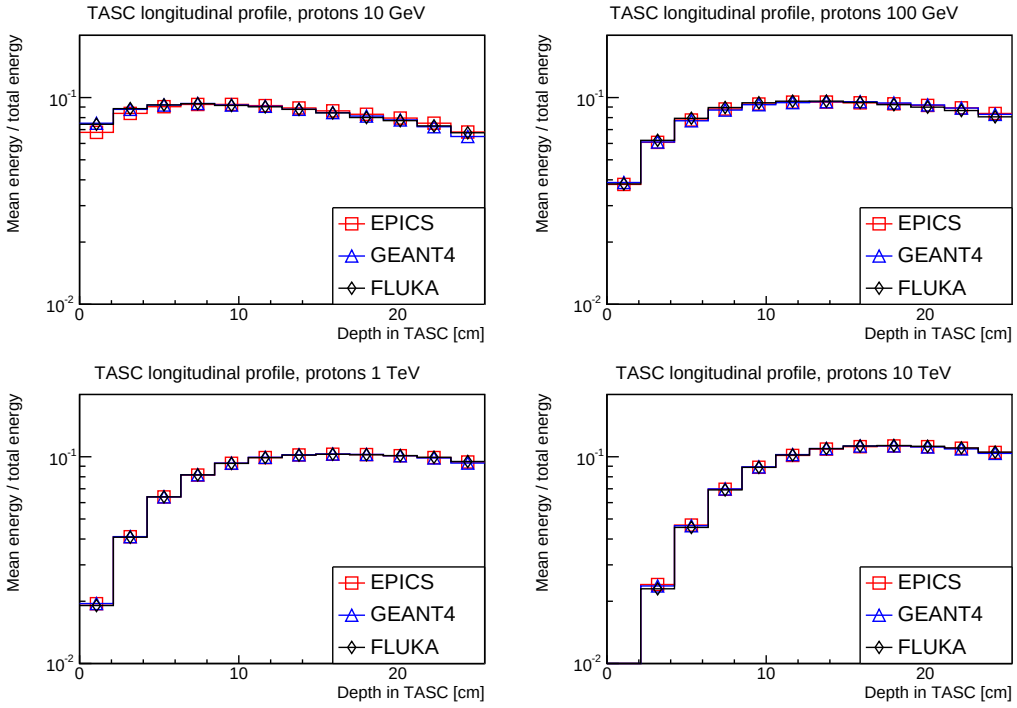

Figure 3.6. *Longitudinal profile of the shower in TASC for protons at different energies obtained with EPICS (red), GEANT4 (blue) and FLUKA (black) MC simulations.*

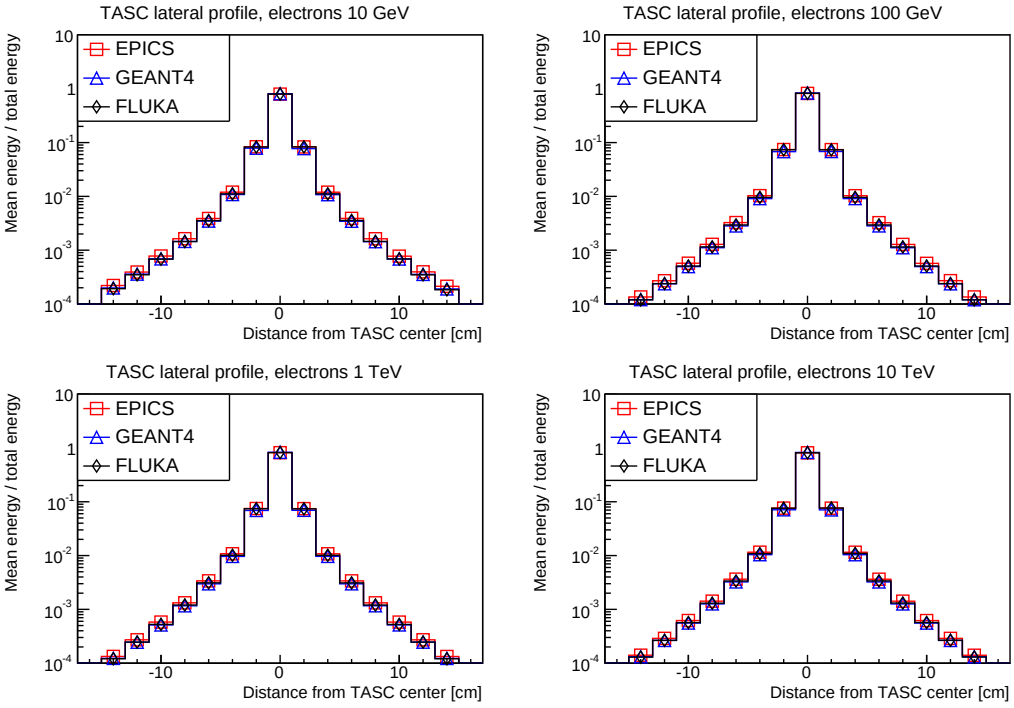

Figure 3.7. *Lateral profile of the shower in TASC layer with the maximum energy deposit for electrons at different energies obtained with EPICS (red), GEANT4 (blue) and FLUKA (black) MC simulations.*

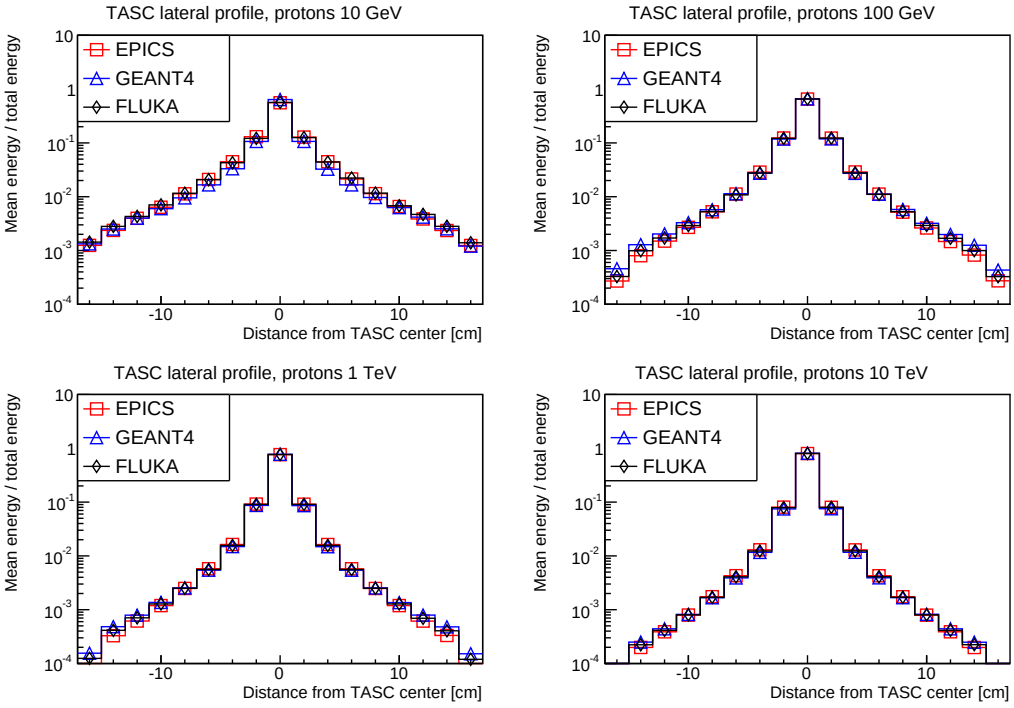

Figure 3.8. *Lateral profile of the shower in TASC layer with the maximum energy deposit for protons at different energies obtained with EPICS (red), GEANT4 (blue) and FLUKA (black) MC simulations.*

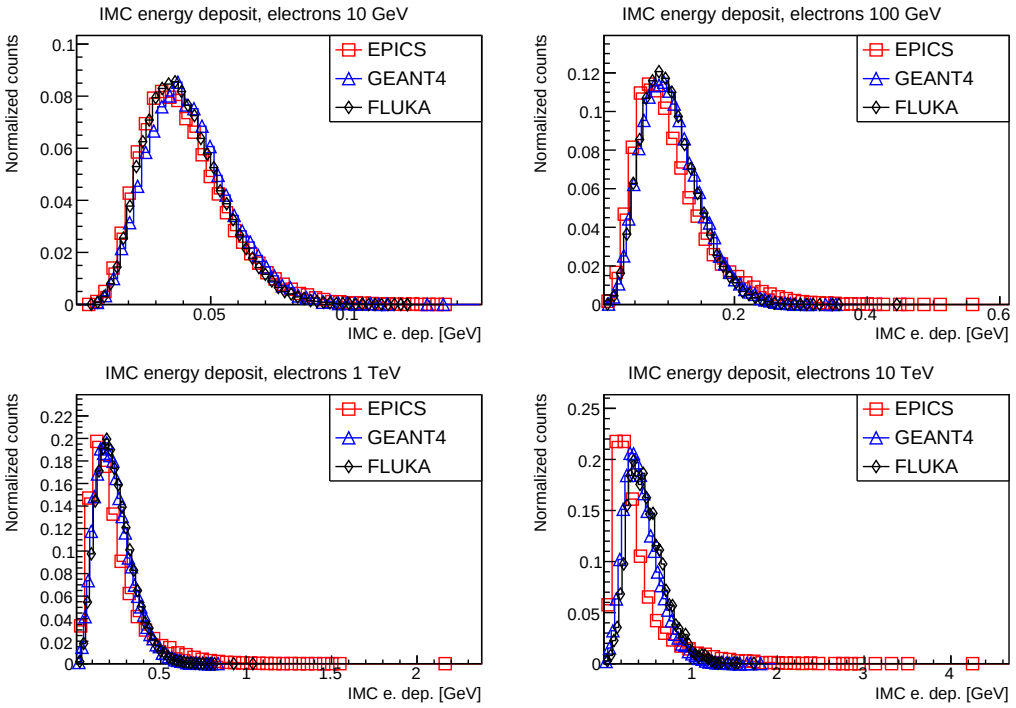

Figure 3.9. *Total energy deposit in IMC for electrons at different energies obtained with EPICS (red), GEANT4 (blue) and FLUKA (black) MC simulations.*

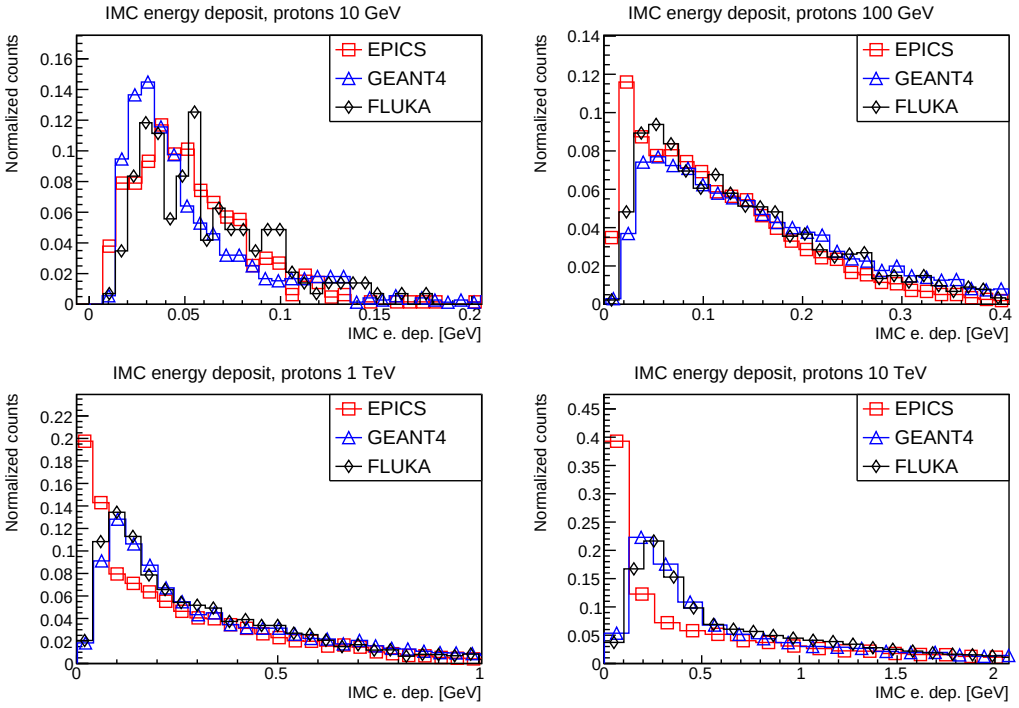

Figure 3.10. *Total energy deposit in IMC for protons at different energies obtained with EPICS (red), GEANT4 (blue) and FLUKA (black) MC simulations.*

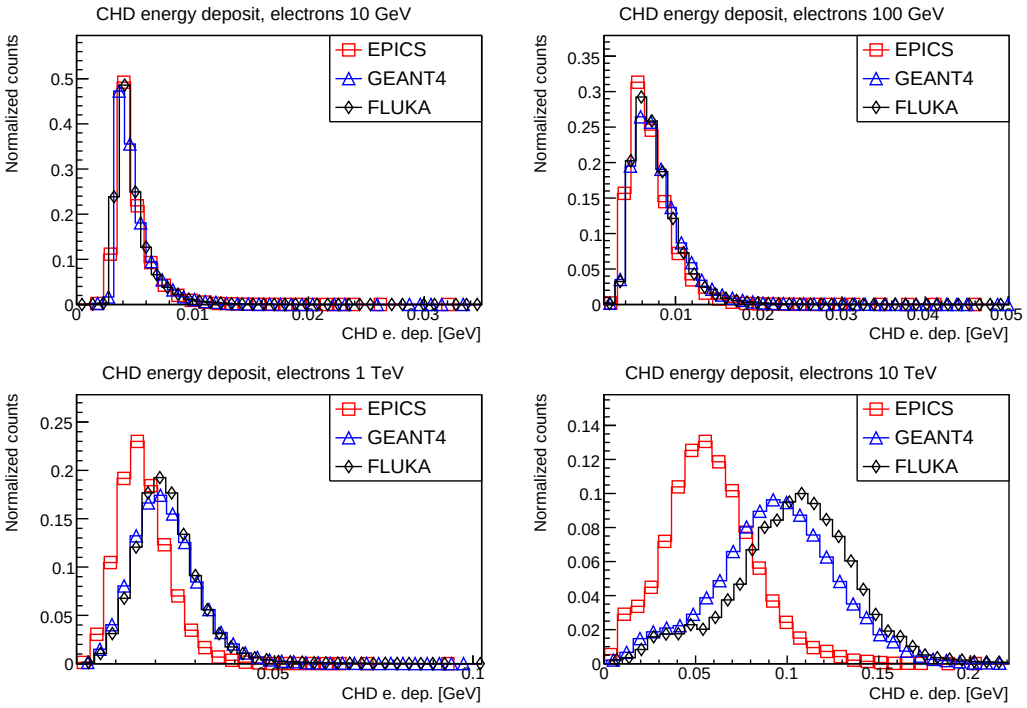

Figure 3.11. *Total energy deposit in CHD for electrons at different energies obtained with EPICS (red), GEANT4 (blue) and FLUKA (black) MC simulations.*

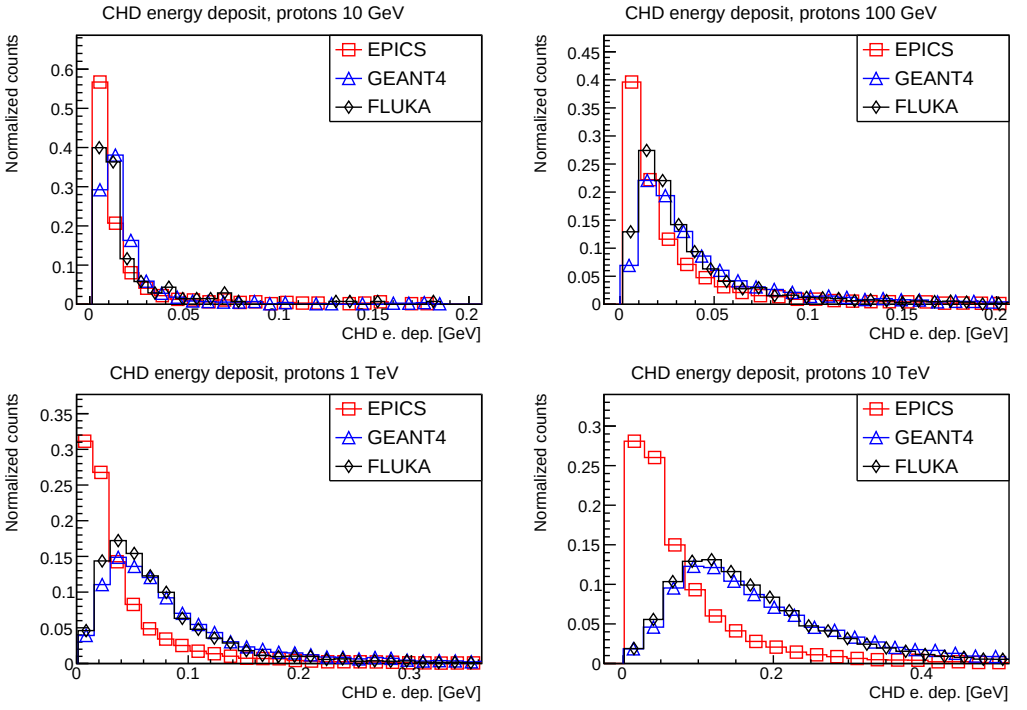

Figure 3.12. *Total energy deposit in CHD for protons at different energies obtained with EPICS (red), GEANT4 (blue) and FLUKA (black) MC simulations.*

trend is found for the IMC.
Furthermore, the longitudinal profile, shown in fig. 3.13 and 3.14, also confirms a discrepancy between EPICS with respect to GEANT4 and FLUKA, especially in the first layers of the IMC.

In order to investigate the origin of these discrepancies, and to exclude the possibility to ascribe them to differences in the implementation of the CALETCAD geometry in GEANT4 and FLUKA with respect to EPICS, the same benchmarks were done with the same simulation package but using the simplified geometry. In the 3 simulations the implementation of this geometry is identical. The advantage of this approach is that this configuration is simple and it is easier to check the consistency of the implemented geometries with respect to the CALETCAD. The analysis with the simplified geometry confirms a reasonable agreement among the MC simulations for the TASC benchmarks as expected. It also shows the same discrepancies in IMC and CHD obtained with the CALETCAD. As an example, the total energy deposit in the CHD by protons and electrons with the simplified geometry is shown in fig. 3.15 and 3.16; this result confirms the discrepancies found with the CALETCAD and suggests that these are not related to the implementation of the complex geometry of the CALETCAD.

The first hypothesis to explain these discrepancies is that the EPICS simulation has a different treatment of the backscattered particles coming from TASC with respect to GEANT4 and FLUKA. The total energy released in CHD (IMC) includes both the energy deposited by the primary particle in the crossed paddles (fibres), and the signals due to backscattered particles in the nearby paddles (fibres). The latter is expected to increase with the primary particle energy. This is consistent with the observed discrepancies, which increase with the particle energies. Furthermore, the IMC longitudinal profile shows a bigger discrepancy in the energy deposit in the first layers than in the last ones. This is consistent with the backscattering hypotheses: the energy deposit on the upper layers is mostly due to the direct ionization of the primary particle, which is relatively small and as such the contribution of the backscattered particles to the benchmark variables is expected to be sizeable. On the contrary, on lower layers the energy deposit is dominated by the big releases given by the particle shower, especially for electrons, and thus the backscattering contribution is expected to be far less important than for the upper layers.

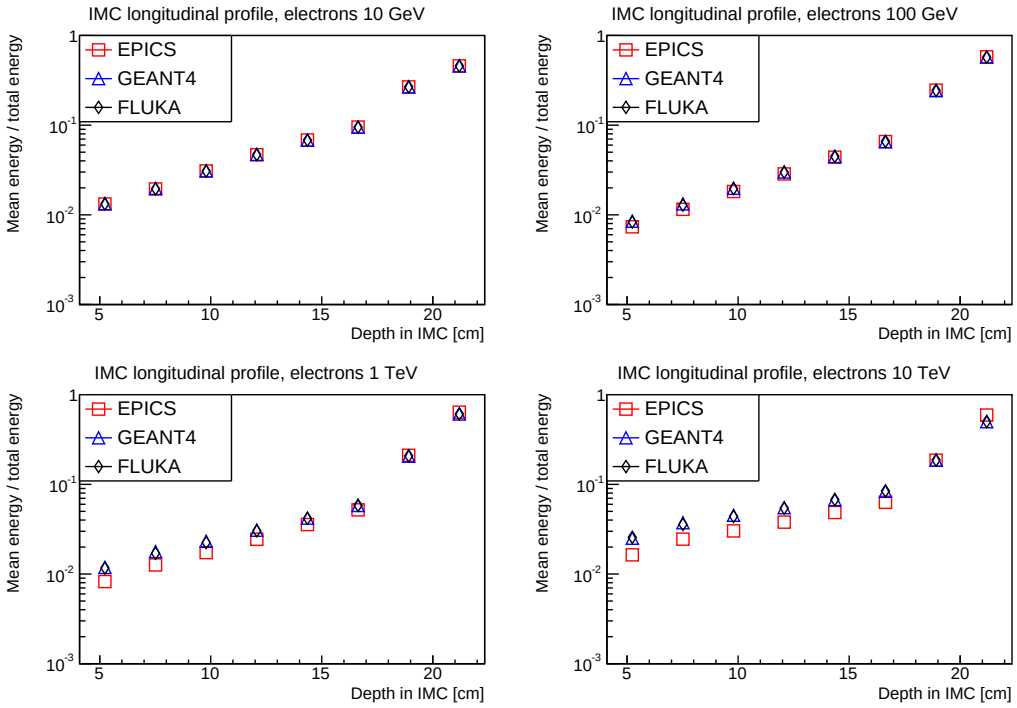

Figure 3.13. *Longitudinal profile of the shower in IMC for electrons at different energies obtained with EPICS (red), GEANT4 (blue) and FLUKA (black) MC simulations.*

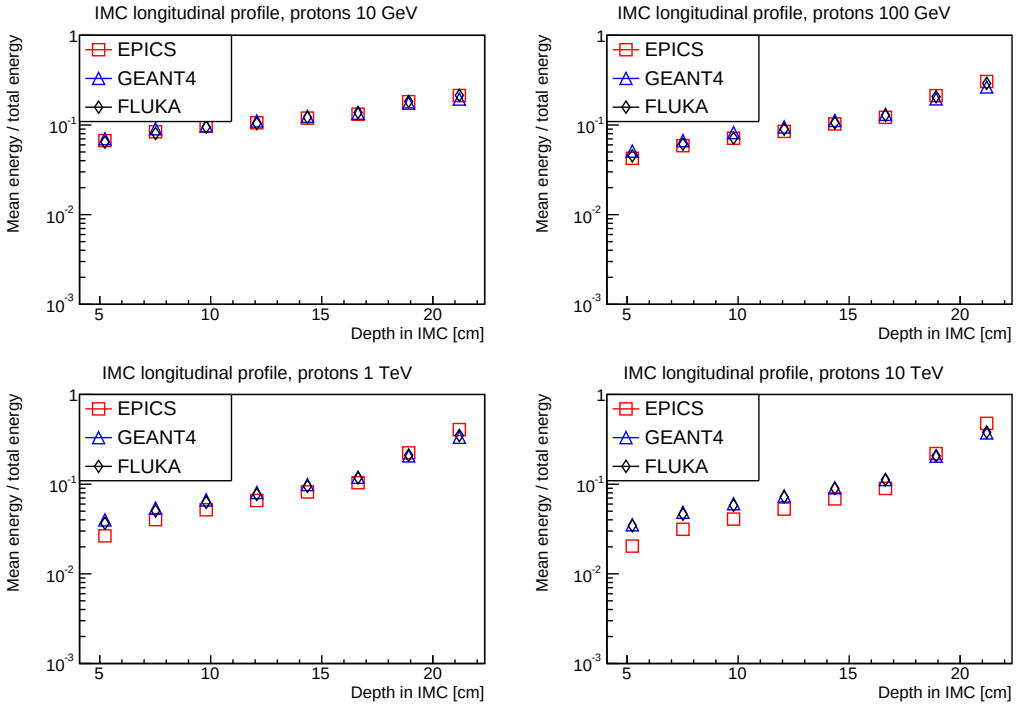

Figure 3.14. *Longitudinal profile of the shower in IMC for protons at different energies obtained with EPICS (red), GEANT4 (blue) and FLUKA (black) MC simulations.*

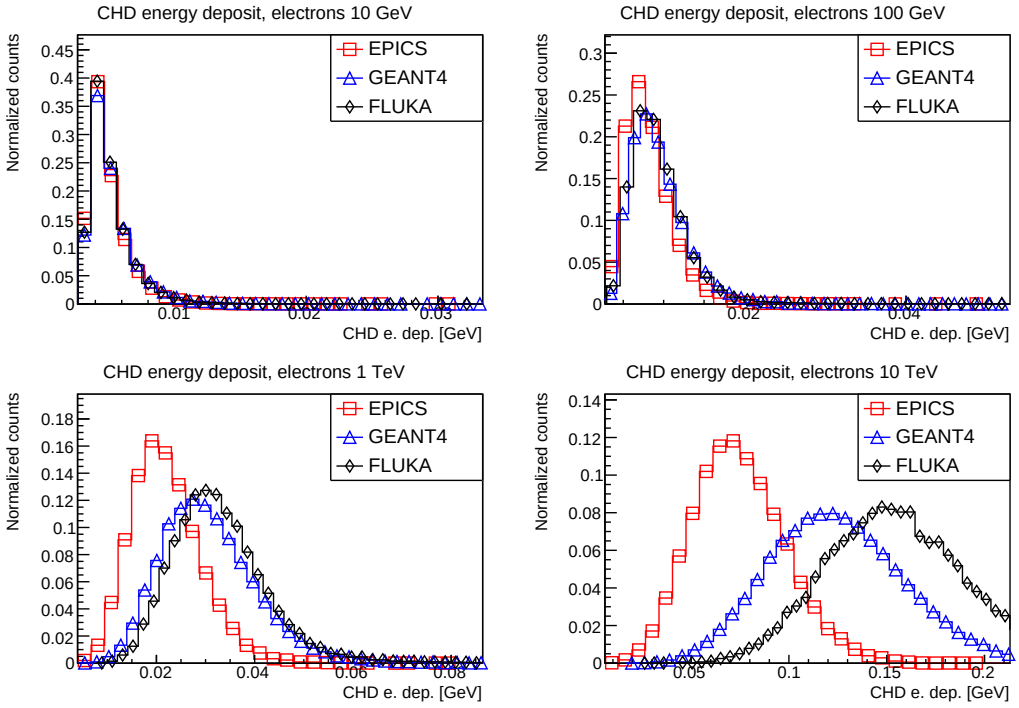

Figure 3.15. *Total energy deposit in CHD for electrons at different energies obtained with the simplified geometry implemented in EPICS (red), GEANT4 (blue) and FLUKA (black) MC simulations.*

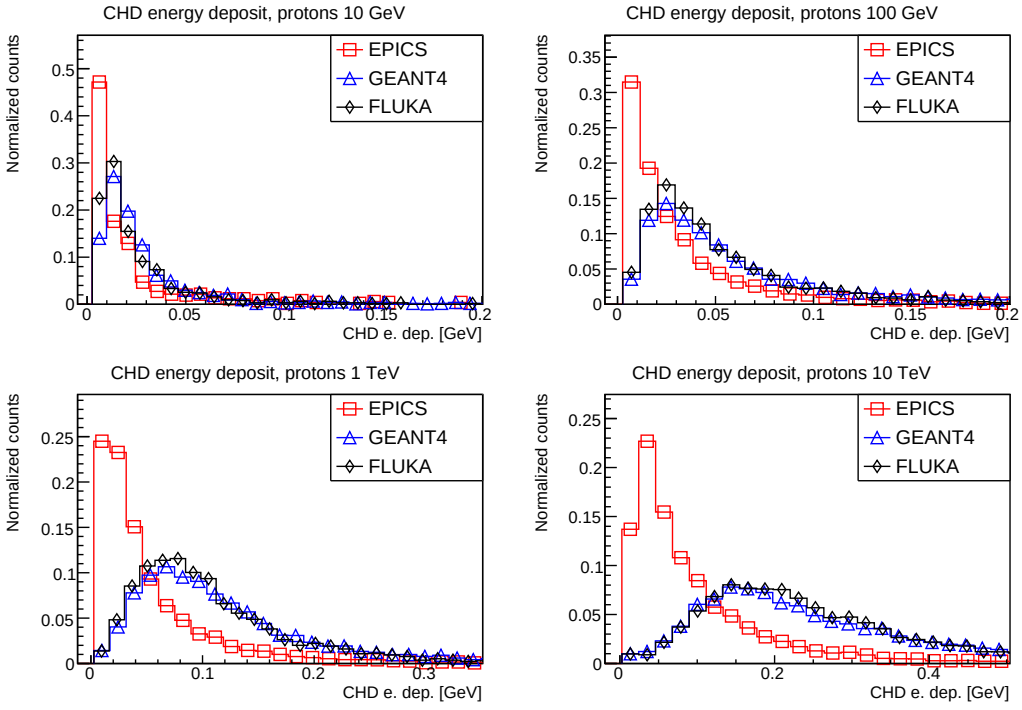

Figure 3.16. *Total energy deposit in CHD for protons at different energies obtained with the simplified geometry implemented in EPICS (red), GEANT4 (blue) and FLUKA (black) MC simulations.*

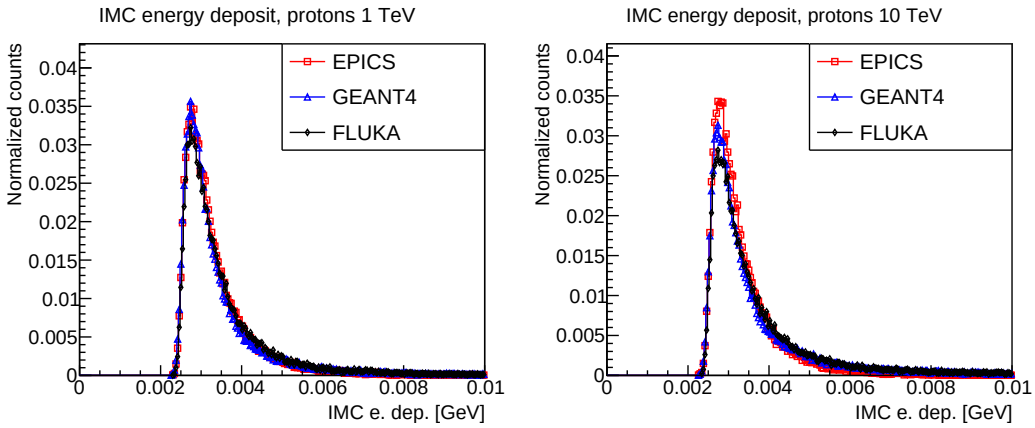

Figure 3.17. *Total energy deposit in IMC for protons at* 1 TeV *and* 10 TeV *obtained with the CALETCAD without the TASC implemented in EPICS (red), GEANT4 (blue) and FLUKA (black) MC simulations.*

To investigate this hypothesis, new simulations with EPICS, FLUKA and GEANT4 were done, using the CALETCAD geometry without the TASC (both passive and active materials). This avoids the production of most of the backscattered particles. By using the same benchmarks with this configuration a good agreement was found up to 10 TeV for protons and electrons, with discrepancies in the position of the maximum of the CHD (and IMC) energy deposit of few percent. As an example, the benchmarks about the total energy deposit in IMC obtained with this configuration for protons at 1 TeV and 10 TeV are shown in fig. 3.17. The result of this comparison features that the treatment of backscattered particles is the main reason of the discrepancies found with the CALETCAD geometry in IMC and CHD, since backscattering is the only way the TASC can affect the benchmark variables on the upper sub-detectors.

3.2.3 First hadronic interaction point

The X axis of fig. 3.18 shows the Z coordinate of the first hadronic interaction point of protons at 1 TeV in the CHD and IMC (left panel) and TASC (right panel). The Y axis shows the number of events for each bin divided the total number of events. For this benchmark the SW-HET cut is not applied in order to study protons with an interaction point in the last layers of the TASC too, otherwise these are completely removed with the SW-HET. The overall agreement among the MC simulations is reasonable, by taking into account that some differences due to the different employed cross-sections are expected. Starting from the left of fig. 3.18, the first bunch of events interacts with the aluminium panel placed at the top of CALET and then it is possible to identify the

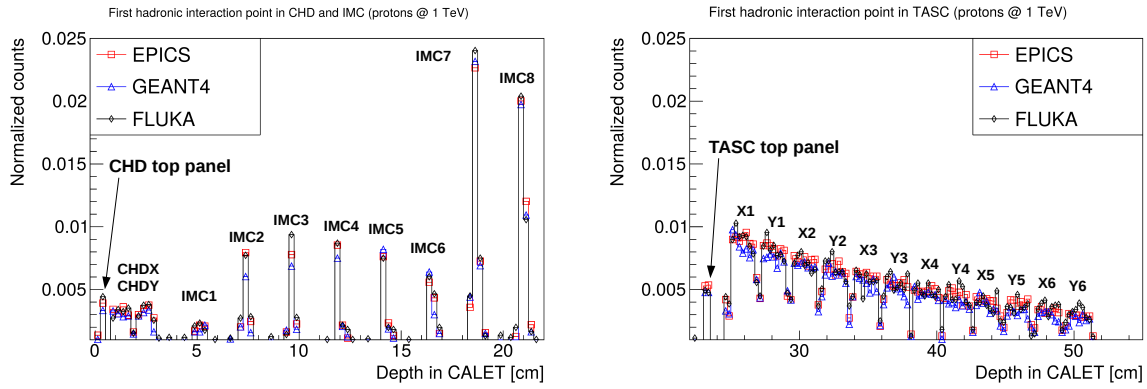

Figure 3.18. *Depth in the CALET detector of the first hadronic interaction point in TASC (right panel) and IMC+CHD (left panel) with EPICS (red), GEANT4 (blue) and FLUKA (black).*

events that interact with the CHDX and CHDY. In the IMC numerous events interacts with the tungsten layers: these are placed above the IMC SciFi layers. The number of events with the interaction point in the last 2 tungsten layers is larger, since the thickness of these layers is greater with respect to the previous ones. The number of particles with the interaction point in the first IMC layer is relatively small because there is not a tungsten layer placed above this layer. In the right panel of fig 3.18 it is possible to identify the aluminium panel placed on the top of the TASC and the TASC layers. The distribution of the first interaction point observed at different energies is very similar with respect to the one found at 1 TeV for both EPICS, GEANT4 and FLUKA.

3.2.4 Benchmark summary

The discussed comparisons show a reasonable agreement among the three simulations about the energy deposited and the shower profile in TASC. As far as CHD and IMC response is concerned, a quite good agreement between FLUKA and GEANT4 is found. There are significant differences between GEANT4 and EPICS instead, more and more pronounced as the primary particle energy increases. Because of the overall agreement between FLUKA and GEANT4, and the good agreement between GEANT4 and EPICS concerning the TASC benchmarks too, the implementation of the CALETCAD geometry within the GEANT4 code is considered validated and can be used for the data analysis in parallel with EPICS and FLUKA. In §4 a precise comparison of the CALET performance for the measurement of the electron flux obtained with EPICS and GEANT4 are discussed, and a preliminary validation of these results with several

comparisons between EPICS and GEANT4 MC data and flight data is also presented in §4.8.

Chapter 4

Electron flux measurement

The measurement of the electron spectrum is the main scientific goal of the CALET mission as described in §2.3. The data analysis involved in the measurement it is the main objective of this thesis and is described in this chapter; different cuts studied to select electrons and reject the main background events are presented and a comparison of the results of these analysis techniques obtained with the EPICS and GEANT4 MC simulations is discussed too. Some results described in this chapter are also summarized in [80]. The first sections of this chapter present a brief description of the CALET acceptance (§4.1), of the MC simulations involved in the analysis (§4.2) and of the parameters used for the electron flux calculation (§4.2). The selections developed for this Ph.D. work, with the expected selection efficiencies and residual contaminations due to different backgrounds source, obtained with different MC simulations, are discussed in §4.6 and §4.7. A preliminary validation of the results obtained with the MC simulations and a preliminary evaluation of the systematic error that affect the electron measurement due to the proton rejection cut and the application of different MC simulation results are described in §4.8 and §4.9 respectively. During the drawing of this Ph.D. thesis, the CALET collaboration has finalized the analysis used for the electron measurement: this analysis exploits the selections developed during this thesis with some modifications. The last section of this chapter presents the first measurement of the CALET electron flux, pointing out the differences of the final version of the analysis with respect to the data analysis described in this thesis. An article regarding the results of the CALET electron measurement has been accepted by "Physical Review Letters" in the first days of October 2017 and it is currently in press (30 Oct. 2017) [88].

4.1 The CALET geometrical factor

For the electron spectrum analysis, four acceptance categories are defined.

- **Acceptance A** (acc. A): a particle is inside the acc. A if its direction of incidence extrapolated to the bottom of the apparatus (extrapolated track) crosses the top surface of the CHDX and CHDY, the top and the bottom of the TASC (the top of TASCX1 and the bottom of TASCY6) within an inner fiducial region 1.9 cm (i.e. one PWO log) apart from the TASC lateral borders on both sides.
- **Acceptance B** (acc. B): the extrapolated particle track crosses the top CHD layers, the top and bottom of the TASC, but it is outside the TASC fiducial volume defined for the acc. A.
- **Acceptance C** (acc. C): the extrapolated particle track crosses the IMCX5 and IMCY5, the top and bottom of the TASC, excluding particles inside acc. A and B.
- **Acceptance D** (acc. D): the extrapolated particle track crosses the IMCX5 and IMCY5, the top of the TASC, and travels for a minimum length of 26.42 cm in the TASC volume (corresponding to the vertical TASC depth, which is ~ 27 X_0), excluding particles inside acc. A, B, and C.

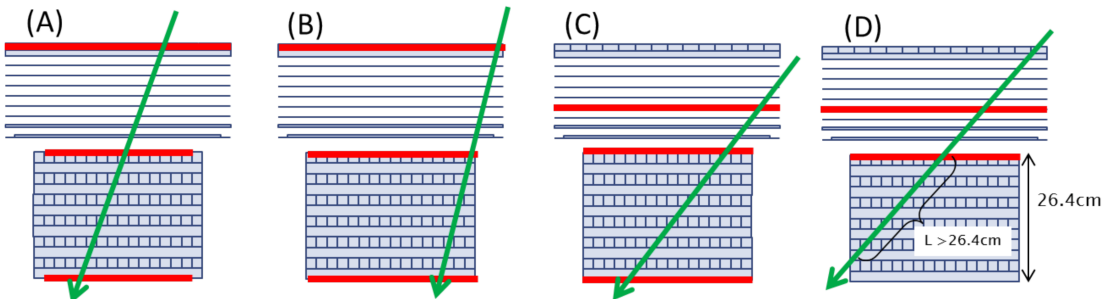

Figure 4.1. *Schematic images of the CALET acceptance categories.*

The schematic representations of the four acceptances are shown in fig. 4.1.

For a generic telescope and an isotropic flux, a geometrical factor (G) [69], usually expressed in $[cm^2 sr]$, is associated to the detector acceptance and defined as:

$$G = \int_{\Omega} d\omega \int_{S} d\vec{\sigma} \cdot \hat{r}, \tag{4.1}$$

where $d\omega$ is the element of solid angle equal to $d\phi\ dcos(\theta)$, where ϕ and θ are the azimuthal and polar angles respectively, Ω is the solid angle domain corresponding to the telescope acceptance, S is the total area of the bottom sensor of the telescope, $d\vec{\sigma}\cdot\hat{r}$ is the effective element of area looking into $d\omega$.

For the measurement of the geometrical factor of complex telescopes, the RHS of eq. 4.1 can not be integrated analytically, thus in [69] an approach based to the MC technique is proposed. This method is based on the generation of particles with random directions and starting points on a generation surface, which must be large enough to cover the complete telescope acceptance. In order to properly calculate the geometrical factor corresponding to an isotropic flux, for each event, in choosing the trajectory starting point equal areas should have equal weights, while the incident directions will be weighted by a factor $\cos\theta$, where θ is the angle of the trajectory with the normal of the generation surface. The geometrical factor G of the telescope is then given by:

$$G = \frac{N_{sel}}{N_{gen}} G_{gen},$$

where N_{gen} is the number of generated events, N_{sel} is the number of events with the generated trajectory inside the telescope acceptance and G_{gen} is the geometrical factor of the generation surface; the latter is commonly selected with a simple geometry in order to calculate G_{gen} by analytical integrating eq. 4.1.

A MC simulation based on the EPICS package [70], with the CALETCAD geometry, is used for the calculation of the CALET geometrical factor. Simulated electrons are isotropically generated in order to cover a geometric region greater than the true CALET acceptance (A+B+C+D). In the EPICS simulation, the generation surface is a hemisphere, with a radius equal to 78 cm, completely covering the top of the CALET instrument. The geometrical factor of a single surface, by solving eq. 4.1, is $G = A\pi$ [69], where A is the surface area. For the MC generation surface it results in a geometrical factor $G_{gen} = 12.01$ m^{2}sr. For this calculation the simulation of the passage of particles trough matter is not needed, since G depends only on the detector geometry for the CALET experiment. The values of the geometrical factors corresponding to the CALET acceptances are:

- acc. A (415.7 ± 1.1) cm^{2}sr,
- acc. B (154.6 ± 0.6) cm^{2}sr, (acc. A+B (570.3 ± 1.3) cm^{2}sr),
- acc. C (230.1 ± 0.8) cm^{2}sr, (acc. A+B+C (800.4 ± 1.6) cm^{2}sr),

- acc. D (236.4 ± 0.8) cm^{2}sr, (acc. A+B+C+D (1036.6 ± 1.8) cm^{2}sr).

The acc. A is designed to maximize the energy resolution by selecting electromagnetic showers that are well contained in the calorimeter and rejecting events near the calorimeter edges, though the geometrical factor is about half of the total CALET acceptance. The other three acceptance categories achieve an increasing geometrical factor, while the energy resolution gets worse. The energy resolution of CALET, for events inside the acc. A, is discussed in §4.5.

The analysis described in this chapter takes into account the acc. A., while the final result discussed in §4.10 also involves the acc. B.

4.2 Monte Carlo simulations

In this chapter, the performance of the CALET detector for the measurement of the electron flux obtained with simulations based on the EPICS and GEANT4 packages is discussed. Electrons and protons are simulated with both MC packages since the main background for the electron measurement are protons (see §4.7 for a description of the expected proton contamination in the electron flux). Simulated particles are isotropically generated in order to cover a geometric region greater than the true CALET acceptance (A+B+C+D) and to take into account possible contaminating out-of-acceptance particles, which are reconstructed inside the CALET acceptance due to the finite angular and spatial resolution of the tracking, or which are scattered inside the acceptance by interactions with the detector and its mechanical structure. The main goal of CALET is the observation of high-energy electrons in the energy range from 10 GeV to 10 TeV thus electrons are simulated in a larger energy range in order to take into account folding border effects due to the finite energy resolution of the detector. The energy range of the proton simulations need to be at least one order of magnitude greater than the one for electrons, since due to the large energy resolution of CALET for protons, the energy deposit by protons in the calorimeter can be < 10 TeV even if its kinetic energy is ~ 100 TeV. See §4.7 for a description of the kinetic energy of contaminating protons.

EPICS simulation Electrons and protons are simulated with EPICS, version 9.20, by using the hadronic interaction model DPMJET-III, in the energy range from 2 GeV

to 20 TeV; the number of total generated electrons and protons is $8 \cdot 10^7$ and $8 \cdot 10^8$ respectively. The incoming flux is generated as a single power-law spectrum with spectral index equal to -1. In order to extend the simulated proton spectrum to higher energies and avoid very long computation time, protons between 20 TeV and 1 PeV are simulated with spectral index of -2.5, the total number of generated protons in this energy range is $5.6 \cdot 10^7$. The generation surface is the same used for the measurement of the CALET geometrical factor and it is described in §4.1.

GEANT4 simulation Protons and electrons are simulated with GEANT4, version 10.01.p02 and FTFP˙BERT physics list, using a single power-law spectrum with spectral index equal to -1. Electrons are simulated from 2 GeV to 20 TeV and the total number of events is $5 \cdot 10^6$, while protons are generated from 10 GeV to 100 TeV for a total number of events of $4.4 \cdot 10^7$. The generation surface is a 240×240 cm^2 horizontal plane placed 2 cm above the CHDX top surface. These dimensions have been chosen in order for the full CALET acceptance to be populated by particles generated on the plane. In order to reduce the computation time, the simulation of the interaction of particles with CALET is performed only for a fraction of the generated events. Four loose CALET acceptance types are defined to this purpose: the acceptances described in §4.1, also implemented in the GEANT4 code, are enlarged by a factor of 20%. Only events initially generated inside the 4 loose acceptances are actually simulated. This configuration ensures a complete simulation of particles in the acceptance (A+B+C+D) and some events useful for the studies of contamination due to events out-of-acceptance.

In order to reproduce a realistic proton and electron fluxes by using the MC simulations, an event-by-event re-weighting procedure of the simulated spectrum is applied. The weight of each event (W) depends on the kinetic energy E_k and it is defined as:

$$W(E_k) = T \cdot \frac{\phi_{data}(E_k)}{\phi_{MC}(E_k)}, \tag{4.2}$$

where T is the foreseen observation time (in units of seconds) of CALET equal to 5 years, ϕ_{MC} is the simulated flux and $\phi_{data}(E_k)$ is a parametrization of the real flux. $W(E_k)$ is used as the weight of each event during the filling of all the histograms or graphs used during the analysis: this procedure allows to directly obtain the expected number of events observed by CALET in 5 years in each energy bin. The simulated

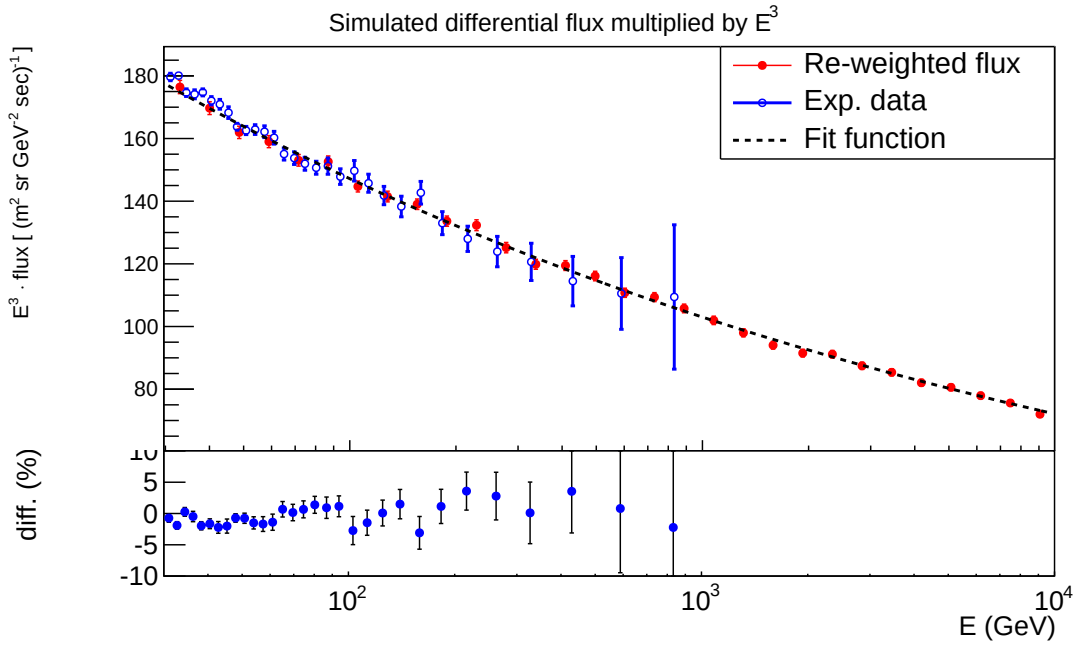

Figure 4.2. *Test of the re-weighting procedure with electrons simulated with EPICS. Top panel: simulated differential flux after the re-weighting procedure (red points) compared with the AMS-02 data (blue points) and a parametrization of this measurement as a single power-law with a spectra index equal to* -3.15 *and a normalization* ~ 300 *(black dotted line). Bottom panel: differences between the re-weighted flux and the AMS data.*

spectra for both GEANT4 and EPICS in each energy interval are single power laws and can be written as:

$$\phi_{MC}(KE) = C \cdot E_k^{\alpha},$$

where α is the spectral index and C is the normalization; the latter can be calculated by using the number of generated events N_{gen} and the total geometrical factor of the generation surface G_{gen} with the following relation:

$$C = \frac{N_{gen}}{G_{gen} \cdot \int_{E_k^{min}}^{E_k^{max}} E_k^{\alpha} dE_k}.$$

where E_k^{min} and E_k^{max} are the lower and higher limits of the simulated energy range. By employing this technique, the electron simulations are re-weighted according to a single power-law with spectral index -3.15 and a normalization factor of ~ 300: these parameters are obtained by fitting the electron flux measured by the AMS-02 experiment [41] in the 30 GeV $-$ 1 TeV energy range. A simple validation test of this procedure is shown in fig. 4.2; this figure shows a comparison between the AMS-02 electron data and the differential electron flux obtained with the re-weighting proce-

dure of the EPICS electron simulation, which is computed by counting the number of events with the initial trajectory inside the acc. A in each kinetic energy bin divided by the foreseen observation time and the geometrical factor of the acc. A. Since the re-weighted flux is consistent with the AMS-02 flux used for computing the re-weight parameters, the procedure is considered as validated. The same result is obtained by employing the simulated electrons with GEANT4.

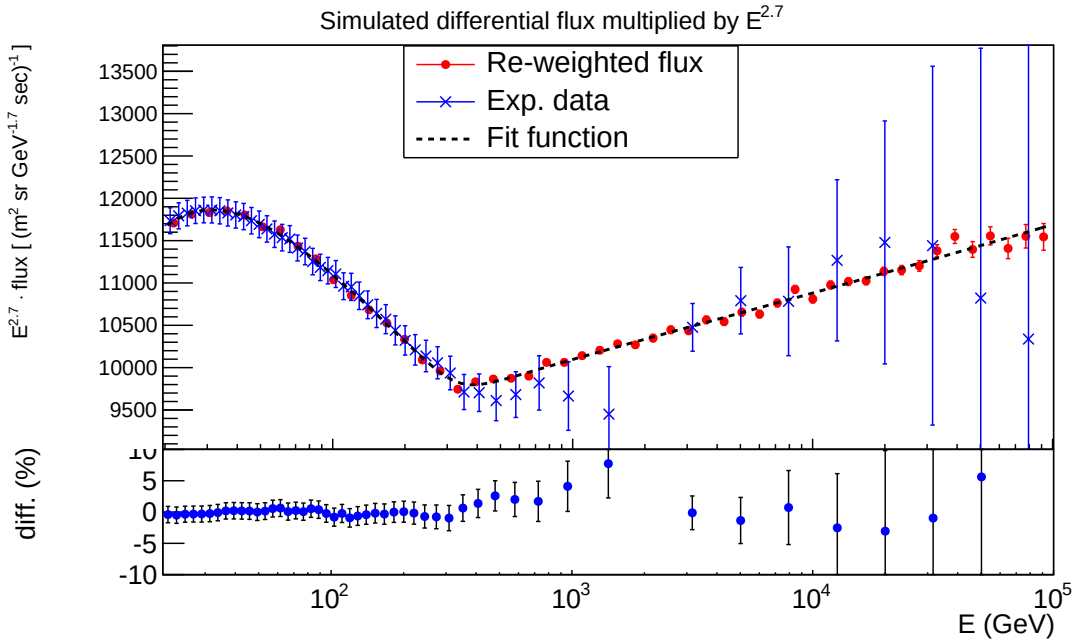

Figure 4.3. *Test of the re-weighting procedure with protons simulated with EPICS. Top panel: EPICS flux after the re-weighting procedure (red points) compared with the AMS-02 data [41] (blue cross below* 2 TeV*) and CREAM-I data (blue cross above* 10 TeV*) and a parametrization of this measurement with eq. 4.3 (black dotted line). Lower panel: differences between the re-weighted flux and the experimental data.*

The proton simulations are weighted according the combined data of AMS [37] and CREAM-I [34], by using the following approximation of the proton flux:

$$\phi_p(E_k) = (1 - \frac{p_0}{E_k} - \frac{p_1}{E_k^2}) \cdot \phi_{AMS}(E_k), \tag{4.3}$$

where p_0 and p_1 are two phenomenological parameters, and $\phi_{AMS}(E_k)$ is the parametrization of the AMS-02 measurement of the proton flux discussed in §1.5.1):

$$\phi_{AMS}(E_k) = C \left(\frac{E_k}{45 \text{ GeV}} \right)^{\gamma} \left[1 + \left(\frac{E_k}{330 \text{ GeV}} \right)^{\Delta\gamma/s} \right]^{s}.$$

The parameters used here for the fit of the AMS-02 and CREAM-I data are: $C = 0.441$, $\gamma = -2.83$, $\Delta\gamma = 0.166$, $s = 0.02$, $p_0 = 3.89$ and $p_1 = -2.97$. Fig. 4.3 show the comparison between the re-weighted flux and the data from AMS-02 and CREAM-I.

Simulation digitization In order to reproduce the real detector performance, the native output of the MC simulations is convolved with instrumental features like electronic noise etc., in a process called digitization. The digitization implemented in CALET is based on the results of the in-flight calibration of the detector described in details in [31], and it takes into account two main effects briefly described below.

Electronic noise. As a first approximation, this introduces a smearing of the energy deposit that does not depend on the energy itself. The amount of the electronic noise can be estimated by using pedestal events acquired during the flight, i.e. events acquired with a random trigger without signals induced by incoming particles. For each channel, the distributions of pedestals are well fitted by a Gaussian distribution. The digitization procedure introduces a smearing to the energy deposit as computed by the simulations according to the Gaussian distributions fitted during the pedestal analysis. This smearing has a considerable impact on the small TASC signals read-out by APDs, since the signal/noise ratio, here defined as the ratio of the ADC channel corresponding to an energy deposit of 1 MIP and the sigma of the pedestal distribution, is about 1, while for the first layer of TASC (which is read by PMTs), and a typical channel of CHD and IMC, has a small impact since the signal/noise ration is ≥ 10. A TASC channel read-out by PD is taken into account only when the signal of the corresponding APD channel is saturated; the saturation of the APD coincides with a typical signal in PD much larger than the PD electronic noise thus this smearing term is negligible for the TASC channels read-out by PDs too.

Scintillation photo-statistic The light emitted by a scintillating detector is proportional to energy deposit in the detector itself. An intrinsic fluctuation of the emitted light corresponding to a constant energy deposit is present; as a first approximation the number of photons emitted during the scintillation follows a Poisson distribution, thus the sigma of the distribution is $\sigma = \sqrt{< N >}$ where $< N >$ is the mean number of photons. Furthermore, the signal fluctuations in real detector are also influenced by other instrumental features, e.g. the light collection and the quantum efficiency of

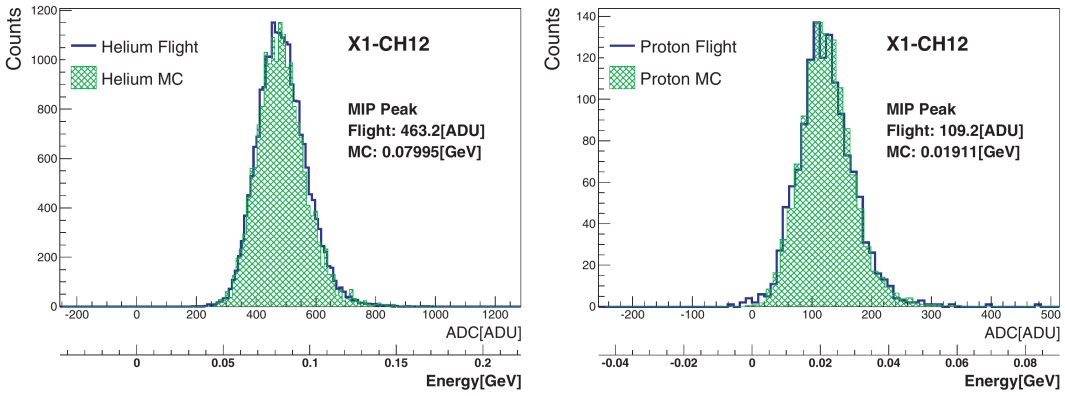

Figure 4.4. *Comparison of the energy deposit by non-interacting helium nuclei (left panel) and protons (right panel) obtained with the flight data (blue histogram) and the digitized EPICS data (green filled histogram).*

the light detector; these reduce the number of photons converted to electric signals by the light detector itself. The parametrization of the signal smearing due to the limited photo-statistic is not trivial. For each CALET channel, by using the fight data acquired with the Single Trigger configuration (see 2.2) and selecting non-interacting protons and helium nuclei, the distributions of the energy deposit are compared with the one obtained from the EPICS simulation, after the application of the smearing due to the electronic noise. The residual discrepancies between the simulated and the flight data are mainly due to the photo-statistics: for a given energy deposit E_0, e.g. the energy deposit by non-interacting helium nuclei, these discrepancies are removed by applying a further Gaussian smearing with a standard deviation parameter equal to σ_0, properly selected to match the flight data distribution. Then the sigma parameter σ used for the smearing for a different energy deposit E as a first approximation is $\sigma = \sigma_0\sqrt{\frac{E}{E_0}}$ since the energy deposit is proportional to the number photons (N) detected by the light detector and for a large count of photons the Poisson distribution is well approximated with the Gaussian distribution.

By taking into account the two described effects, the energy deposit after the digitization procedure (E_{DG}) is described by the following equation:

$$E_{DG} = E_{MC} + G(K_{ADC-GeV} \cdot \sigma_{ped}) + G(\sigma_0\sqrt{\frac{E_{MC}}{E_0}})$$

where E_{MC} is the energy deposit computed by the MC simulations, $K_{ADC-GeV}$ is the conversion factor between the ADC channel and the GeV units found during the

CALET calibration [31], $G(X)$ represent the Gaussian smearing with a sigma parameter equal to X, σ_{ped} is the sigma parameter of the fit of the pedestal distribution expressed in ADC units, σ_0 is the sigma parameter of the Gaussian smearing related to the photo-statistic at energy E_0. A comparison between the simulated data with EPICS after the digitization procedure and the flight data for non-interacting protons and helium nuclei is shown in fig. 4.4: a good agreement is featured.

Besides the application of the digitization procedure, in order to improve the agreement between MC simulations and the flight data about the variables related to the shower development in TASC, all the logs with a signal less than 3 MIP are not taken into account during this analysis; see §4.8 for a comparison between the simulation data and the flight data.

From February 2016 to September 2016, 3 APD channels have shown anomalous behaviours since, in some time periods, the noise of these channels has become about 3 orders of magnitude greater than those of the other APD channels. The normal operation of these channels has been recovered in September 2016 with a modification of the high voltage power supply. Such an anomalous situation required a time dependent digitization of the MC simulation, in order to correctly simulate different time periods with different detector status. This procedure is actually under study but at this stage is not available, thus for this work, a more simple approach is used: the signals of these noisy channels (hereafter indicated with "dead channels") is replaced with 0 for both flight data (all the data, without selection on the time period) and the MC simulation data. As discuss in the following sections, the performance of the detector remains sufficient for the physical goals of CALET even with 3 dead channels.

4.3 Differential flux measurement.

In this Ph.D. thesis the word "spectrum" indicates the differential flux $\phi(E)$ defined as the number of events dN per unit area normal $dS_\perp$, time dt, solid angle $d\Omega$ and energy dE:

$$\phi(E) = \frac{dN}{dE \cdot dS_\perp \cdot dt \cdot d\Omega} \tag{4.4}$$

The measurement of the particle fluxes with CALET involves the following parameters: the number of detected particles $N(E)$ in a given energy bin, the efficiency of the

event selection $\epsilon_{tot}(E)$, the geometrical factor G (defined in §4.1), the live time of the measurement Δt, the energy bin width ΔE and a contamination factor $N_{BG}(E)$ according to the following equation:

$$< \phi(E) >= \frac{N(E) - N_{BG}(E)}{\Delta E \cdot G \cdot \Delta t \cdot \epsilon_{tot}(E)} \tag{4.5}$$

where $< \phi(E) >$ is the mean flux in the energy bin $[E,E + \Delta E]$ and the energy scale (E) of the measurement is the best estimator of the kinetic energy of particles. In this chapter the symbols E_{dep}, E_{true} and E indicate the energy deposit in the CALET detector, the true kinetic energy of incoming particles and the reconstructed kinetic energy with the CALET instruments respectively, see §4.5 for a precise description of the reconstructed energy for electrons. In the electron spectrum analysis G and Δt do not depend on the particle energy while $\epsilon_{tot}(E)$ and $N_{BG}(E)$ depend on the particle energy, charge, type (e.g electrons or nuclei). Each term of eq. 4.5 is discussed in this chapter.

4.4 Live time measurement

The *"live time"* (LT) of a measurement is the amount of time for which the detector is capable to acquire new data. In a typical experiment, after a trigger signal, the apparatus spends an amount of time, named *"dead time"*, to process the electronic signals and store the resulting data. During this time period the apparatus is not able to accept new triggers. As an example, consider two consecutive events: the amount of live time LT_{ev} that elapses between the two events is given by:

$$LT_{ev} = \Delta t - DT_{ev}$$

where Δt is the absolute time interval between the two events and DT_{ev} is the dead time associated to the data acquisition of the first event. In general the cumulative live time LT_{tot} corresponding to an observation time interval Δt can be calculated by:

$$LT_{tot} = \Delta t - \sum_{i=1}^{N} DT_i \tag{4.6}$$

where DT_i is the dead time of the i-th event, and N is the number of events acquired during the time interval Δt.

Because of the CALET electronics configuration, the information of the dead time associated to each event is not available but for each second a value of the cumulative dead time is stored. Consider a time interval of $\Delta t_{1s} \sim 1$ s starting at the absolute time t_0 with a cumulative dead time equal to DT_{1s}: to each event acquired during this time interval is associated an approximated dead time $< DT_{ev} >$ given by:

$$< DT_{ev} >= \frac{DT_{1s}}{N_{1s}} \cdot \frac{\Delta t_{1s}}{\Delta t_{ev}}$$

where N_{1s} is the number of events acquired during the considered time interval and Δt_{ev} is the time interval between the current event and the previous one. If the current event is the first event acquired during Δt_{1s}, the time interval Δt_{ev} is the difference of the absolute time of this event and t_0. The values of $< DT_{ev} >$ of each event are then used to compute the LT_{tot} of contiguous time interval using eq. 4.6. For each contiguous time intervals, an upper limit of the error due to the described procedure of the calculation of the live time is 1 s[1], thus this source of error is sizeable for short time interval, but it becomes negligible when the LT_{tot} is calculated for long contiguous time interval. The time intervals included in the high-energy electron measurement are long, typically more than 10 minutes, and the mean fraction of dead time for these events is $\sim 20\%$, thus the error related to the LT_{tot} computation does not affect the electron measurement.

4.5 Energy reconstruction for electrons

According to the EPICS and GEANT4 simulations, the energy resolution achieved by simply using the energy deposit in TASC as an estimator of the true energy of electrons above 100 GeV is better than 2%. In this thesis the energy resolution is computed by intersecting the energy distribution with a horizontal line, at a height such that the intersections define an energy interval containing 68.3% of the events; the half-width of this interval divided by the most probable value (MPV) of the energy distribution is the energy resolution. The mean of the energy deposit in TASC by electrons with true kinetic energy equal to 1 TeV is about 0.95 TeV; this means that in order to

[1]The error of the LT_{tot} of a contiguous time interval is due to the error of the approximation of the dead time of the first and last events of the time interval itself, which can not be greater than 0.5 s for each of the two events. The errors related to the other events are removed by the sum of $< DT_{ev} >$ used for the calculation of LT_{tot}, eq. 4.6.

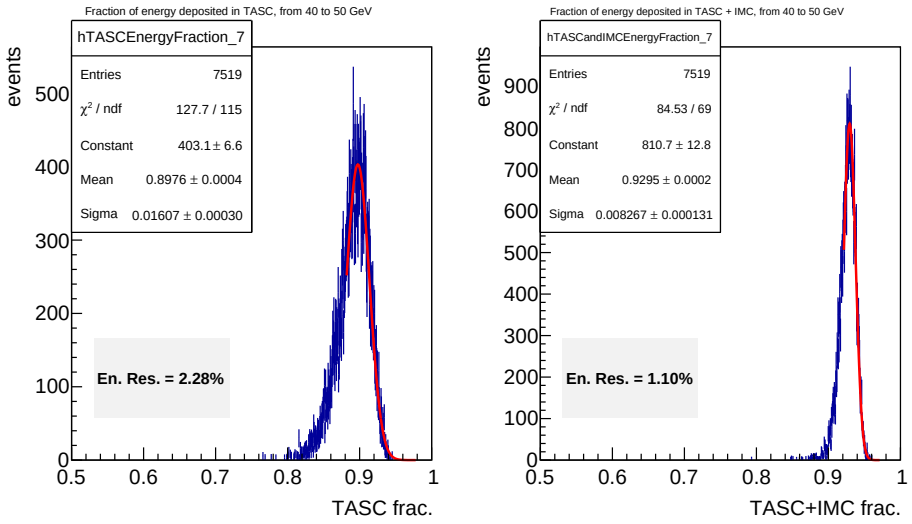

Figure 4.5. *EDF in TASC (left panel) and in TASC + IMC (right panel) for electrons in the energy deposit bin* $[40, 50]$ GeV *obtained with the EPICS simulation. The red line is a Gaussian fit of the peak and the right side of the distribution.*

correctly estimate the true electron energy a correction factor of the energy deposit in TASC is needed, which for electrons at 1 TeV is about $\sim 5\%$. Furthermore, for electrons below 100 GeV the energy deposit in the IMC, especially in the SciFis and tungsten layers, is not negligible. Since the tungsten is a passive material, in order to retrieve the energy deposit in tungsten layers a simple procedure based on the EPICS electron simulation is adopted: for each SciFi+W layer the mean fraction of energy deposit in W is computed using MC data. These mean fractions are used as calibration parameters to compute the total energy deposit in the tungsten layers E_W with the following formula:

$$E_W = \sum_{i=0}^{8} C_i E_i^{IMC}$$

where E_i^{IMC} is the energy deposit in the SciFis of the i-th layers and C_i is the calibration parameter of the i-th tungsten layer (which is as a first approximation energy independent): from the top to the bottom the values of C_i are: 3.96, 4.12, 4.29, 4.47, 4.54, 18.1 and 22.5. The sum of the energy deposit in SciFis and tungsten layers calculated with this procedure is hereafter indicated with "energy deposit in IMC". Fig. 4.5 shows a comparison between the *"Energy Deposit Fraction"* (EDF) in TASC (left panel), defined as the energy deposit in TASC divided by the true kinetic energy, and the EDF in TASC summed with EDF in IMC (hereafter "EDF in TASC+IMC") for electrons at ~ 45 GeV simulated with EPICS. By taking into account the energy de-

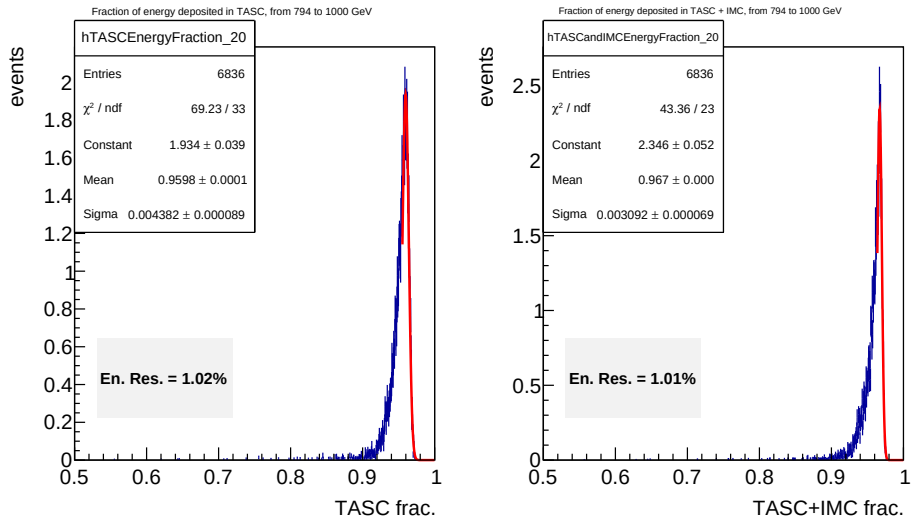

Figure 4.6. *EDF in TASC (left panel) and in TASC + IMC (right panel) for electrons in the energy deposit bin* $[794, 1000]$ GeV *obtained with the EPICS simulation. The red line is a Gaussian fit of the peak and the right side of the distribution.*

posit in TASC+IMC the energy resolution improves with respect to the energy deposit in TASC only. In fig. 4.6 the same comparison for electrons above ~ 790 GeV is shown: here the energy deposit in IMC has not impact in the energy resolution. The red line in the figures is a Gaussian fit of the peak of the distribution used for the identification of the MPV.

By using the energy deposit in TASC+IMC, an estimator of the true kinetic energy of electrons can be found dividing the energy deposit in TASC+IMC by the mean of the EDF in TASC+IMC, which depends on the energy deposit itself. In the left panels of fig. 4.7 the trend of this parameter with energy is shown for both the TASC only and the TASC+IMC cases. The plots are fitted by the following empirical equation:

$$F(E_{dep}) = p_0 + \frac{p_1}{\sqrt{E_{dep}}} + \frac{p_2}{E_{dep}} + p_3\sqrt{E_{dep}}, \tag{4.7}$$

where E_{dep} is the energy deposit in TASC (TASC+IMC), p_0, p_1, p_2 and p_3 are the fit parameters; the values of those are shown in fig. 4.7. In the right panels of fig. 4.7 the energy resolution is shown: the TASC+IMC case achieves a better resolution in the low-energy region ($E_{dep} < 100$ GeV) while in the high-energy region there is not an appreciable difference. The trend of the resolution of a typical calorimeter [83] is related to the shower intrinsic fluctuations, to the electronic noise and to non-uniformities of

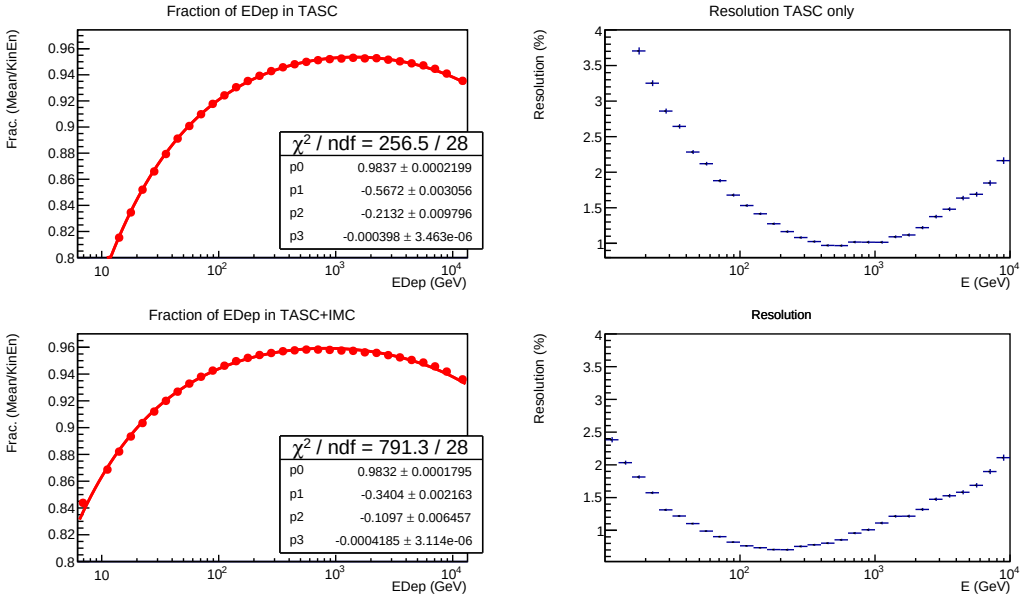

Figure 4.7. *Some results of the EPICS simulation concerning the energy reconstruction in CALET. Left panels show the mean of the EDF in TASC (top left panel) and in TASC+IMC (bottom left panel) as a function of the energy deposit in TASC and TASC+IMC respectively; the red line is the fit with equation 4.7. Right panels show the energy resolution achieved with energy deposit in TASC (top right panel) and in TASC+IMC (bottom right panel).*

the calorimeter response. In addition to those, to correctly understand the trend of the energy resolution and the EDF in CALET other two effects are relevant.

CHD and IMC passive materials. The energy deposit in the CHD and in the passive materials of the IMC (carbon fibre and aluminium honeycomb) is relevant for electrons below 100 GeV. Indeed, the EDF in active materials and tungsten decreases with a decreasing energy thus the energy resolution degrades. The depth of the maximum energy deposit of an electromagnetic shower (t_{max}, expressed in units of X_0) in a homogeneous material can be approximated with:

$$t_{max} = ln\left(\frac{E}{E_c}\right) - 0.5 \ ,$$

where E is the energy of the particle and E_c is the critical energy of the material [83]. The maximum of the shower is progressively deeper for an increasing energy thus the impact of the energy deposit in the passive materials of the IMC becomes negligible above 100 GeV.

Longitudinal leakage. Above 500 GeV the longitudinal leakage due to the shower particles escaping from the bottom of the TASC increases, thus the EDF decreases and the energy resolution gets worse with increasing energy, as shown in fig. 4.7. The lateral leakage has only a small impact in CALET for electrons inside the acc. A.

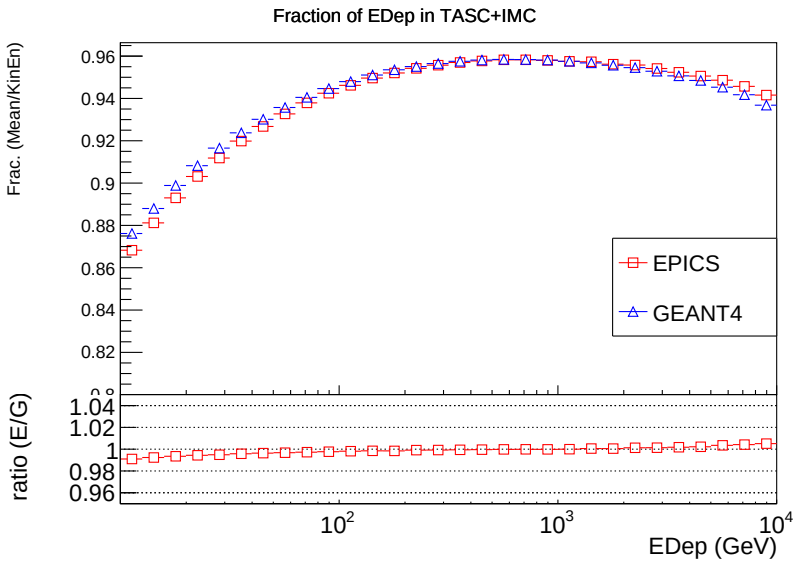

Figure 4.8. *Mean of the EDF in TASC+IMC as a function of the energy deposit TASC+IMC with the EPICS (red squares) and GEANT4 (blue triangles) simulations; the small bottom panel show the ratio between EPICS and GEANT4.*

Though these two effects are present and no dedicated correction are developed during this thesis, the energy resolution obtained with the MC simulation is sufficient for the CALET measurement, as discussed at the end of this section.

The results of the analysis with the EPICS simulation are in good agreement with the ones obtained with GEANT4. As an example, in fig. 4.8 a comparison of the EDF in TASC+IMC is shown. The GEANT4 result is slightly higher than the EPICS one below 1 TeV while it is lower at 10 TeV but the maximum difference remains reasonably small, of about 1%, as shown in the bottom panel of fig. 4.8.

The estimator (E_{rec}) of the kinetic energy (E_{true}) of the electrons, computed from the energy deposit in TASC+IMC (E_{dep}) is:

$$E_{rec} = \frac{E_{dep}}{F(E_{dep})}$$

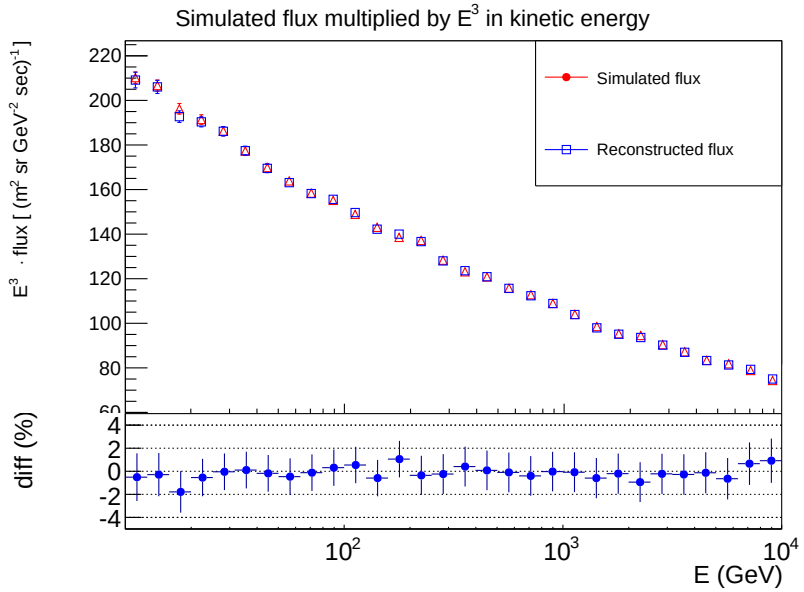

Figure 4.9. *Comparison between the simulated flux (red triangles) in kinetic energy and the reconstructed flux (blue squares) by using the energy estimator explained in the text.*

where $F(E_{dep})$ is given by the fit of eq. 4.7 to MC data. This approach is validated by using the MC simulation: the flux computed with the simulated electrons inside the acc. A and binned in E_{true}, here indicated with "simulated flux", is compared with the flux computed with the same events but using E_{rec} as the energy scale, here indicated as "reconstructed flux". This test with the EPICS simulation is shown in fig. 4.9: the agreement between the simulated and the reconstructed flux is very good, with differences below 2%. This result, also confirmed with the GEANT4 simulation, suggests that this simple procedure can be used for measuring the electron energy and that no additional unfolding procedure is needed for the electron flux measurement. Hereafter "E" indicates the reconstructed energy obtained with this method, which is used as the energy scale for the analysis described in the next sections.

4.6 Pre-selection cuts

In this section some event selection cuts used for the measurement of the electron spectrum are discussed, while the rejection cuts dedicated to the electron/proton discrimination are discussed in §4.7. This selection, here after indicated as "pre-selection", is needed in order to take into account the detector trigger and avoid contamination from events outside the acceptance and $Z >= 2$ nuclei.

4.6.1 High energy software trigger

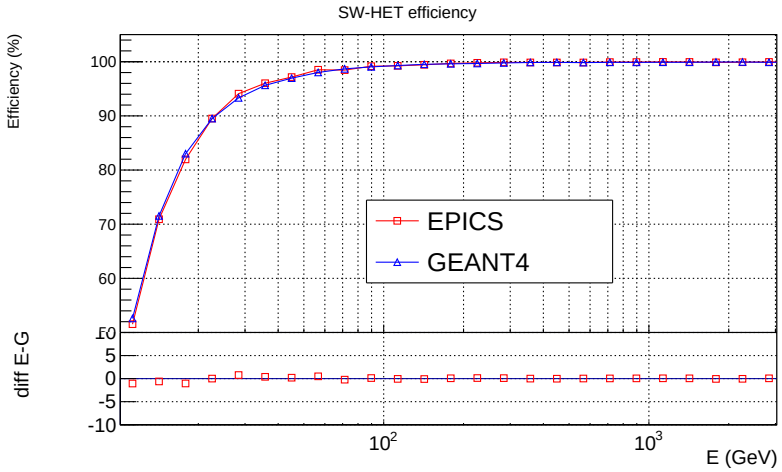

Figure 4.10. *Comparison of the efficiencies of the SW-HET cut as a function of the reconstructed kinetic energy of electrons obtained with the EPICS (red squares) and GEANT4 (blue triangles) MC simulations. The small bottom panel shows the absolute difference between the EPICS and GEANT4 results.*

This event selection is already described in §3.2 since it is used for the comparison between EPICS, GEANT4 and FLUKA MC simulations. This cut, named software HET (SW-HET) is designed to be a slightly stronger cut with respect to the real HET of CALET (described in §2.2). By using flight data events acquired with the LET, and using the information about the status of each threshold discriminator, available in the CALET data format, it is possible to precisely measure the minimum energy deposit required for satisfy the HET in each channel involved in the trigger. The channels involved in the SW-HET are the same of those in the hardware HET but the thresholds are slightly higher with respect to the one measured with the flight data, in order to avoid the need for an accurate simulation of the smearing of the real thresholds that are affected by the electronic noise, temperature dependence of the threshold discriminators, etc. The thresholds applied in the SW-HET are 100 MIP for the TASC trigger signal and 40 MIP for the IMC trigger signals (the hardware thresholds for TASC and IMC signals are about 90 MIP and 30 MIP respectively).
The efficiency of the SW-HET is very similar to the efficiency of the nominal HET, with differences of only few percent for electrons above 50 GeV. The efficiency of the SW-HET for electrons with a kinetic energy from 10 GeV to 3 TeV, obtained with

the EPICS and GEANT4 simulations, is shown in fig. 4.10. The error bars are not visible in this plot because these are smaller than the markers. In this thesis the error of all the efficiencies are estimated with the frequentist Clopper-Pearson interval [84] with a confidence level of 68.3%. This approach is commonly used for the calculation of the errors on efficiencies [1]. This cut have a very high efficiency above 40 GeV ($> 95\%$) which decreases at lower energies, since the HET has been designed for the selection of high-energy electromagnetic shower. The agreement between EPICS and GEANT4 is very good, with absolute differences below 1% in the entire energy range. The differences in the selection efficiencies between EPICS and GEANT4 are treated as systematic errors of the electron flux measurement and are discussed in §4.9.

4.6.2 Tracking with a Kalman filter based algorithm

In CALET an accurate particle tracking is necessary to:

- compute the acceptance type of incoming particles,
- identify the crossed CHD paddles and IMC fibres in order to measure the particle charge and the point where it starts showering (as described in [66]),
- compute topological calorimetric variables, like the width of the shower with respect to the particle trajectory, which are used for proton rejection in electron analysis (see §4.7).

Different tracking methods have been studied by the CALET collaboration; in this thesis the algorithm based on the combinatorial Kalman filter [81] is used. This exploits the fine granularity and imaging capability of the IMC: it is a hybrid technique of data analysis for simultaneous track and vertex fitting widely used in high-energy experiments at the accelerators that can handle a high multiplicity of hits, as expected in the IMC for high-energy shower events, and reconstruct multiple track candidates. The implementation of this technique within the CALET analysis software is described in details in [82] and in [66]. Here a simplified description of the algorithm is presented. The track reconstruction can be decomposed in two independent two-dimensional problems in the XZ and YZ views. Straight lines in orthogonal planes crossing the IMC layers at various positions represent the projection of the particle trajectory on one of the two planes (XZ or YZ). In each IMC layer, nearby SciFis with an energy deposit greater than 0.4 MIP are clustered and the Centre-Of-Gravities (COG) of each cluster

is taken as a candidate track point. Track finding begins from the top of the IMC. A vertical candidate track is created for each cluster of the first five IMC layers with a very large error associated to the angle of the track. Consider a vertical tack associated to a cluster in the layer k: for each cluster in the layer $k+1$ a new track is created and it is fitted to a straight line using the points in layer k and $k+1$. Then both the vertical tracks (with only 1 point) and the fitted tracks (with 2 points) are evolved separately on the next layer $(k+2)$. For each track, the predicted impact point on the layer $k+2$ is used to identify the cluster to be assigned to the track at layer $k+2$, which lies within the position error computed for the predicted impact point itself: if 2 more more candidate clusters are present, a new track for each candidate cluster is created. Since the predicted points of the vertical track (tracks with only 1 point) have very large errors, each cluster of the $k+2$ layer leads to the creation of new tracks. All the new tracks (with 2 or 3 points) are fitted to a straight line. This procedure is then applied to the layer $k+3$, where both the initial vertical tracks coming from layer k and the fitted tracks from layer $k+1$ and $k+2$ are taken into account.
Obviously such a combinatorial algorithm can produce a very large number of track candidates thus a candidate track is discarded if, at any point of its evolution, it has a reduced χ^2 greater than 10 or a too large number of missing points (¿2); the number of missing points is the number of IMC layers without points associated to the track within the topmost and nethermost track point.
Among all the tracks found by the combinatorial Kalman filter algorithm, a group of tracks passing closer to the core of the shower reconstructed in TASC is selected, and the one with lowest χ^2 is chosen as the primary particle track.
In order to reduce the processing time, for events that triggered the HET, only IMC clusters within a *"Region Of Interest"* (ROI) are fed into the algorithm. The ROI include all the SciFi's within ± 5 cm from the intercept of the ROI axis with each IMC layer. The ROI axis is the shower axis found by reconstructing the shower in TASC and in the last layers of the IMC. A precise description of the ROI definition is described in [82].

Such a procedure can also give no good candidate for the primary track, e.g. when all the candidate tracks are discarded due to the reduced χ^2 and missing points criteria. The efficiency of this algorithm is defined as the number of events with a primary track reconstructed divided by the total number events. This efficiency, calculated on those events that trigger the SW-HET, and obtained with both EPICS and GEANT4

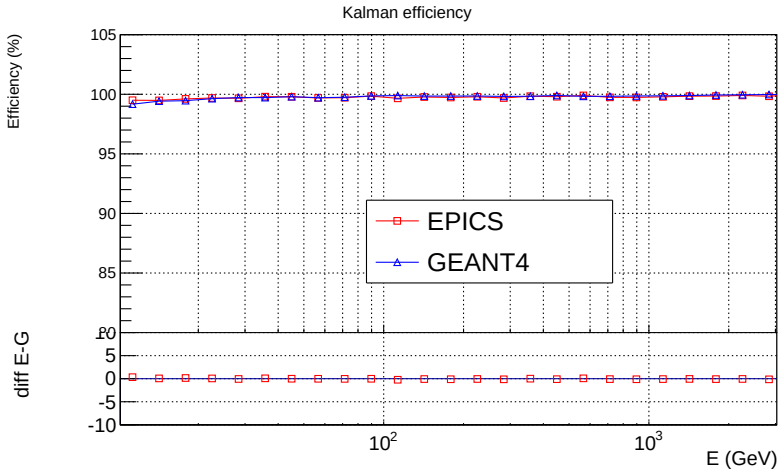

Figure 4.11. *Comparison of the efficiencies of the tracking algorithm as a function of the reconstructed kinetic energy of electrons obtained with the EPICS (red squares) and GEANT4 (blue triangles) MC simulations. The small bottom panel shows the absolute difference between the EPICS and GEANT4 results.*

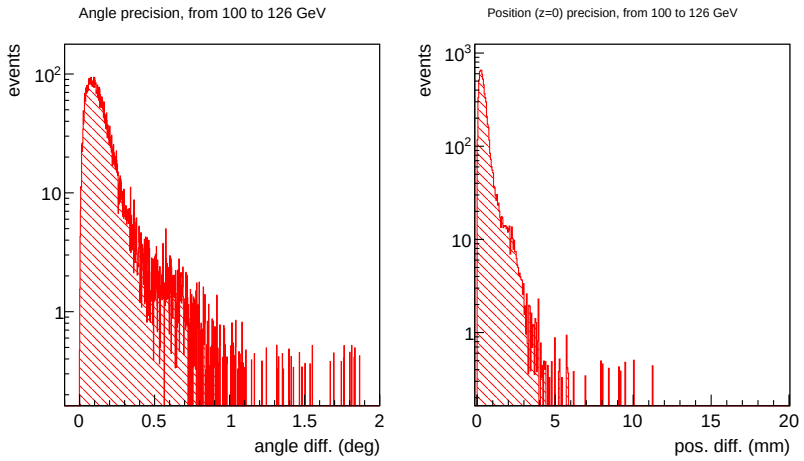

Figure 4.12. *Check of the tracking algorithm accuracy for electrons with a reconstructed kinetic energy in the energy bin* $[100, 126]$ GeV *and inside the acc. A. Left panel: angle between the reconstructed and the MC track. Right panel: distance between the intersections of the reconstructed and the true MC track with the top of the CHD.*

simulations, is shown in fig. 4.11 and is about 99% in the whole energy range.

In parallel with the efficiency is important to check the accuracy of the tracking algorithm. Two simple estimators of the accuracy are defined: the angle between the reconstructed track and the true particle direction generated by the MC (in this section named "angular precision") and the distance between the intersections of the reconstructed and the true MC track with the top of the CHD (placed at $Z = 0$)

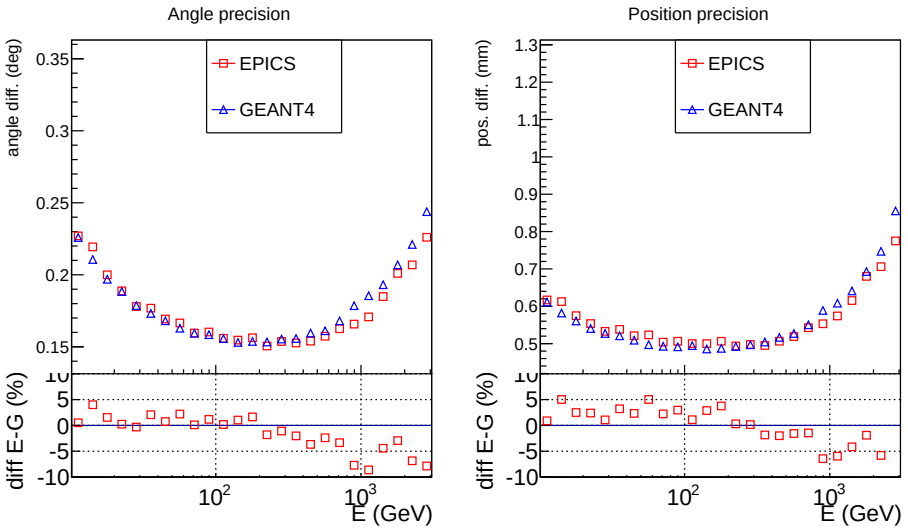

Figure 4.13. *Accuracy of the tracking algorithm obtained with EPICS (red squares) and GEANT4 (blue triangles) MC simulations for electrons with a reconstructed energy from* 10 GeV *to* 3 TeV*. Left panel: angular precision. Right panel: position precision.*

(named "position precision"). Fig. 4.12 shows these estimators for electrons with the reconstructed tack inside the acc. A and the reconstructed kinetic energy in the energy bin $[100, 126]$ GeV, simulated with GEANT4. The angular precision is better than 1° and the position precision is better than 5 mm for almost all the events ($> 99\%$). To evaluate the tracking accuracy as a function of the energy, in each energy bin, the value of the estimator X_E (where X_E is either the angular precision or the position precision) containing the 68.3% of the events in the range $0 < X < X_E$ is found. The trend of the angular precision and the position precision with energy for electrons is shown in fig. 4.13. The trend of the tracking precision, which shows a minimum around 200 GeV, is mainly due to two effects:

- below 50 GeV the most of the shower is contained in the top section of the TASC, and only the first 4 layers have a considerable energy deposit, so it is difficult to estimate an accurate ROI,

- above 500 GeV the number of backscattered particles increases and the number of mis-reconstructed tracks due to the backscattering increases too.

Furthermore, some discrepancies between the simulations are present. The differences are less than 10% and these are partially expected since the performance of the tracking is affected by the backscattered particles, and a different treatment of backscattering due to the shower develop in TASC is found in the simulations, as discussed

in §3.2. The impact of backscattered particles on the IMC energy deposit is greater in GEANT4 with respect to EPICS, thus the accuracy of the tracking obtained with EPICS is slightly better than the one obtained with GEANT4 in the high-energy region.

4.6.3 Reconstructed acc. A

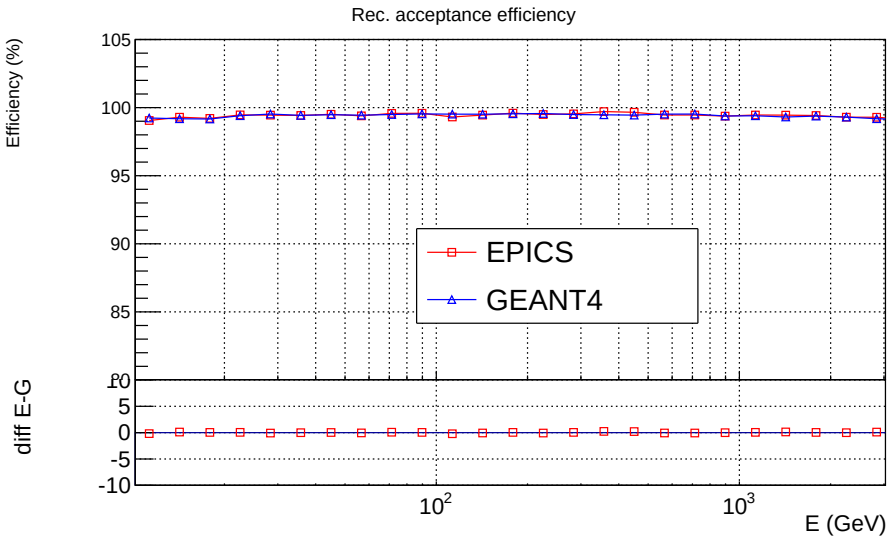

Figure 4.14. *Comparison of the efficiencies of the selection of reconstructed acc. A as a function of the reconstructed kinetic energy of electrons obtained with the EPICS (red squares) and GEANT4 (blue triangles) MC simulations. The small bottom panel shows the absolute difference between the EPICS and GEANT4 results.*

By using the track reconstructed with the Kalman filter algorithm, only events inside the acc. A are selected. Fig. 4.14 shows the efficiency of this selection, defined as the number of selected events divided by the number of events with the true direction inside the acc. A, taking into account only events with a good reconstructed track. The efficiency is greater than 98% in the whole energy range.

The acceptance contamination, defined as the number of events with the reconstructed track inside acc. A but the true trajectory outside the acc. A divided by the total number of events with the reconstructed track inside acc. A, as a function of energy for electrons obtained with the EPICS simulation is shown in fig. 4.15. This contamination is quite large especially in the high-energy range and it is due to two different categories of events. The first category consists of events with true trajectory near to the acc. A, e.g events with the generated track inside acc. B or C, reconstructed

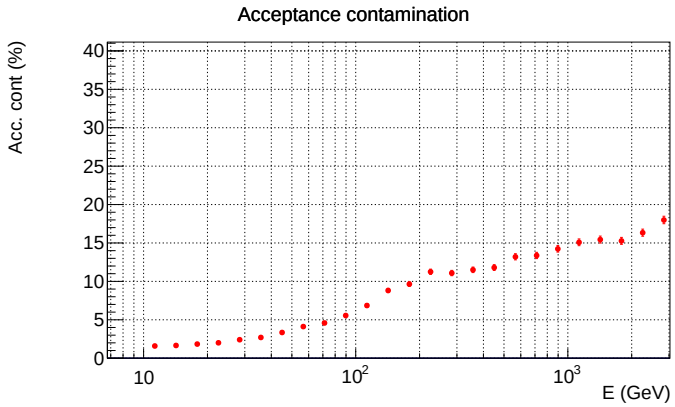

Figure 4.15. *Acceptance contamination for electrons as a function of the reconstructed kinetic energy obtained with the EPICS simulation.*

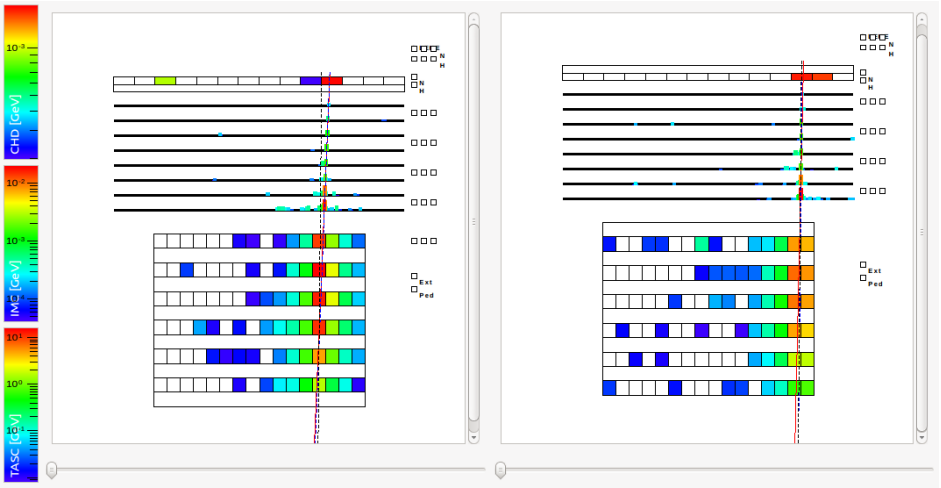

Figure 4.16. *Display of a contaminating event coming from acc. B, simulated with EPICS. The left panel shows the X view of the CALET detector while the right panel shows the Y view. The blue dotted line is the true particle direction, the red line is the reconstructed track and the black dotted line the reconstructed shower axis in TASC.*

inside the acc. A due to the finite resolution of the tracking algorithm; an example of one contaminating event of this category is shown in fig. 4.16. This event is out of acc. A since its true direction is outside the TASC fiducial area defined inside the acc. A: in the image it is difficult to appreciate the difference between the true and the reconstructed track but the Y view shows that the true direction intersects the edge of the last log of the first TASC layer. The second category consists of events with very inclined true trajectories that interact with the TASC or with the passive materials surrounding the calorimeter. The definition of the ROI is complicated for this kind of events since the algorithm for the reconstruction of the shower axis is mainly studied for particles coming from the top of the calorimeter and it is currently not optimized

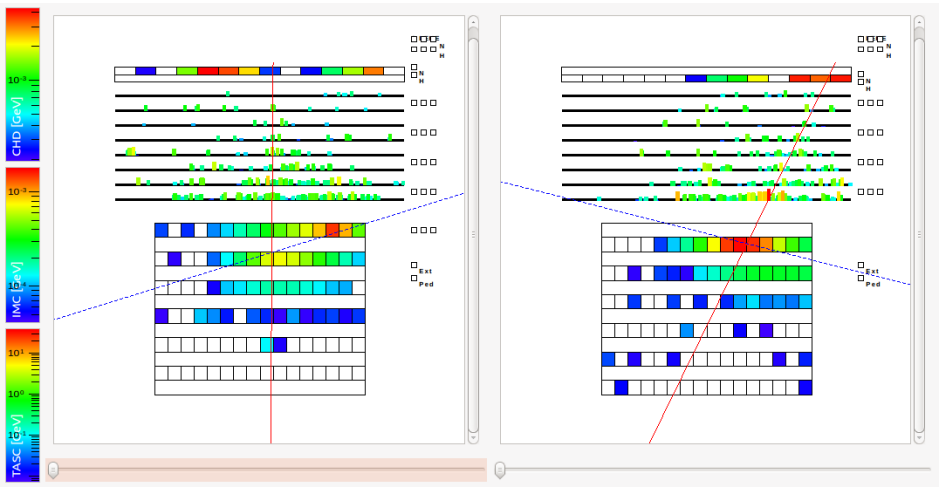

Figure 4.17. *Display of a contaminating event coming from out of acc. A+B+C+D, simulated with EPICS. The left panel shows the X view of the CALET detector while the right panel shows the Y view. The blue dotted line is the true particle direction, the red line is the reconstructed track and the shower axis is not present.*

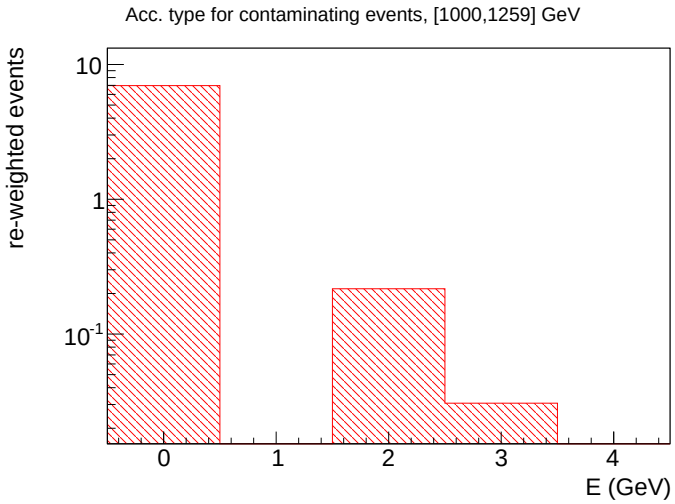

Figure 4.18. *True acceptance of contaminating electrons in the bin* $[1000, 1259]$ GeV. *X axis indicates the true acceptance: 0 indicates events out of acceptance A+B+C+D, 2 indicates events inside acc. B, 3 indicates events inside acc. C, 4 indicates events inside acc. D.*

for these events. An example is shown in fig. 4.17, for this event the shower axis is not found and the reconstructed track is almost vertical.

Fig. 4.18 shows the true acceptance of contaminating electrons at $\sim$ 1 TeV. The bulk of contaminating events ($>$ 95%) consists of particles out of acceptance (A+B+C+D) included in the second category of contaminating events. The number

of contaminating events which belong to the second category strongly depends on the electron kinetic energy, and the impact of this contamination increases with energy, while the contamination from events of the first category weakly depends on the energy, thus it is relevant only for electrons below 50 GeV. To reject contaminating out-of-acceptance events different techniques are under study, e.g. a three-dimensional shower reconstruction to identify the shower axis for particles coming from the lateral faces of TASC and IMC; in this work two specific cuts described in the next paragraph are employed to reduce this contamination.

4.6.4 IMC shower concentration and TASC consistency cuts

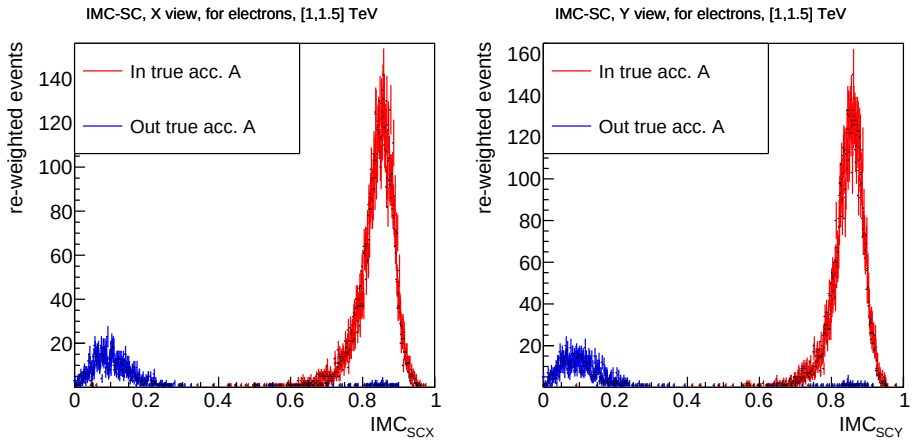

Figure 4.19. *IMC_{SCX} (left panel) and IMC_{SCY} (right panel) for electrons in the energy bin* $[1, 1.5]$ TeV *with the true direction within the acc. A (red histogram) and outside of acc. A (blue histogram) obtained with the EPICS simulation.*

The first cut studied in order to reject the contamination due to events out of acceptance is named "IMC shower concentration" (IMC-SC). Exploiting the fact that a typical electromagnetic shower starts in the IMC tungsten layers, for an electron a large energy deposit near the true particle direction is present in the last layer of the IMC. On the contrary, if the intersection with the last IMC layer of the reconstructed track is distant with respect to intersection of the true track, the energy deposit near the reconstructed track is small with respect to the total energy deposit in the last IMC layer. As an example, the contaminating event shown in fig. 4.17 features a large deposit on the last IMCX layer but not sufficiently concentrated around the reconstructed track.

Two variables, one related to the X view and the other to the Y, are defined for this

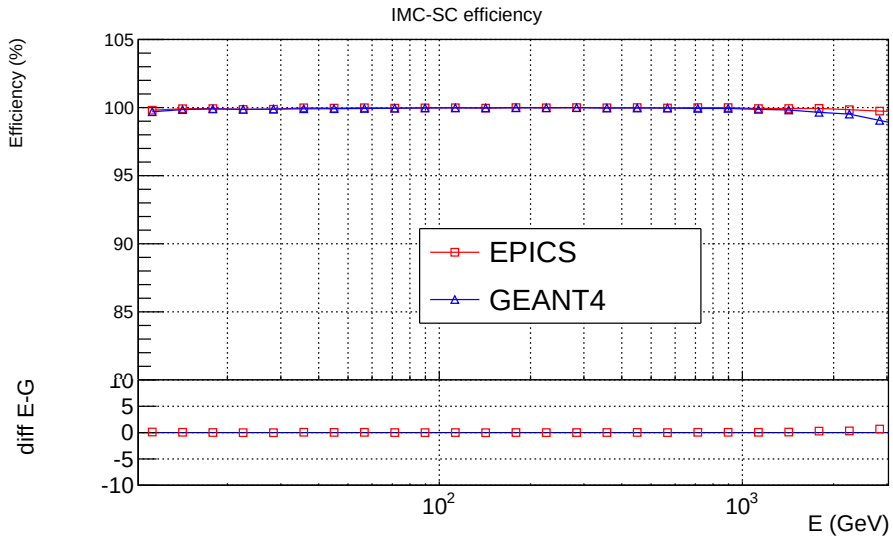

Figure 4.20. *Comparison of the efficiencies of IMC-SC cut as a function of the reconstructed kinetic energy of electrons obtained with the EPICS (red squares) and GEANT4 (blue triangles) MC simulations. The small bottom panel shows the absolute difference between the EPICS and GEANT4 results.*

cut: IMC_{SCX} (IMC_{SCY}) is defined as the energy deposit in the last IMC X (Y) layer within 1 Moliére radius of the tungsten (equal to 9 SciFis) from the reconstructed particle direction divided by the total energy deposit in the last IMC X (Y) layer. The distribution of the IMC-SC variables for electrons in the energy bin $[1, 1.5]$ TeV with the true direction within the acc. A (red histogram) and contaminating events (blue histogram) are shown in fig. 4.19. The bulk of contaminating events have a small IMC-SC. In this analysis this cut rejects all the events with a IMC_{SCX} or IMC_{SCY} less than 0.4. The efficiency of this cut for electrons with the true direction within the acc. A is greater than 98% as shown in fig. 4.20.

In addition to the IMC-SC, a cut named "TASC consistency" (TASC-C) is employed to further reduce the residual contamination due to out-of-acceptance events. The variables "$TASC_{CX}$" and "$TASC_{CY}$" related this cut are:

$$TASC_{CX} = \frac{\sum_{i=1}^{3} D_i(X)}{3};\ TASC_{CY} = \frac{\sum_{i=1}^{3} D_i(Y)}{3},$$

where i enumerates the first 3 layers for each view and $D_i(X)$ ($D_i(Y)$) is the distance in cm between the interception point of the reconstructed track with the i-th TASCX (TASCY) layer and the centre of the log with the maximum energy deposit. The

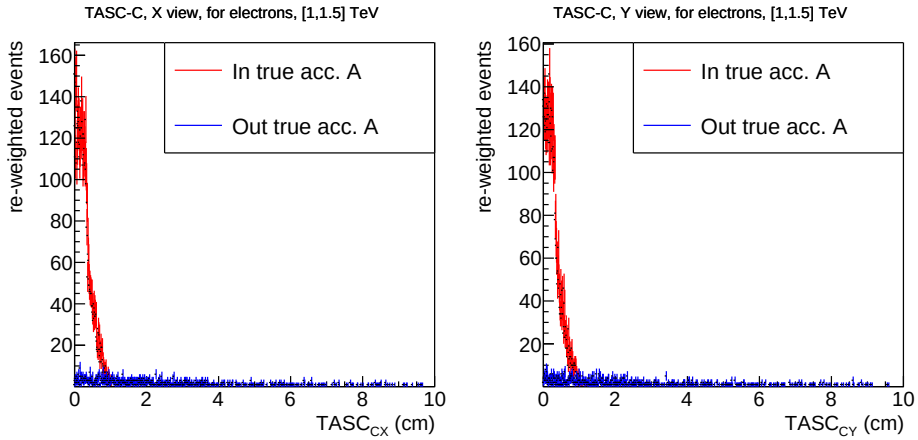

Figure 4.21. *$TASC_{CX}$ (left panel) and $TASC_{CY}$ (right panel) for electrons in the energy bin* $[1, 1.5]$ TeV *with the true direction within the acc. A (red histogram) and outside of acc. A (blue histogram) obtained with the EPICS simulation.*

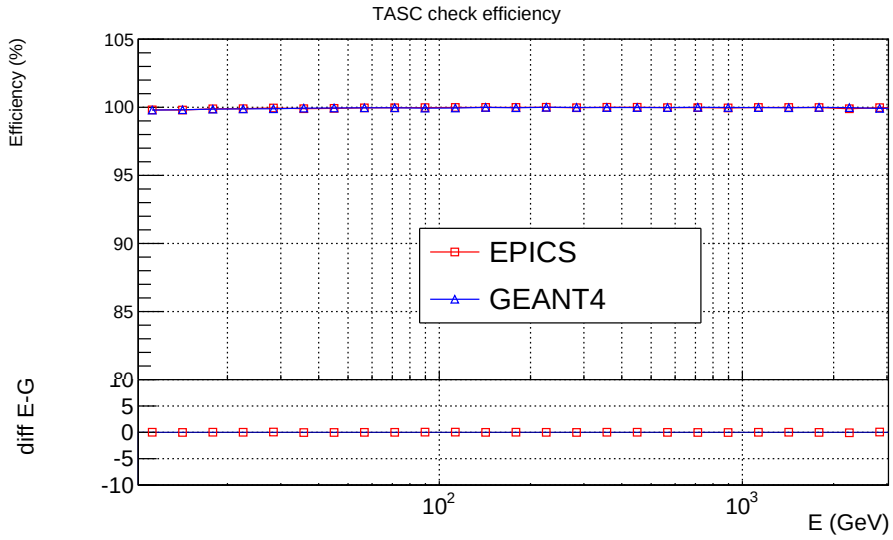

Figure 4.22. *Comparison of the efficiencies of TASC consistency cut as a function of the reconstructed kinetic energy of electrons obtained with the EPICS (red squares) and GEANT4 (blue triangles) MC simulations. The small bottom panel shows the absolute difference between the EPICS and GEANT4 results.*

distribution of this variable for electrons in the energy bin $[1, 1.5]$ TeV is shown in fig. 4.21: a large portion of contaminating events has a value higher than good reconstructed events. For this reason the TASC-C cut reject all the events with "$TASC_{CX}$" or "$TASC_{CY}$" greater than 2 cm. The efficiency of this event selection is shown in fig. 4.22 and it is about 100%.

The residual contamination after the IMC-SC and TASC-C cuts obtained with the

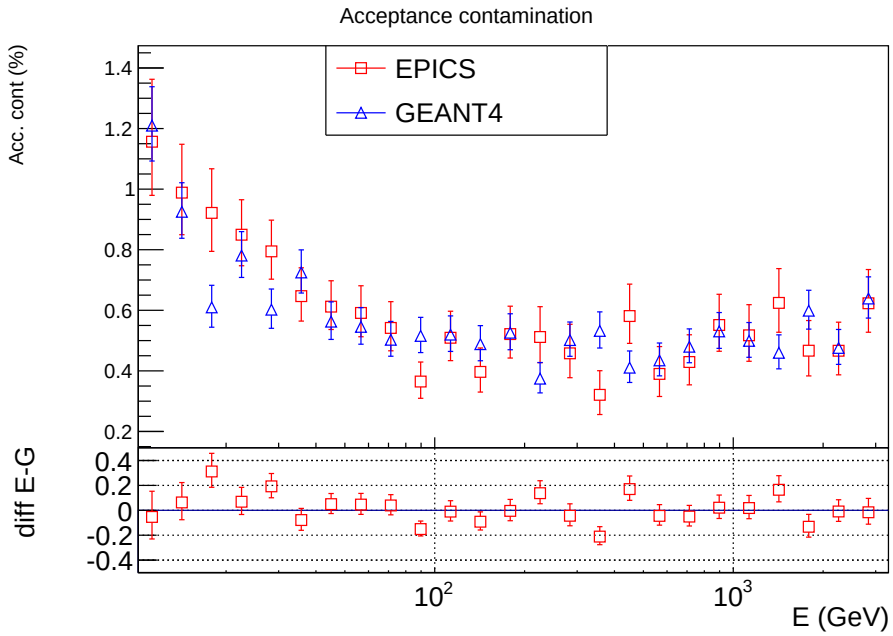

Figure 4.23. *Comparison of the residual acceptance contamination as a function of the reconstructed kinetic energy of electrons obtained with the EPICS (red squares) and GEANT4 (blue triangles) MC simulations. The small bottom panel shows the absolute difference between the EPICS and GEANT4 results.*

EPICS and GEANT4 simulation is shown in fig. 4.23: the residual contamination is below 1.5% and it decreases with the reconstructed kinetic energy up to $\sim$ 100 GeV. Some differences between the MC results are present but it can be related to the different condition of the particle generation. As described in §4.2 particles are propagated in the GEANT4 simulation only if the true trajectory is inside a loose acceptance, thus particles with a very inclined trajectory are not simulated. Indeed, the residual contamination obtained with GEANT4 is slightly smaller than the one obtained with EPICS, thus the EPICS results is used as the reference for this study.

4.6.5 Charge selection with the CHD

In order to reject helium and heavier nuclei different charge selections were studied. Here a simple cut based on the energy deposit in the CHD is used while refined cuts, specifically studied for the proton and nuclei analysis, are discussed in [66]. This cut involves the energy deposit in CHDX and CHDY paddles crossed by the reconstructed particle track, named $CHDX_{hit}$ and $CHDY_{hit}$. If the reconstructed track intercepts only one paddle of the CHDX (CHDY) layer and the minimum distance between the track and the lateral edge of the paddle is greater than 1 mm, $CHDX_{hit}$ ($CHDY_{hit}$) is

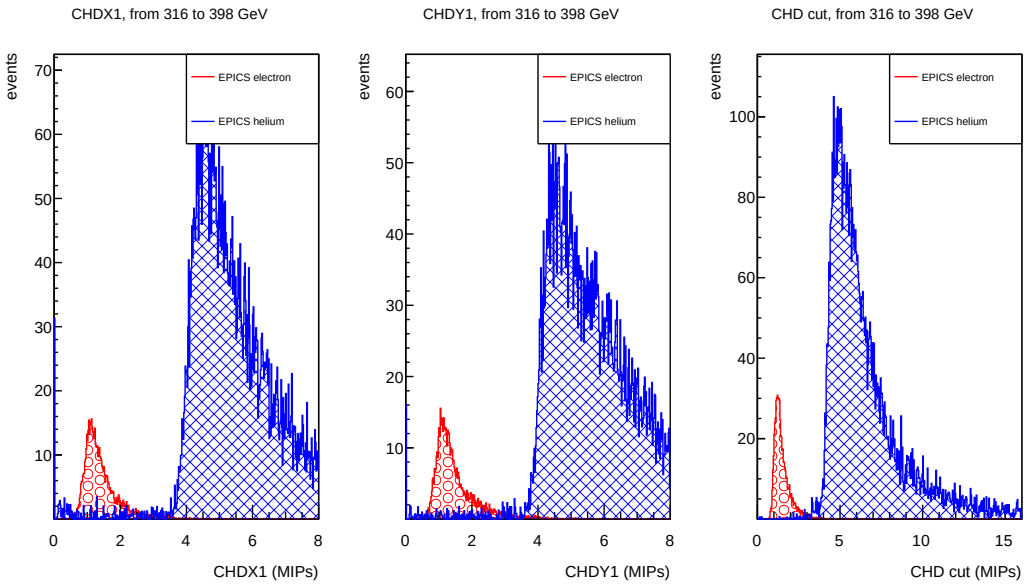

Figure 4.24. *Distribution of $CHDX_{hit}$ (left panel), $CHDY_{hit}$ (middle panel) and the quadratic mean used for the charge cut (right panel) for electrons (red histograms) and helium nuclei (blue histograms) in the energy bin* $[316, 398]$ GeV *obtained with the EPICS simulation.*

the energy deposit in this paddle, otherwise if the minimum distance is less than 1 mm, $CHDX_{hit}$ ($CHDY_{hit}$) is the sum of the energy deposit in the crossed paddle and the paddle nearby the particle trajectory, else if the reconstructed track cross two paddles $CHDX_{hit}$ ($CHDY_{hit}$) is the sum of the energy deposit in these. The variable used for the charge cut is the square mean of $CHDX_{hit}$ and $CHDY_{hit}$: the distributions of this quadratic mean for electrons (red histogram) and helium nuclei (blue histogram) at ~ 350 GeV are shown in fig. 4.24. The CHD cut clearly shows a good separation between the electron and helium peaks. For the pre-selection all the events with a square mean of $CHDX_{hit}$ and $CHDY_{hit}$ greater than 3.5 MIP are rejected. The efficiency of this cut is shown in fig. 4.25: it is almost constant at 100% below 500 GeV and it slightly decreases at higher energy. Furthermore, in the TeV region a discrepancy of about 5% between GEANT4 and EPICS is present: this is probably due to the different treatment in backscattered particle described in §3.2. The effect of this discrepancy between the EPICS and GEANT4 simulation on the electron measurement is discussed in §4.9.

To estimate the residual helium contamination after this cut, the re-weighting procedure of the MC simulation applied to protons and electrons, described in §4.2, is also

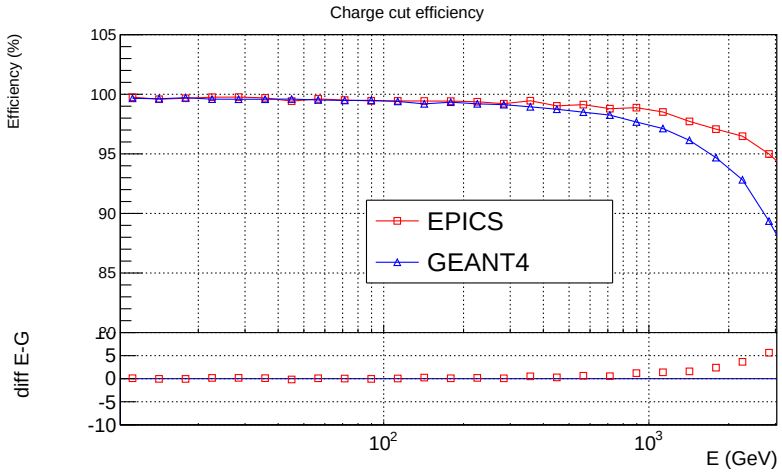

Figure 4.25. *Comparison of the efficiencies of the CHD cut as a function of the reconstructed kinetic energy of electrons obtained with the EPICS (red squares) and GEANT4 (blue triangles) MC simulations. The small bottom panel shows the difference between the EPICS and GEANT4 results.*

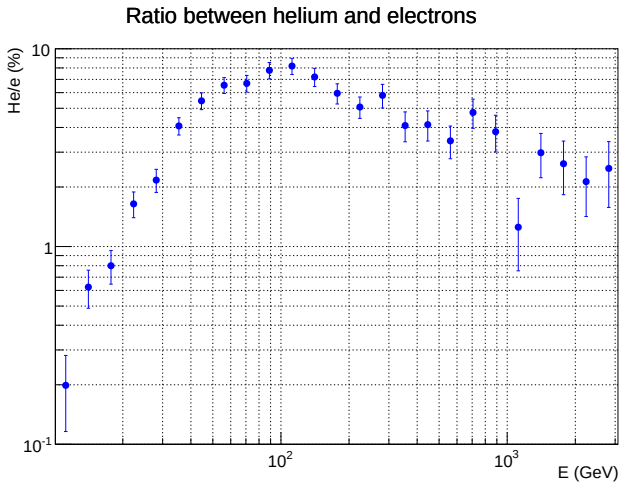

Figure 4.26. *Ratio between the number of helium and electron events after the charge cut as a function of the reconstructed kinetic energy obtained with the EPICS simulation.*

applied to the helium events, using a fit of the flux measured by AMS-02 [38] with a broken power-law and a correction factor for the low-energy range, as explained for the proton re-weighting procedure. The abundance of the helium peaks in fig. 4.25 is obtained with this re-weighting procedure. The ratio between the number of helium and electron events that survives the cut as a function of the reconstructed kinetic energy obtained with the EPICS simulation is shown in fig. 4.26. The contamination is below 10% and it reaches a maximum around 100 GeV since in the low-energy region the SW-HET and the IMC-SC reject many helium simulated events while in

the high-energy region the CHD cut strongly suppresses the helium contamination. This contamination factor is not negligible at this stage of this analysis but it further decreases after the electron/proton discrimination cut as explained in the next section.

4.7 Electron/proton discrimination cuts

The pre-selection presented in the previous section is designed to select electrons with very high efficiency, rejecting contaminating events due to events out of acc. A and nuclei. The total efficiency of these selection cuts is shown in fig. 4.27: the discrepancies between EPICS and GEANT4 are mainly due to the CHD cut. The pre-selection is studied for electrons and the efficiency for protons is small, about 30% for protons with a reconstructed kinetic energy equal to 100 GeV, mainly due to the SW-HET and IMC-SC cuts. Despite that, since the proton differential flux is about 100-1000 times higher than the electron flux, the proton contamination remains very high at this step of the analysis: the number of events selected with the pre-selection for electrons and protons obtained with the EPICS simulation, after the re-weighting procedure according to the AMS-02 data, is shown in fig. 4.28. The number of selected protons is greater than the number of electrons and a strong proton rejection cut is needed to avoid a large proton contamination. Since the energy resolution of CALET for protons is worse than the one for electrons, about 35% for protons above 100 GeV, the distribution of the true kinetic energy of protons which fill each bin of reconstructed energy is very large: fig. 4.29 shows the distribution of the kinetic energy for protons in the bin of reconstructed energy at $\sim$ 100 GeV and $\sim$ 1 TeV. The MPV of the distributions are $\sim$ 3.5 times larger than the centre of the bins and the high-energy tail reaches very high-energy, about 10 times larger with respect to the bin centres.

In order to reject protons, two different approaches are discussed in this thesis, the first one based on a single discriminant cut involving standard variables, and a second approach based on a Multi Variate Analysis (MVA) algorithm.

4.7.1 Simple cut with the K variable

The electron/proton discrimination cut discussed here involves the development of the shower in the TASC. Two variables are used: the first (F_E) is the energy deposited in

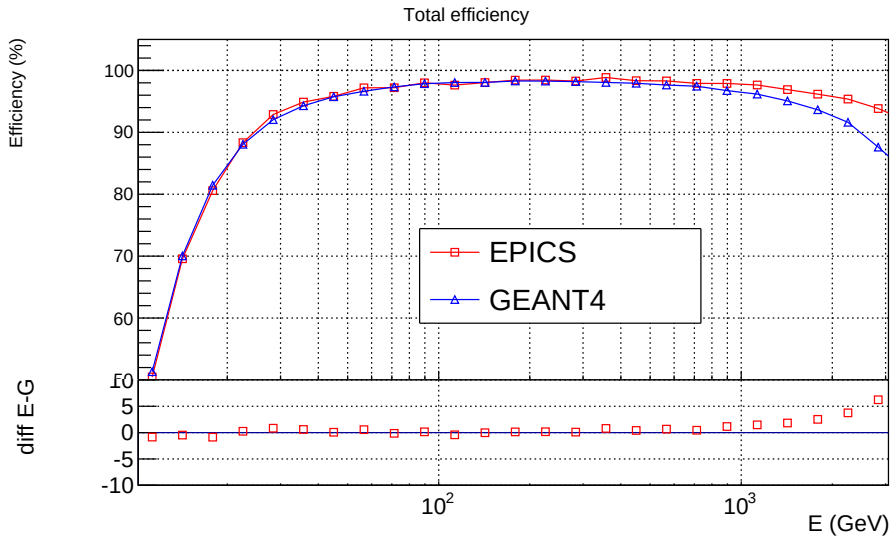

Figure 4.27. *Comparison of the total efficiencies of the pre-selection as a function of the reconstructed kinetic energy of electrons obtained with the EPICS (red squares) and GEANT4 (blue triangles) MC simulations. The small bottom panel shows the absolute difference between the EPICS and GEANT4 results.*

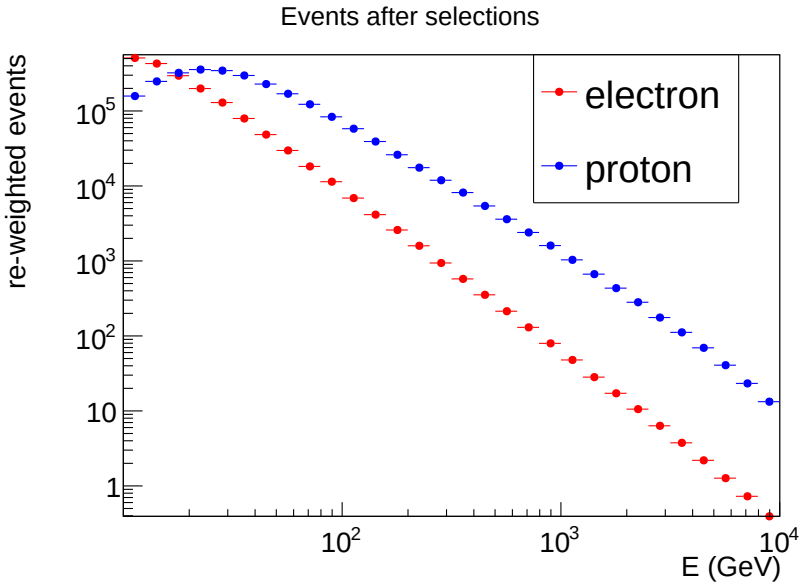

Figure 4.28. *Number of events selected by the pre-selection for electrons (red points) and protons (blue points) obtained with the EPICS simulation.*

the last (bottom) TASC layer divided by the total energy deposited in the TASC; this is related to the longitudinal shower development and in hadronic showers this value is bigger than in electromagnetic ones. Since a 3 MIP cut is applied to all the TASC logs, as described in §4.2, for events which have all the signals of the last TASC layer below this threshold, the energy deposit in this layer is replaced with 3 MIP.

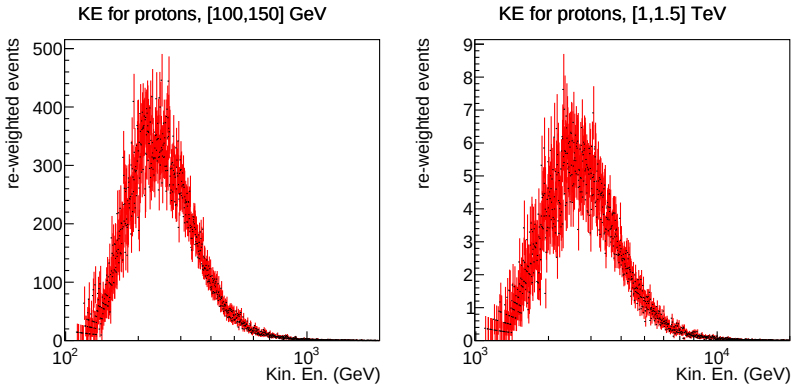

Figure 4.29. *Kinetic energy for protons in the reconstructed energy* $[100, 150]$ GeV *(left panel) and* $[1, 1.5]$ TeV *(right panel).*

The second variable (R_E) is the energy-weighted spread in the first (topmost) TASC layer: it takes into account the lateral profile of the early part of the shower and it is given by:

$$R_E = \sqrt{\frac{\sum_j (\Delta E_j \cdot (x_j - x_c)^2)}{\sum_j \Delta E_j}},$$

where x_c is the coordinate of the reconstructed particle track in the first TASC layer, x_j and ΔE_j are the coordinate of the centre and the energy deposit in the jth PWO log respectively. These variables are chosen not only to achieve a high proton rejection power but also in order to get a good agreement between the MC simulation and the flight data; in §4.8 some comparisons between the distributions of variables obtained with the simulation and flight data are presented. Fig. 4.30 and fig. 4.31 show the distribution of F_E (right panel) and R_E (middle panel) for electrons (red) and protons (blue) at ~ 100 GeV and ~ 1 TeV respectively, obtained with the EPICS simulations. The F_E distributions feature a different population of the two distribution components: a narrow peak at low F_E due to the 3 MIP cut and broad peak at high F_E. The rejection power of the F_E can be enhanced by properly combining the F_E with R_E. Thus, in order to improve the cut efficiency for electrons, while keeping a good discrimination power, the discrimination cut is applied on a single variable (K) obtained by combination of the two variables as follows:

$$K = log_{10}(F_E) + 0.65 \cdot \frac{R_E}{1 \text{ cm}},$$

where the 0.65 numeric parameter is selected in order to maximize the rejection power at 1 TeV. An event selection based on this variable represents a linear cut in the two-

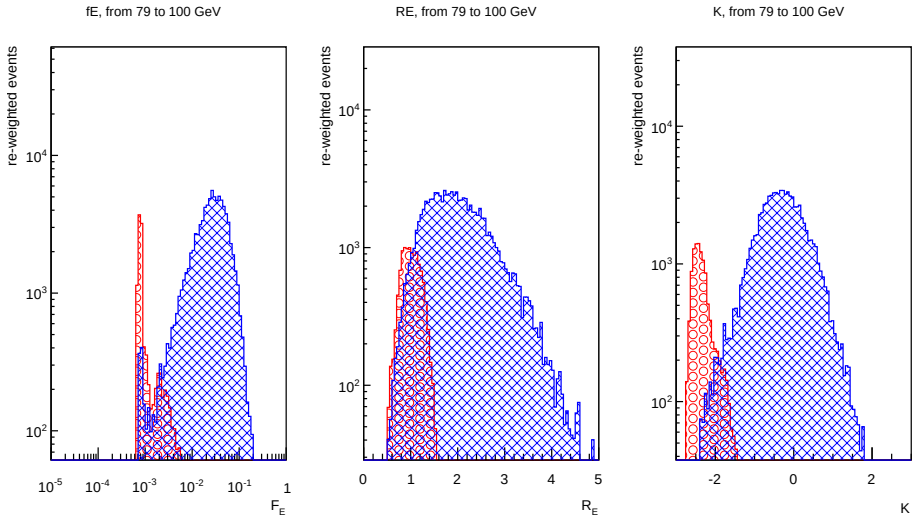

Figure 4.30. *F_E (left panel), R_E (middle panel) and K (right panel) distributions for electrons (red) and protons (blue) in the energy bin* $[79, 100]$ GeV *obtained with EPICS.*

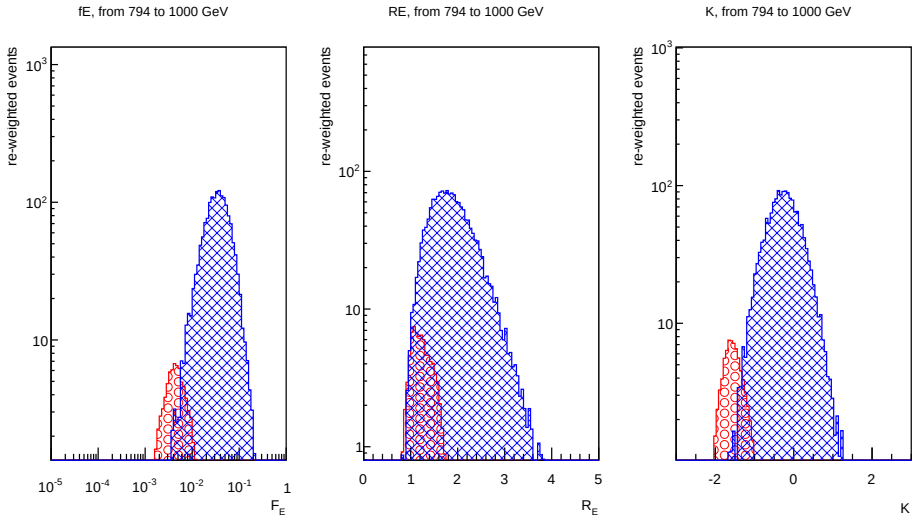

Figure 4.31. *F_E (left panel), R_E (middle panel) and K (right panel) distributions for electrons (red) and protons (blue) in the energy bin* $[0.79, 1]$ TeV *obtained with EPICS.*

dimensional plot with the $log_{10}(F_E)$ on the Y axis and R_E on the X axis: this plot for electrons and protons at ~ 1 TeV obtained with the EPICS simulation is shown in fig. 4.32. The black line represents the cut on the two-dimensional plot applied in this energy bin; events above the black line are rejected. This is equivalent to employ a single cut with the K variables, by using a threshold of about -1.4, rejecting all the events with $K > -1.4$. The distributions of the K variable obtained with EPICS for electrons and protons in two energy bins are shown in the right panel of fig. 4.30 and fig. 4.31.

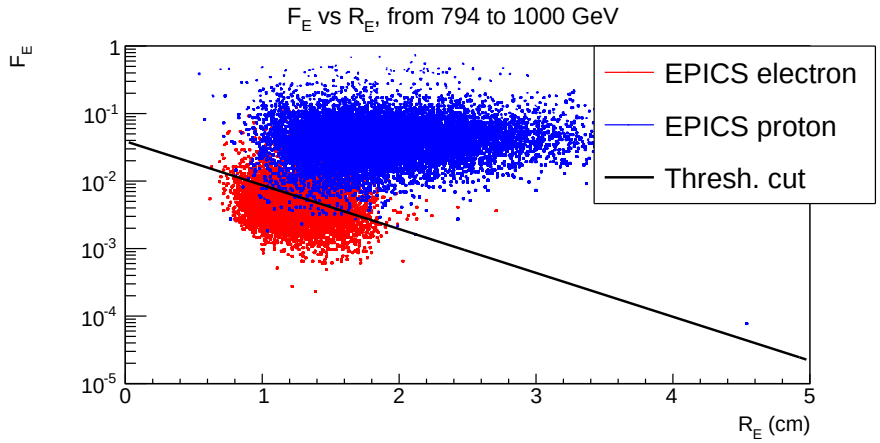

Figure 4.32. *F_E vs R_E plot for electrons (red) and protons (blue) in the energy bin* $[0.79, 1]$ TeV *obtained with EPICS. The black line is the two-dimensional cut applied in this energy bin.*

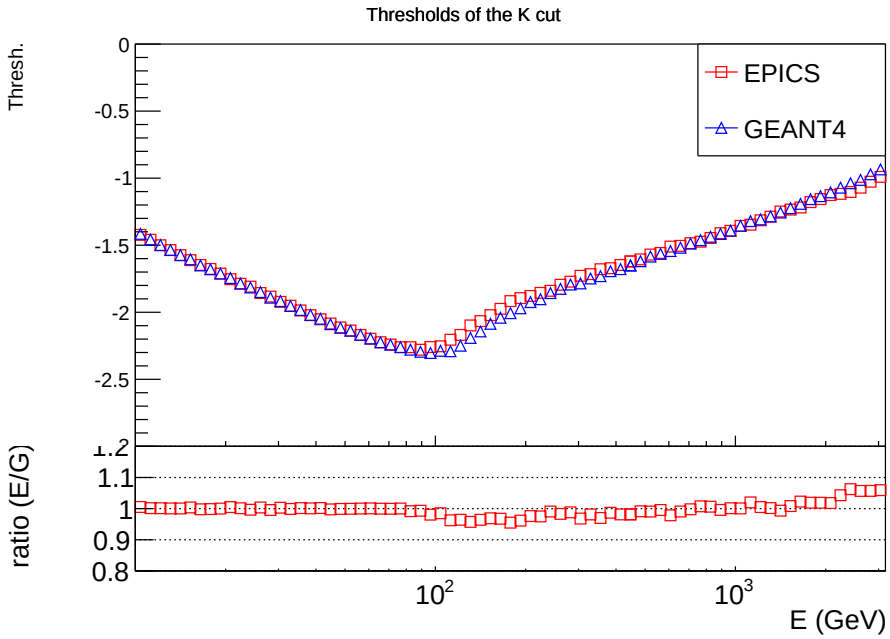

Figure 4.33. *Thresholds used for the K cut corresponding to a constant selection efficiency of* 70% *computed with EPICS (red squares) and GEANT4 (blue triangles). The bottom panel shows the ratio between EPICS and GEANT4.*

By employing the MC simulation, the thresholds for the cut on the K variables are chosen in order to achieve a constant efficiency of 70% of this selection for electrons in each energy bin. The thresholds computed with the EPICS and GEANT4 simulations are shown in fig. 4.33. The trend of the threshold is dominated by the F_E variables.

Below $\sim$ 100 GeV the energy deposit by electrons in the logs of the last TASC layer is in most cases below 3 MIP thus the F_E is computed as 3 MIP divided by the total energy deposited in TASC, therefore the F_E decreases with energy. Above $\sim$ 100 GeV the 3 MIP cut on the energy deposit in the TASC logs does not affect the F_E and the latter increases with energy since the shower development becomes progressively deeper with increasing energy. The discrepancy between GEANT4 and EPICS is less than 5%.

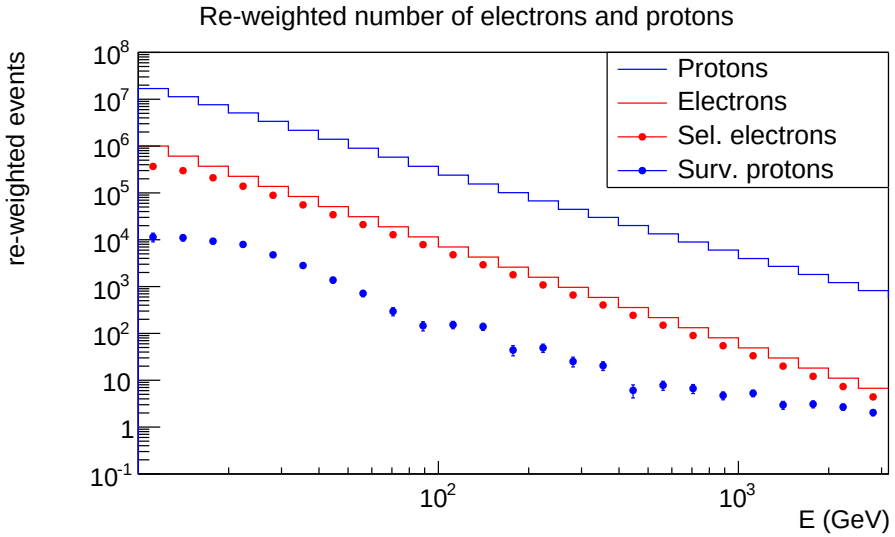

Figure 4.34. *Re-weighted number of electrons (red) and protons (blue) in each bin of reconstructed energy before (red and blue histograms) and after (red and blue points) the event selection that it include both the pre-selection and the rejection cut with the K variable.*

Fig. 4.34 shows the re-weighted number of electrons (red points) and protons (blue points) selected with the pre-selection and the K cut, compared with the initial re-weighted number of events in each bin of reconstructed energy and with the true track inside the acc. A, obtained with the EPICS MC simulations without the application of the selections. The rejection power for protons is very high, since the re-weighted number of selected protons in each energy bin is $10^{-4} \div 10^{-5}$ times the initial re-weighted number of protons, while about the 70% of the electrons pass the selections. The residual proton contamination, here defined as the re-weighted number of protons divided by the number of electrons selected with the pre-selection and the K cut, obtained with EPICS and GEANT4, is shown in 4.35. The proton contamination is below 10% for electrons below 1 TeV according to the EPICS simulation. There are some discrepancies between EPICS and GEANT4 especially for electrons below 50 GeV, where

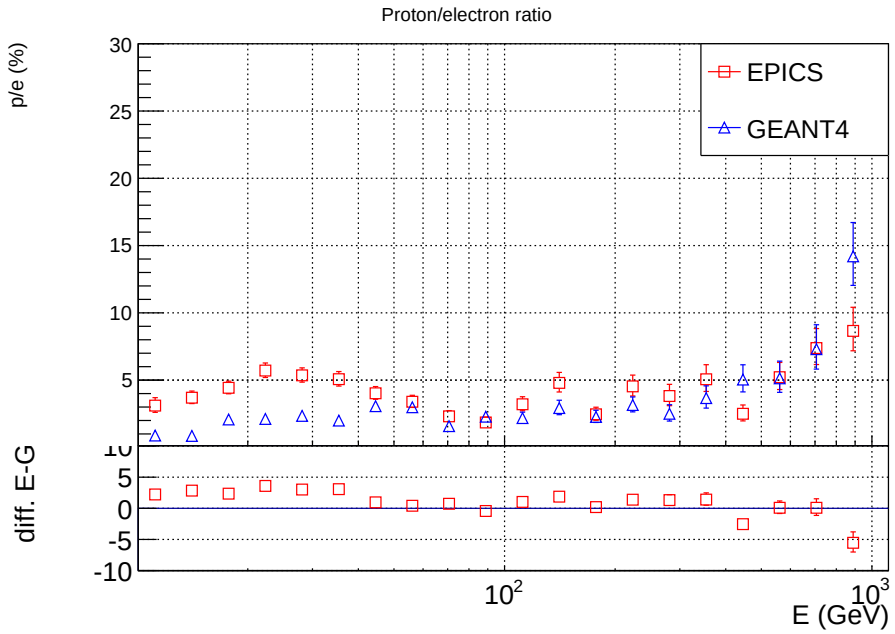

Figure 4.35. *Proton contamination, defined as the re-weighted number of protons divided by the re-weighted number of electrons selected with the pre-selection and the K cut, obtained with EPICS (red square) and GEANT4 (blue triangles). The small bottom panel shows the absolute difference between the EPICS and GEANT4 results.*

GEANT4 features a lower contamination with respect to EPICS, and in the last energy bin, while in the range $[50, 900]$ GeV the agreement is good, with differences of only a few percent. The K cut is designed to well discriminate electrons below 1 TeV and is useful in this energy range to select electrons with a simple variable for comparison between MC and flight data.

4.7.2 Rejection cut with MVA

To improve the e/p discrimination up to the multi-TeV region, while keeping a high efficiency for electrons, a Multi Variate Analysis (MVA) approach has been developed. Preliminary comparison [86] between different MVA algorithms showed that the *"Boosted Decision Trees"* (BDT) is the most promising one. The algorithm employed in this analysis is contained in the TMVA tool-kit [85], a package integrated into the Root data analysis framework which contains a large variety of multivariate classification algorithms based on machine learning techniques. In this work, the BDT algorithm is used to classify events as signal or background, i.e. to separate electrons from protons. During the "training" step of the algorithm, the MC simulations of

electrons and protons are used to build a decision tree, based on a set of discriminating variables. This tree consists of a sequence of binary splits; each split involves a single discriminating variable that, at this split, gives the best separation between signal and background. The data are processed with subsequent binary decisions until a stop criterion is fulfilled, i.e. when no other splits are present in the current branch. The algorithm is named *"Boosted Decision Trees"* since it is an enhanced ("boosted") version of a standard decision tree: this is a well-known method for improving the classification performance of MVAs based on decision trees by sequentially applying the MVA algorithm to re-weighted versions of the training data; see [85], pages 54-56, for a precise description of this method.

This MVA analysis has been developed and properly optimized with the EPICS simulation. The main variables involved in the MVA analysis are the F_E and R_E and also other variables are included: these are selected taking into account both the discrimination power and the agreement between the MC and the flight data distributions, as discussed in §4.8. The first variable included is related to the IMC-SC, described in sec. 4.6.4, where it was used as a weak cut in order to avoid contamination from out-of-acceptance particles. In the MVA analysis the variable IMC-SC is defined as the mean of IMC_{SCX} and IMC_{SCY}. This selection has a proton rejection power similar to the R_E variable. The distributions of the main discriminating variables, i.e. F_E, R_E and IMC-SC, for protons and electrons obtained with EPICS in two bins of reconstructed energy are shown in fig. 4.36 and fig. 4.37.

Other variables employed in the MVA analysis represent the TASC longitudinal shower profile parameters: by using the energy deposit in each TASC layer, the longitudinal shower profile is fitted with a Gamma distribution:

$$\frac{dE}{dt} = E_0 \frac{(t-t_0)^{\alpha-1} e^{\frac{(t-t_o)}{\theta}}}{\Gamma(\alpha)\theta^{\alpha}}, \tag{4.8}$$

where t is the depth in units of X_0, θ is a scale parameter (in units of X_0), α is a shape parameter, E_0 is the total energy of the shower (in GeV) and t_0 is the shower starting point defined as the point where $\frac{dE}{dt} = 0$. As an example, the longitudinal profile of an electromagnetic shower at 91 GeV simulated with EPICS is shown in fig. 4.38. The

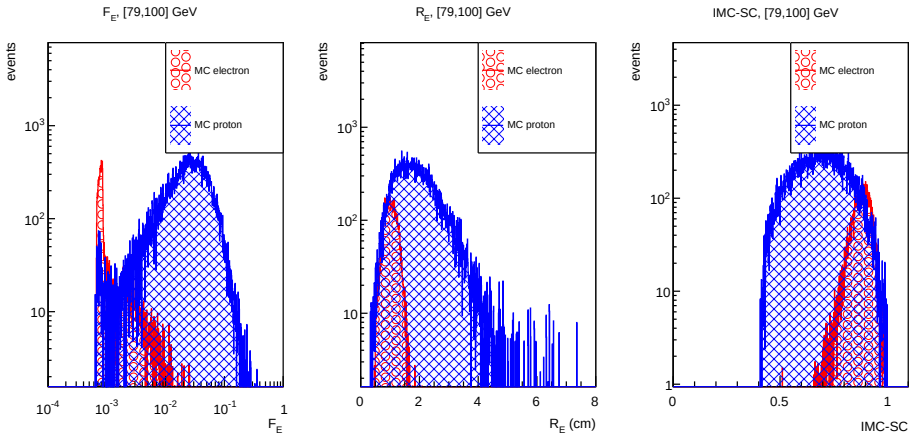

Figure 4.36. *F_E (left panel), R_E (middle panel) and IMC-SC (right panel) distributions for electrons (red) and protons (blue) in the energy bin* $[79, 100]$ GeV *obtained with EPICS.*

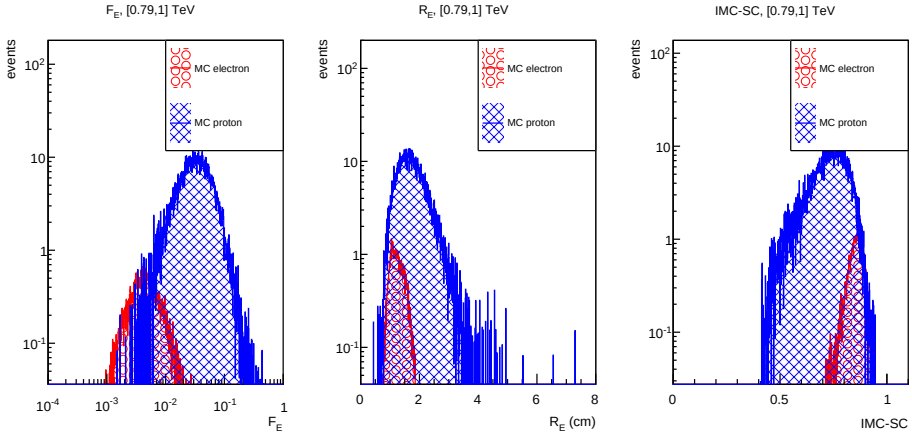

Figure 4.37. *F_E (left panel), R_E (middle panel) and IMC-SC (right panel) distributions for electrons (red) and protons (blue) in the energy bin* $[0.79, 1]$ TeV *obtained with EPICS.*

values of $\frac{dE}{dt}$ shown on the Y axis are approximated with:

$$\frac{dE}{dt} = \frac{E_i}{\Delta t_i},$$

where E_i is the energy deposit in the i-th layer and Δt_i is the thickness ($\sim 2X_0$) of the i-th layer itself, expressed in units of X_0 and multiplied by the cosine of the angle of the reconstructed track to correct for track inclination. t is shown on the X axis and it is defined as the depth of the TASC layer multiplied by the cosine of the angle of the reconstructed track. The TASCY5 layer is removed from this plot for an improvement of the fit performance, since this layer contains 3 "dead" channels. The red line in

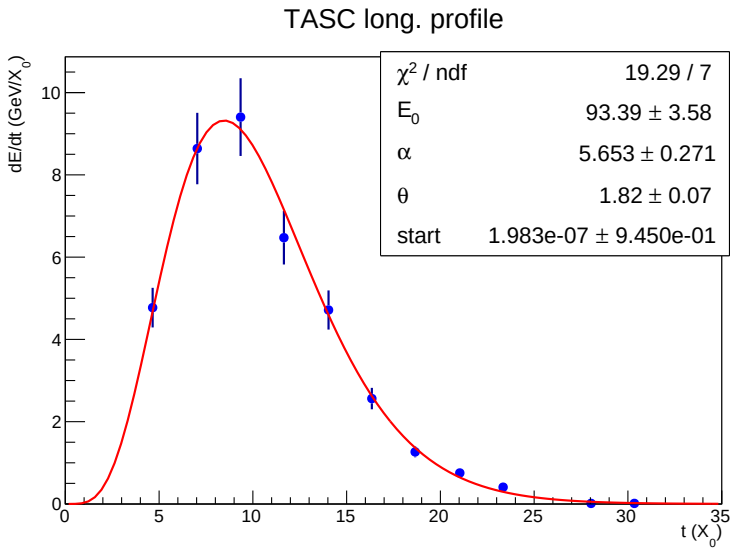

Figure 4.38. *Longitudinal profile of a shower in TASC induced by an electron at* 91 GeV *simulated with EPICS. The red line is the fit of the histogram with the gamma function (eq. 4.8).*

fig. 4.38 represents the fit of the histogram with eq. 4.8 (t_0 is indicated with "start" parameter in the figure).
Three variables related to this fit are included in the BDT algorithm: the point of the maximum of the function $t_{max} = (\alpha - 1)\theta$, the θ parameter and the reduced χ^2 of the fit. The distribution of these variables for protons and electrons obtained with EPICS in two bins of reconstructed energy are shown in fig. 4.39 and fig. 4.40.

Similarly, the longitudinal signal distribution in the IMC can be described with:

$$E(t) = p_0 + p_1 \cdot t^2, \tag{4.9}$$

where t is the depth of the IMC layers expressed in units of X_0 and multiplied by the cosine of the angle of the reconstructed track, $E(t)$ is the energy deposit in the IMC layers at depth t and p_0, p_1 are phenomenological parameters. Fig. 4.41 shows an example of the shower profile in IMC obtained with an electron at 91 GeV simulated with EPICS. In the plot only the IMC layers with a total energy deposit greater than 5 MIP are included; p_0, p_1 and the χ^2 of the fit are used within the BDT analysis; the distributions of these variables are shown in fig. 4.42 and fig. 4.43.
In summary, the 9 variables included within the MVA analysis are:

- F_E, R_E and IMC-SC,

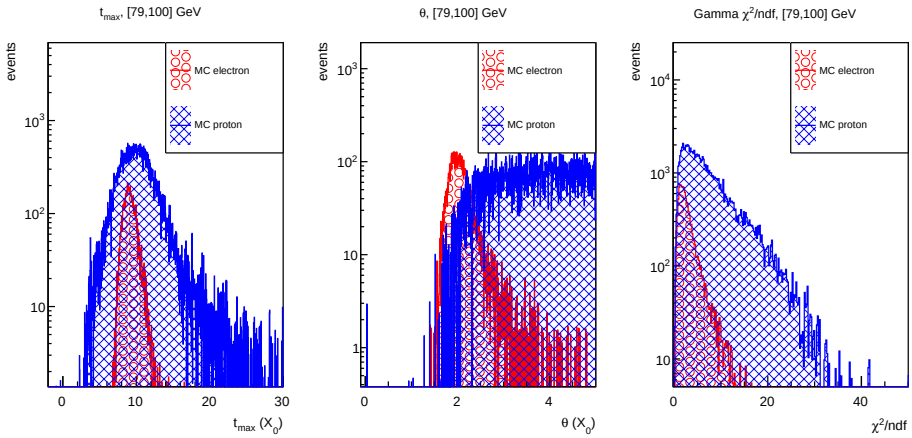

Figure 4.39. *Parameters t_{max} (left panel), θ (middle panel) and the reduced χ^2 (right panel) of the gamma fit, for electrons (red) and protons (blue) in the energy bin* $[79, 100]$ GeV *obtained with EPICS.*

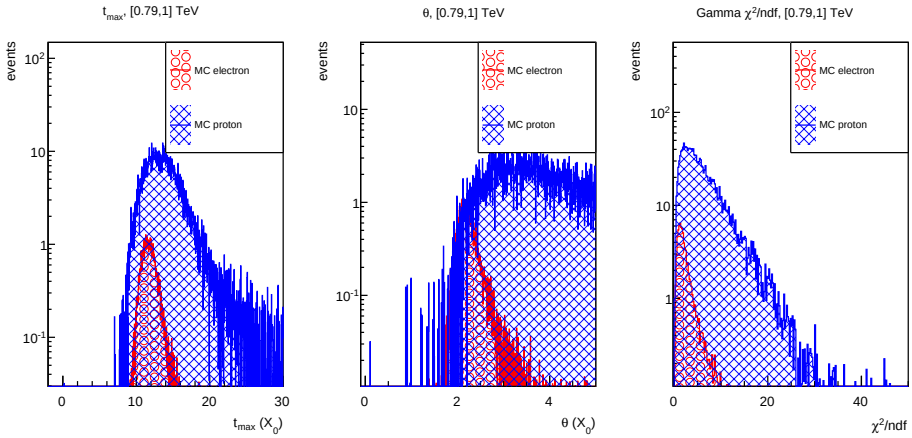

Figure 4.40. *Parameters t_{max} (left panel), θ (middle panel) and the reduced χ^2 (right panel) of the gamma fit, for electrons (red) and protons (blue) in the energy bin* $[0.79, 1]$ TeV *obtained with EPICS.*

- the t_{max}, θ parameters and the reduced χ^2 of the Gamma fit.
- the p_0, p_1 parameters and the χ^2 of the IMC fit.

To properly train and test the MVA algorithm, the generated proton and electron events are separated in two samples. The first one is used for the BDT training, and the other one for the test of the analysis, i.e. for the calculation of the efficiency and the proton contamination. For each energy bin an independent BDT training and test is carried out in order to optimize the rejection power.
In each energy bin only the variables that show a good agreement between the EPICS MC simulations and the flight data are included in the BDT algorithm, see §4.8. For

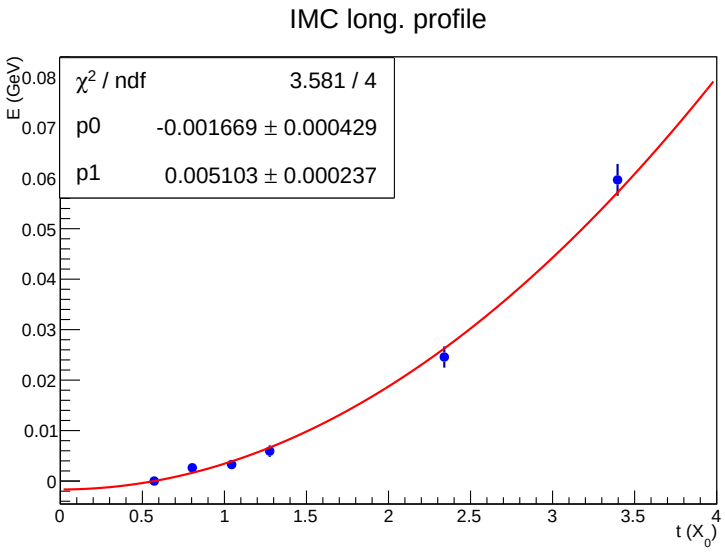

Figure 4.41. *Longitudinal profile of a shower in IMC induced by an electron at* 91 GeV *simulated with EPICS. The red line is the fit of the histogram by using the eq. 4.9.*

this purpose, the energy range can be divided in 3 segments:

- below 100 GeV: only F_E, R_E and IMC-SC are included since in the low-energy bins the proton rejection power obtained with few variables is sufficient;
- from 100 GeV to 500 GeV: all the variables are included except for the θ parameter of the gamma fit;
- above 500 GeV: all the variables are included except the IMC-SC.

The output variable of the BDT algorithm assumes a value greater than 0 for electrons and less than 0 for protons in most cases. The distributions of this variable for the test sample in two bins of reconstructed energy are shown in fig. 4.44 where a good separation of the proton and electron peaks is shown even in the 1 TeV energy bin. The thresholds for this cut are selected with the same method used for the K cut analysis by using the test sample and requiring a constant efficiency of 70% for electrons.

The residual proton contamination after the BDT cut corresponding to a constant 70% efficiency is shown in fig. 4.45. The result obtained with the EPICS simulation features a smaller contamination than the one computed with the K cut analysis: it remains below 8% up to 1 TeV. By employing the BDT cut it is possible to extend the

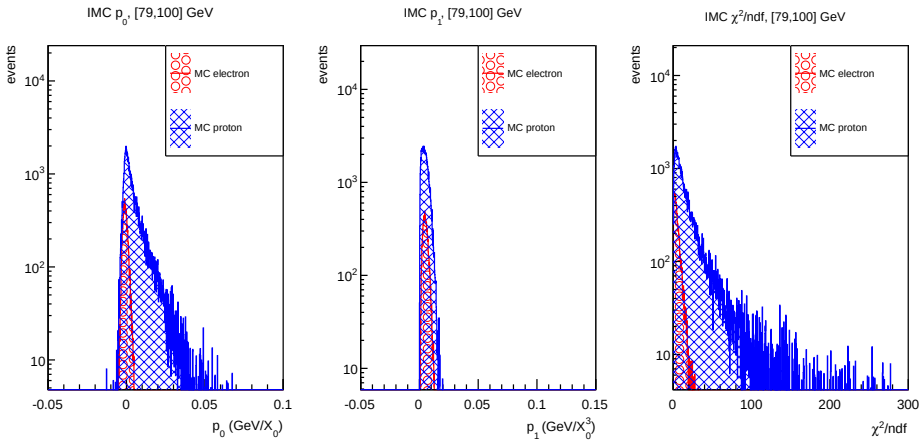

Figure 4.42. *Parameters p_1 (left panel), p_2 (middle panel) and the χ^2 (right panel) of the IMC profile fit, for electrons (red) and protons (blue) in the energy bin* $[79, 100]$ GeV *obtained with EPICS.*

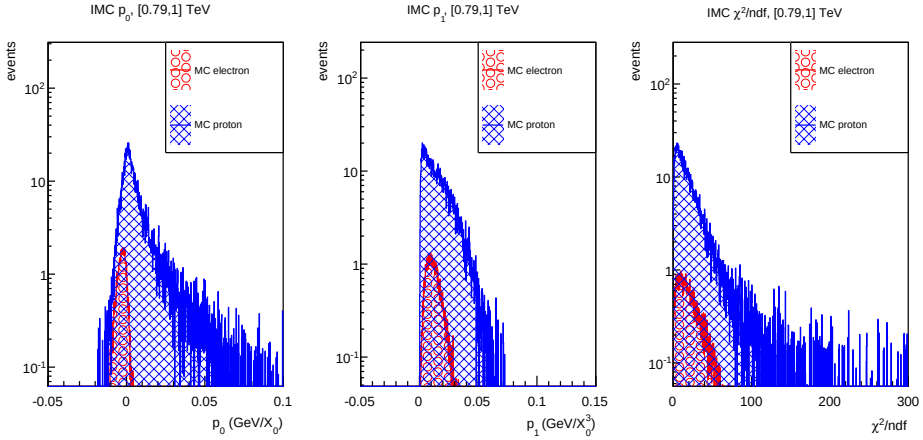

Figure 4.43. *Parameters p_1 (left panel), p_2 (middle panel) and the χ^2 (right panel) of the IMC profile fit, for electrons (red) and protons (blue) in the energy bin* $[0.79, 1]$ TeV *obtained with EPICS.*

analysis up to 3 TeV, where the proton contamination remains around 10% according to EPICS. In order to check the systematic effects due to MC code, the BDT cut calibrated with EPICS has been applied to a test sample of protons and electrons obtained with GEANT4. The proton contamination obtained with this method is shown in fig. 4.45 with blue triangles. The absolute difference between the results obtained with GEANT4 with respect the one obtained with EPICS is smaller than 3% up to 400 GeV, while above differences of order of 5% are present. The bin-by-bin fluctuation of the GEANT4 results seems larger than the EPICS one; these fluctuations are of the same order of the large statistical error bars present in fig. 4.45 due to the statistics of the proton simulation actually available at high-energy. In order to investigate this

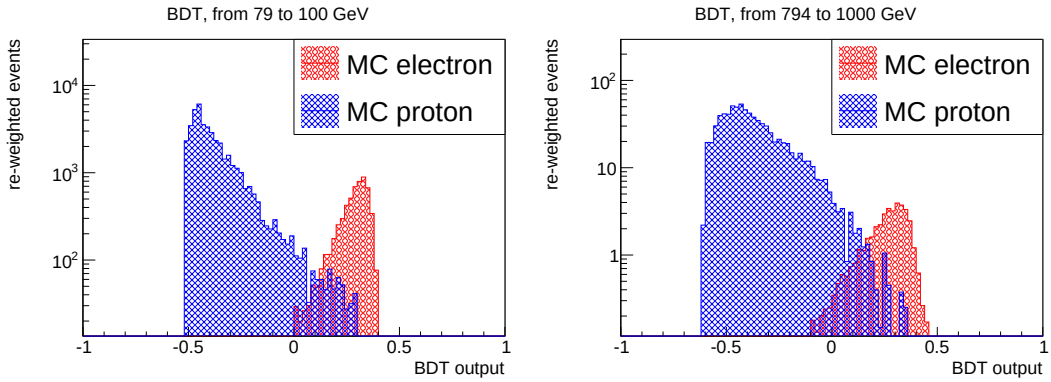

Figure 4.44. *BDT output variable, for electrons (red) and protons (blue) in the energy bin* $[79, 100]$ GeV *(left panel) and* $[0.79, 1]$ TeV *(right panel) obtained with the EPICS simulation.*

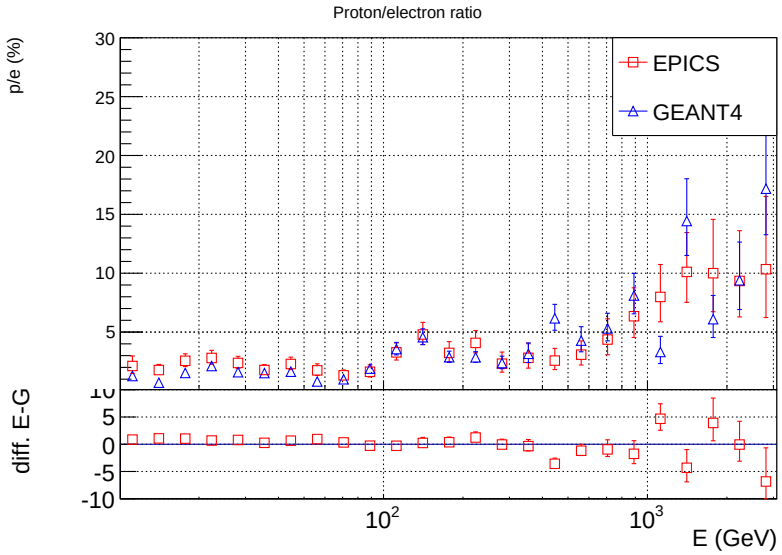

Figure 4.45. *Proton contamination, defined as the re-weighted number of protons divided by the re-weighted number of electrons selected with the BDT cut, obtained with EPICS (red square) and GEANT4 (blue triangles) test data-sets (the training of the MVA employs the EPICS data sample in both cases). The small bottom panel shows the absolute difference between the EPICS and GEANT4 results.*

fluctuation, new GEANT4 proton simulation are running to reduce the statistical error about the proton contamination. The absolute differences between the residual contamination obtained with GEANT4 and EPICS is treated as a systematic error of the electron measurement (see §4.9).

Furthermore, by applying the BDT cut to the helium EPICS simulation almost all the events which survive the pre-selection are rejected by this cut, thus the residual helium contamination after the rejection cut is negligible since it is below 0.5% in the entire

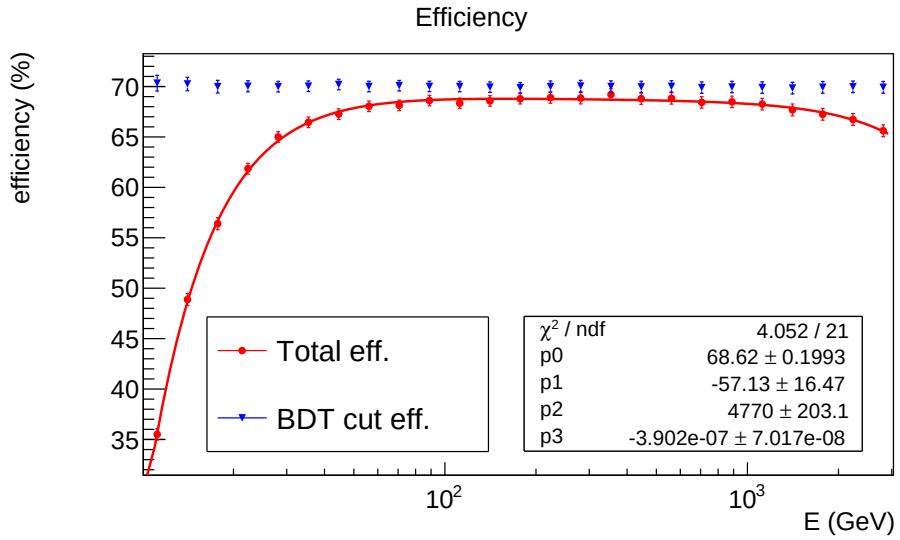

Figure 4.46. *Efficiency of the BDT cut (blue triangles) and total efficiency of the pre-selection combined with the BDT cut (blue circles) as a function of the reconstructed kinetic energy of electrons obtained with the EPICS. The red line is the fit of the total efficiency using eq. 4.10.*

energy range.

Fig. 4.46 shows the efficiency of the BDT cut (blue triangles) and the total efficiency for the electron selection (red points), that it includes both the pre-selection and the BDT cut. The BDT cut efficiency is about 70% in the whole energy range, as expected by construction, while the total efficiency is the product of the BDT cut efficiency and the efficiency of the pre-selection. The red line is a fit of the total efficiency with the following function:

$$F(E) = p_0 - \frac{p_1}{E} - \frac{p_2}{E^2} + p_3 \cdot E^2, \tag{4.10}$$

where E is the reconstructed energy and p_0, p_1, p_2 and p_3 are the fit parameters: the value of these parameters after the fit of the total efficiency are shown in fig 4.46. This phenomenological fit of the total efficiency is used for the computation of the differential electron flux in order to approximate the $\epsilon_{tot}(E)$ terms of eq. 4.5.

4.8 Preliminary Monte Carlo validation with flight data

In this section some comparisons between simulated and flight data about relevant variables used for the electron selection are presented. These are used for a validation of the results obtained with the EPICS and GEANT4 simulations, described in the previous sections. These studies are crucial for the CALET experiment and here only preliminary results are discussed, while a precise comparison, especially for variables that show discrepancies between simulated and flight data, is currently ongoing. As explained in §4.7.2, these studies are also used to select the variables involved in the MVA.

Flight data The flight data used for these comparisons are acquired from the first day of December 2015 to the last day of June 2017. The data acquired in flight contains all the information of the CALET detector, e.g the signals of the CALET channels in units of ADC, the position of the detector on orbit, the temperature of the apparatus etc. This information is written in a binary format named *"L1"*. Afterwards the L1 files are processed with the CALET reconstruction software: the output of this software is named "L2" and it is written in a custom file format based on Root files [87]. The L2 files contain the reconstructed event data, such as the calibrated energy deposits in GeV, the track and charge of the incoming particle, the live time etc. Different versions of the reconstruction software have been developed: the L2 files used in this work contain the results of the most recent version of the tracking and calibration procedure, and they are tagged with the name "PASS 2.0".

MC data The MC data used for these comparisons are already described in §4.2. In order to precisely reproduce the expected number of events in each bin of reconstructed energy, the exposure time (term T in eq. 4.2) used in the MC re-weighting procedure is now equal to the cumulative live time computed with the flight data, of about $4.22512 \cdot 10^7$ s $\sim$ 489 days. By using the CALET reconstruction software the MC data are also converted in the L2 format, thus the event selection is applied to both the flight and MC data by using the exactly same algorithm. Both the flight and the MC data are selected by using the pre-selection while the rejection cuts are not applied, since the main purpose of these comparisons is the validation of the variables

used for the electron/proton discrimination.

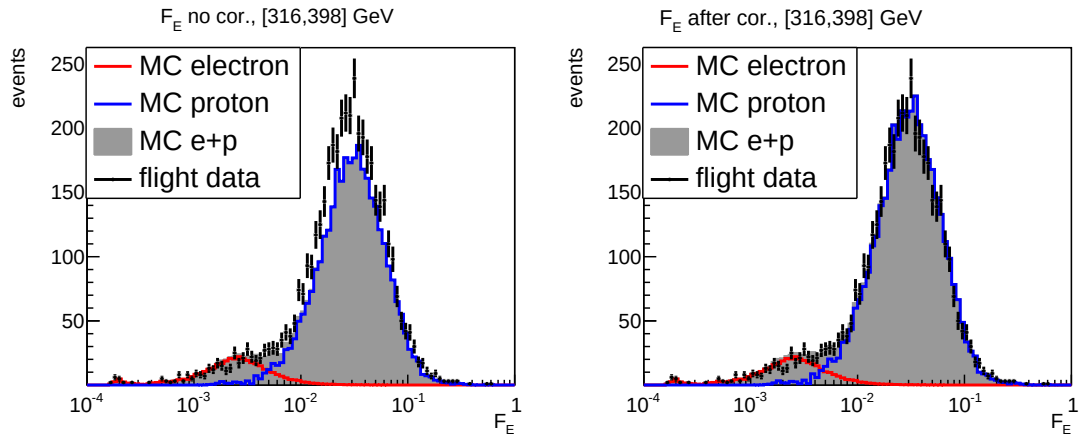

Figure 4.47. *Comparison between the flight data (black points) and the MC simulation of electrons (red histogram) and protons (blue histograms) based on GEANT4, regarding the F_E variable in the bin of reconstructed energy* $[316, 398]$ GeV. *The grey filled histograms are the sum of the electron and proton distributions obtained with the MC. The left panel shows the MC distributions without the W_C correction, the right panel shows the same distributions after this correction.*

Beside the MC re-weighting procedure, a further correction to the weight applied to the simulated protons is employed to increase the agreement between the simulated and the flight data. The number of protons surviving the pre-selection obtained with the simulations depends on the efficiency of the pre-selection for protons, which is very small especially below 100 GeV and it is affected by systematic errors related to the simulation of hadronic showers. It also depends on the parametrization of the proton flux used for the re-weighting procedure, which has an intrinsic uncertainty mainly due to the statistical and the systematic errors of the measured proton flux. This correction factor, here named *"post re-weight correction factor"* (W_C) is defined as follows:

$$W_C = \frac{\int_{10^{-2}}^{1} F_E^f(x)dx - \int_{10^{-2}}^{1} F_E^e(x)dx}{\int_{10^{-2}}^{1} F_E^s(x)dx},$$

where F_E^f is the distribution of the F_E obtained with the flight data, F_E^e is the one for simulated electrons after the re-weighting procedure and F_E^s is the sum of the F_E distributions obtained with the proton simulation and with the electron simulation after the re-weighting procedure. This correction factor depends on the energy thus this procedure is separately applied in each bin of reconstructed energy, obtaining a

value of W_C for each bin. The low limit of the integrals is 10^{-2} since above this value almost all the events are protons and the impact of $\int_{10^{-2}}^{1} F_E^e(x)dx$ is small, only a few percent in the high-energy region while it is negligible below 100 GeV. No post re-weight correction factor is applied to the electron simulations since the agreement between the number of events obtained with the re-weighted MC simulations and the flight data for electrons is acceptable. An example of the result of this procedure for the GEANT4 simulation is shown in fig. 4.47; this figure shows a comparison between the flight data and the proton and electron GEANT4 simulations before (left panel) and after (right panel) the application of the post re-weight correction factor: in this energy bin, i.e. $[316, 398]$ GeV, this correction factor is of order of 10%. For the GEANT4 simulation the correction factor is below 20% below 500 GeV, while it increases up to 50% in the TeV region. The EPICS simulation instead needs $W_C \sim -25\%$ in the entire energy range. The difference between the two simulations is mainly due to a difference in the efficiency of the CHD cut and the IMC-SC obtained with EPICS and GEANT4 protons. This discrepancy is partially expected since these cuts are strongly affected by the backscattered particles, as already mentioned in §4.6.5, where a discrepancy of $\sim 5\%$ between the CHD cut efficiency obtained with EPICS and GEANT4 for high-energy electrons is shown. The post re-weight correction factor, that is found to match the flight and the MC data, is used to correct the number of MC protons included in all the validation plots. It is also used to compute the best estimator of the residual proton contamination as described in §4.9.
A brief summary of the most important comparisons between MC and flight data is discussed in the following paragraphs, starting from simple variables, but mainly focusing on variables used for the proton rejection cut. A final comment about the comparison results, with an interpretation of the observed discrepancies between MC and flight data, is presented in the final paragraph of this section. The MC validation procedure involves numerous plots but here only few examples are shown.

Variables related to the tracking The first variables checked for the MC validation are related to the reconstructed track: the azimuthal and polar angles of the reconstructed track, the impact point of the reconstructed track on the top of the CHD, the number of missing points returned by the Kalman filter algorithm and the χ^2 of the reconstructed track. A reasonable agreement between the MC and the flight data about these variables is obtained with both EPICS and GEANT4 in the whole energy range, with only some small discrepancies about the number of missing points;

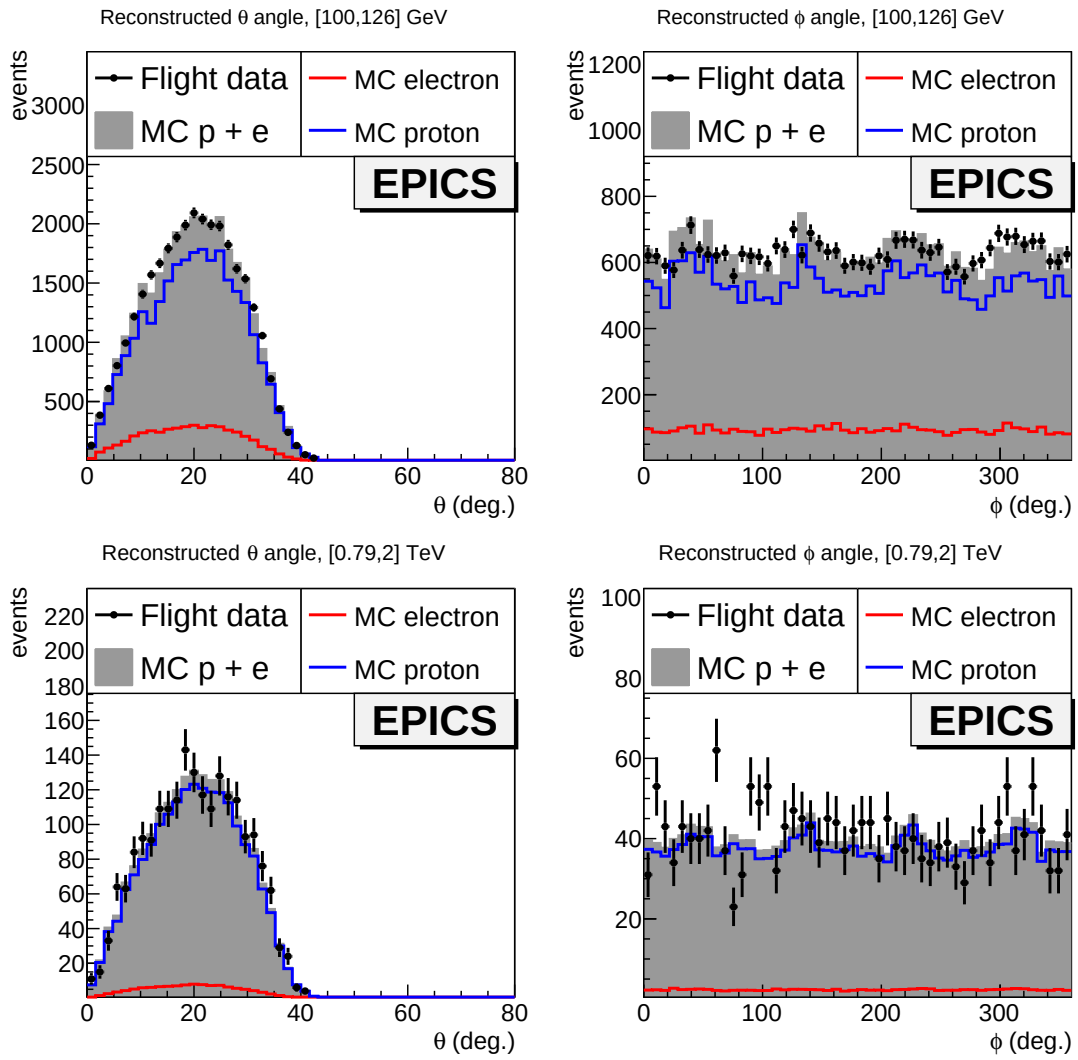

Figure 4.48. *Comparison between the flight data (black points) and the MC simulation of electrons (red histogram) and protons (blue histograms) based on EPICS, regarding the polar (θ, left panels) and the azimuthal (ϕ, right panels) reconstructed angles in the bin of reconstructed energy* $[100, 126]$ GeV *(top panels) and* $[0.79, 2]$ TeV *(bottom panels). The grey filled histograms are the sum of the electron and proton distributions obtained with the MC.*

the latter are probably due to the small fraction (less than 0.5%) of anomalous IMC channels which are not precisely replicated in the current MC digitization procedure. Two examples of the comparisons between the flight data and the EPICS simulation regarding the reconstructed angles in two bins of reconstructed energy are shown in fig. 4.48; a reasonable agreement is shown for these distributions.

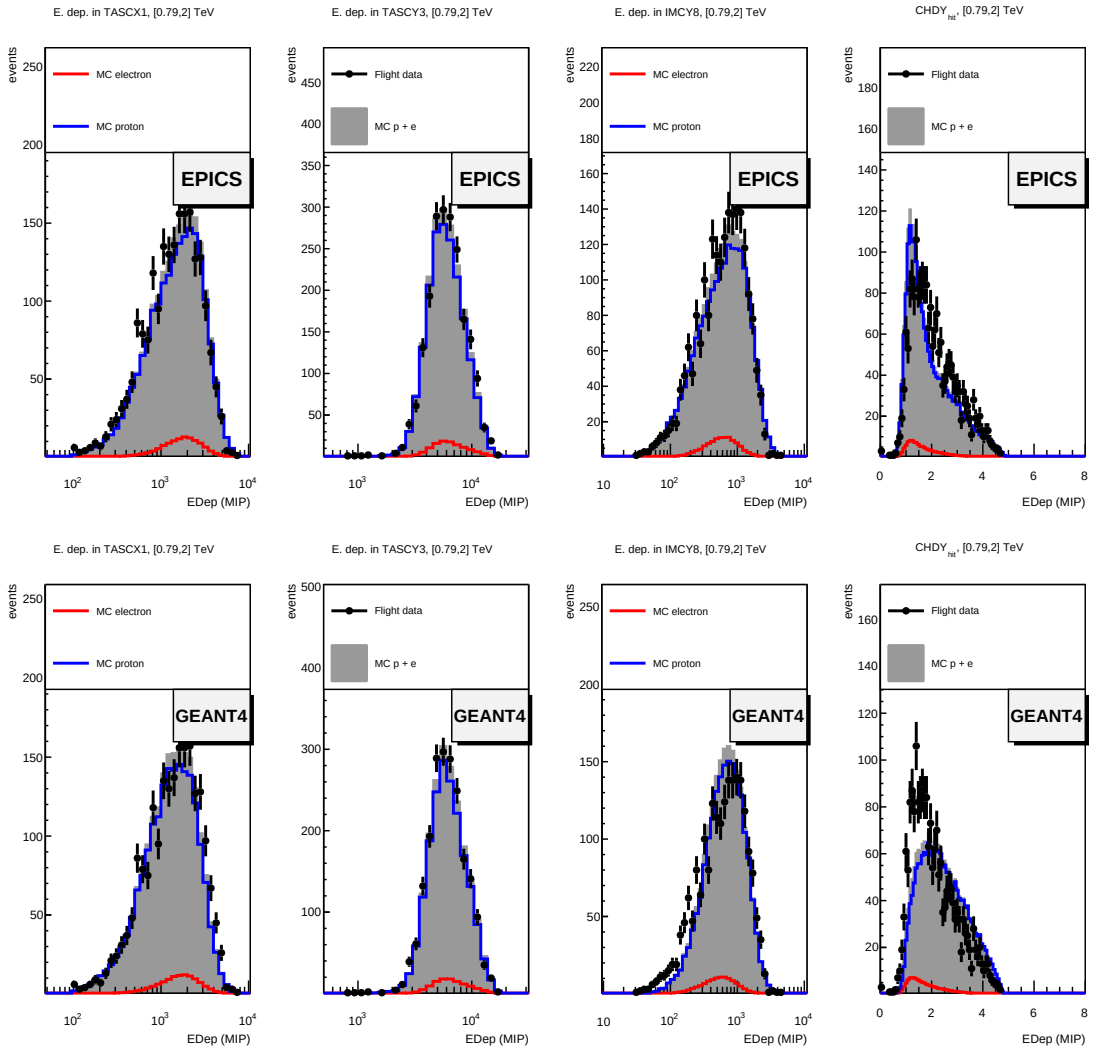

Figure 4.49. *Comparison between the flight data (black points) and the MC simulation of electrons (red histogram) and protons (blue histograms) based on EPICS (top panels) and GEANT4 (bottom panels), regarding the energy deposit in TASCX1 (first panel starting from the left), in the TASCY3 (second panel), in IMCY8 (third panel) and the $CHDY_{hit}$ variable (last panel) in the bin of reconstructed energy* $[0.79, 2]$ TeV*. The grey filled histograms are the sum of the electron and proton distributions obtained with the MC.*

Energy deposited in TASC, IMC and CHD The energy deposit in each layer of TASC, IMC and CHD is checked for the MC validation. The comparisons about energy deposit in TASC layers feature a reasonable agreement between the MC and flight data in the whole energy range with both GEANT4 and EPICS. Some discrepancies are present for the IMC layers with the GEANT4 simulation, especially above 100 GeV, while the EPICS simulation shows better results and no evident discrepancies are

found. The CHD energy deposit in each layer, and the variables involved in the CHD cut, i.e. $CHDX_{hit}$ and $CHDY_{hit}$, also show remarkable discrepancies with GEANT4: the comparisons with the EPICS simulation about these two variables feature small discrepancy in the TeV region, while the agreement is good in the low-energy region. Some examples of these validation plots obtained with EPICS in the TeV region for the energy deposit in TASCX1, TASCY3, IMCX8 and for $CHDY_{hit}$ are shown in the top panels of fig. 4.49, while the same plots obtained with GEANT4 are shown in the bottom panels of fig. 4.49.

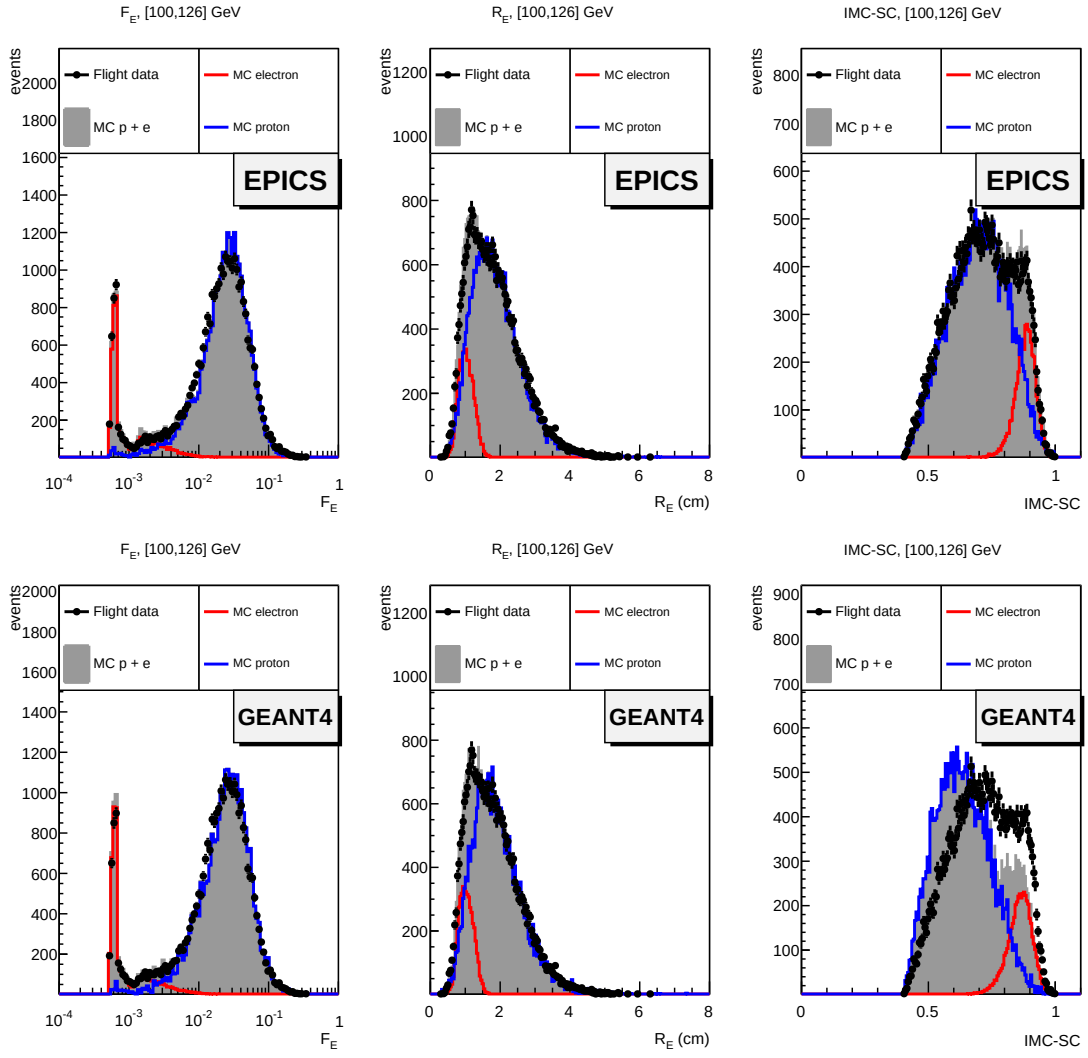

Figure 4.50. *Comparison between the flight data (black points) and the MC simulation of electrons (red histogram) and protons (blue histograms) based on EPICS (top panels) and GEANT4 (bottom panels), regarding the F_E (left panel), R_E (middle panel) and IMC-SC (right panel) in the bin of reconstructed energy* $[100, 126]$ GeV. *The grey filled histograms are the sum of the electron and proton distributions obtained with the MC.*

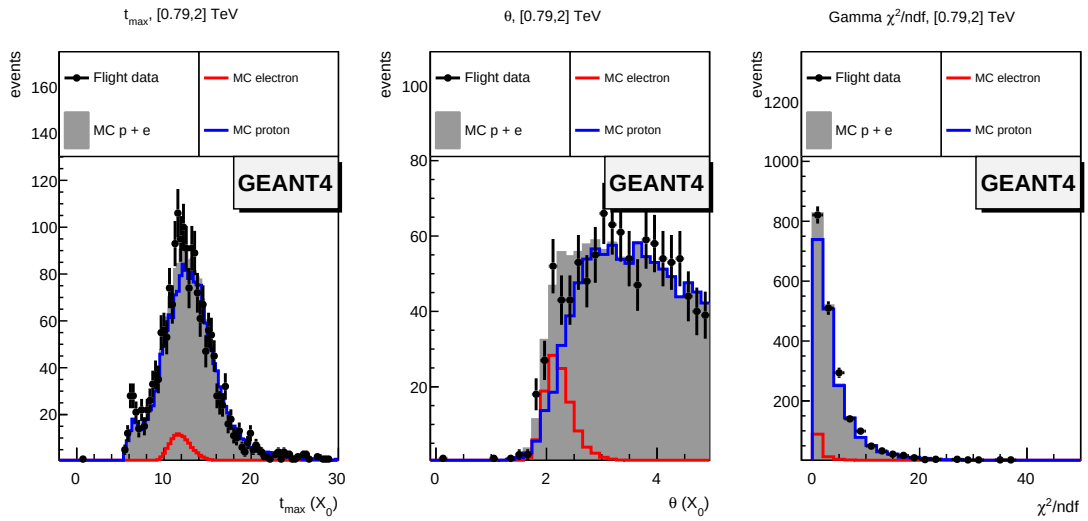

Figure 4.51. *Comparison between the flight data (black points) and the MC simulation of electrons (red histogram) and protons (blue histograms) based on GEANT4, regarding the t_{max} (left panel), θ (middle panel) and χ^2 (right panel) of the Gamma fit in the bin of reconstructed energy* $[0.79, 2]$ TeV. *The grey filled histograms are the sum of the electron and proton distributions obtained with the MC.*

e/p discrimination variables Comparisons about all the variables includes in the BDT analysis have been developed in order to validate the proton rejection cut. The main discriminating variables are F_E and R_E; the validation plots for these variables feature a good agreement with both GEANT4 and EPICS in the entire energy range, as shown in the left and middle panels of fig. 4.50. Another important variable for the rejection cut based on the MVA is the IMC-SC: this variable features a good agreement with the EPICS simulation below 500 GeV and some discrepancies above this energy: indeed this variable is not used for the MVA in the high-energy range. As expected from the previous comparison, the GEANT4 simulation shows considerable discrepancies regarding the IMC-SC in the whole energy range. The validation plots of this variable in the $[100, 126]$ GeV bin of reconstructed energy is shown in the right panels of fig. 4.50.

The variables related to the fit of the shower profile in the TASC show a good agreement between EPICS MC and flight data in the high-energy range, while below 500 GeV a small discrepancy about the distribution of the θ parameter is present; the latter is not involved in the MVA below 500 GeV. The same validation plots obtained with GEANT4 features instead a reasonable agreement in the whole energy range. An example of the validation plots obtained with GEANT4 in the high-energy range is

shown in fig. 4.51.

The validation of the variables related to the fit of the shower profile in the IMC features

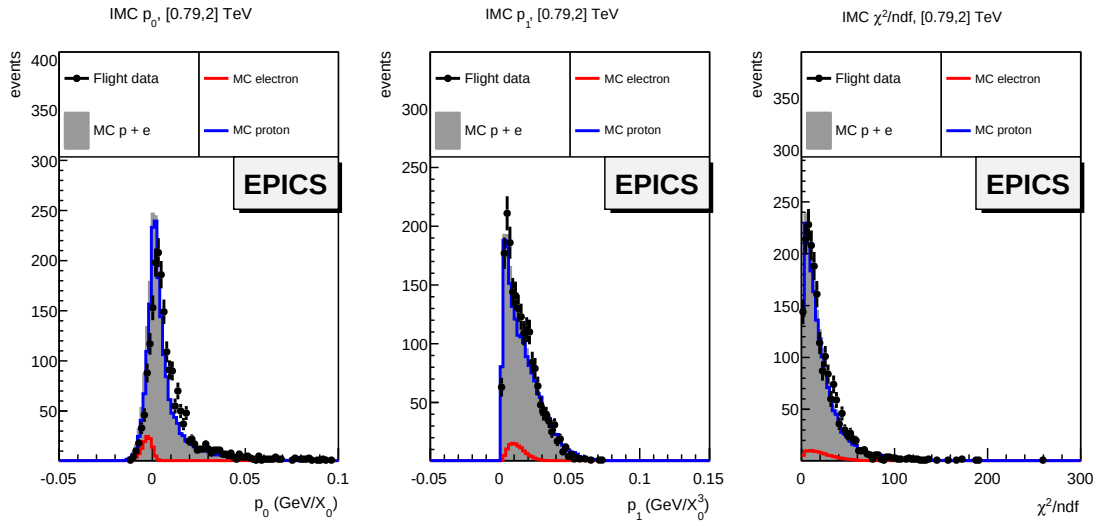

Figure 4.52. *Comparison between the flight data (black points) and the MC simulation of electrons (red histogram) and protons (blue histograms) based on GEANT4, regarding the p_0 (left panel), p_1 (middle panel) and chi^2 (right panel) of the IMC fit in the reconstructed energy* $[0.79, 2]$ TeV. *The grey filled histograms are the sum of the electron and proton distributions obtained with the MC.*

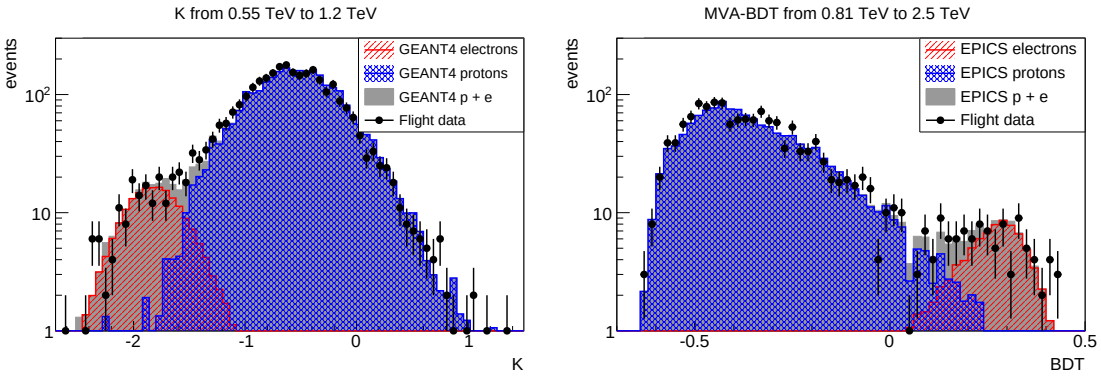

Figure 4.53. *Left panel: comparison between the flight data (black points) and the MC simulation of electrons (red histogram) and protons (blue histograms) based on GEANT4, regarding the K variables in the bin of reconstructed energy* $[0.55, 1.21]$ TeV. *The grey filled histograms are the sum of the electron and proton distributions obtained with the MC. Right panel: comparison obtained with EPICS regarding the BDT output in the reconstructed energy* $[0.81, 2.5]$ TeV.

a reasonable agreement between the EPICS simulation and the flight data in the entire energy range, while the GEANT4 simulation of these variables is less accurate, as expected from previous comparisons. An example obtained with the EPICS simulation

in the TeV energy range is shown in fig. 4.52.
Finally the distribution of the two variables, obtained with the K cut approach and the BDT algorithm, used alternatively for the electron/proton discrimination cut are also checked. A reasonable agreement between the MC and fight data are found with both GEANT4 and EPICS regarding the K cut distribution. Some discrepancies appear for the output variable of the BDT analysis with GEANT4, as expected from the results of the comparisons related to the IMC-SC and the shower fit in IMC. An example of this validation plot is shown in fig. 4.53 (these comparisons are also presented in [80]).

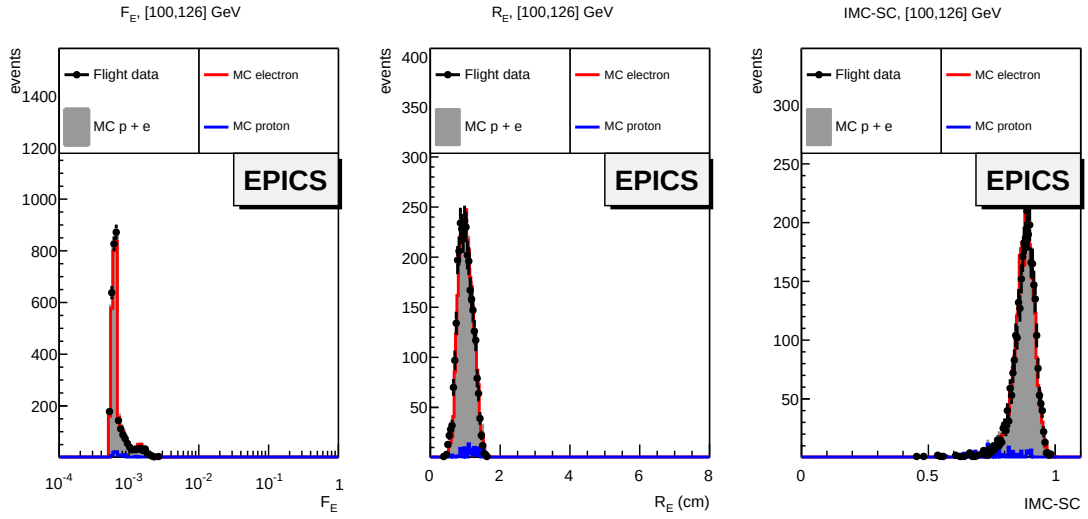

Figure 4.54. *Comparison between the flight data (black points) and the MC simulation of electrons (red histogram) and protons (blue histograms) based on EPICS, regarding the F_E (left panel), R_E (middle panel) and IMC-SC (right panel) in the bin of reconstructed energy* $[100, 126]$ GeV *after the K cut. The grey filled histograms are the sum of the electron and proton distributions obtained with the MC.*

Comparisons after the electron/proton cut The validation plots discussed in the previous paragraph are dominated by protons, since protons are considerably more abundant than electrons. In order to check the distribution of electrons, the validation plots are created again after the application of the K cut which selects the 70% of electrons, while it rejects protons as explained in §4.7.1. These comparisons feature consistent results with respect to the previous checks: the EPICS simulation features a good agreement for almost all the variables involved in this study with some discrepancies about the θ parameter of the Gamma fit already described. An example of these comparisons are shown in fig. 4.54.

Summary of MC validation The comparison between the MC and flight data features a good agreement about the variables related to the energy deposit in TASC and to the tracking algorithm with both EPICS and GEANT4. An overall good agreement is also found about the IMC and CHD variables involved in the electron analysis with EPICS, while GEANT4 features considerable discrepancies, which are probably due to an inaccurate simulation of the backscattered particles since these strongly affect the energy deposits in the IMC and CHD. The EPICS simulation also features some discrepancies for the CHD and IMC variables at high-energy (above 500 GeV), suggesting the fact that a proper simulation of backscattered particles at high-energy needs more accurate models. Furthermore, the validation plots for CHD and IMC suggest that EPICS produces slightly less backscattering with respect to flight data while GEANT4 generates too much backscattering. Because of these comparisons, the EPICS simulation is used as the reference simulation for the electron flux measurement. Indeed, the GEANT4 simulation is used for comparison: a systematic error in the electron flux computed by using the this simulation is expected, due to the disagreement between GEANT4 MC and flight data described in this section, see §4.9. In order to improve the agreement with the flight data, different models of the multiple scattering and the single scattering of particles with respect to the one employed in the current GEANT4 simulation will be investigated for the future CALET analysis.

4.9 Preliminary evaluation of systematic errors

In this section a preliminary evaluation of the systematic errors which affect the CALET electron flux measurement due to the above described discrepancies between MC and flight data is discussed: a more complete description of the total systematic error is discussed in §4.10. The evaluation method described here is based on the comparison of the electron flux measured with different techniques, e.g the electron fluxes computed by using the results of different MC simulations or using different electron/proton cuts. The reference flux for these comparisons is based on the MVA results obtained with the EPICS simulation. The value of this flux ($< \phi(E_i) >$) is calculated with eq. 4.5 described in §4.3 and it is also reported here:

$$< \phi(E_i) >= \frac{N(E_i) - N_{BG}(E_i)}{\Delta E_i \cdot G \cdot \Delta t \cdot \epsilon_{tot}(E_i)}$$

The value of $N(E_i)$ is the number of flight data events selected with the pre-selection and the BDT cut in the i-th bin of reconstructed energy. $N_{BG}(E_i)$ is equal to the number of surviving protons in the bin of reconstructed energy after pre-selection and the BDT cut obtained with the EPICS simulation (described in §4.7.2) multiplied by the post re-weight correction factor W_C obtained with the comparison between flight and EPICS MC data (described in §4.8). The total efficiency $\epsilon_{tot}(E_i)$ is approximated with a fit of eq. 4.10 to the total selection efficiency obtained with EPICS (as described in §4.7.2), computed at the centre of the bin. G is the geometrical factor of the acc. A equal to (415.7 ± 1.1) cm^{2}sr and the live time Δt is ~ 489 days.

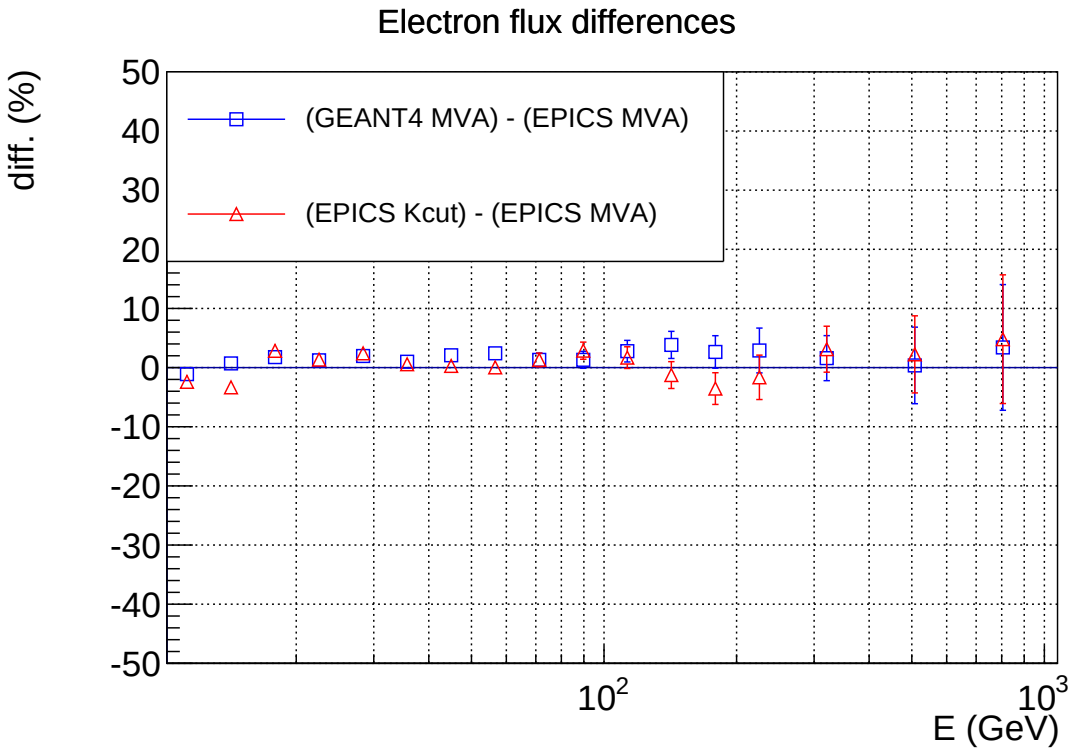

Figure 4.55. *The blue squares are the relative differences between the electron fluxes computed with the GEANT4 simulation by using the BDT cut and the reference flux (obtained with EPICS and the BDT cut). The red triangles are the relative differences between the electron flux computed with the EPICS simulation by using the K cut and the reference flux.*

The first comparison is between the reference flux, calculated with the EPICS simulation, and the one obtained with the GEANT4 simulations. For the latter, $\epsilon_{tot}(E)$ is the fit of the total efficiency obtained with the GEANT4 simulation, after the BDT cut, while $N_{BG}(E)$ is the surviving number of protons obtained with GEANT4 mul-

tiplied by the W_C factor obtained from the comparison between GEANT4 MC and flight data. The relative differences between this flux (named *"GEANT4 MVA"*) and the reference flux (named *"EPICS MVA"*) is shown in 4.55 (blue squares) below 1 TeV, since at higher energies the systematic error is sub-dominant with respect to the statistical one. The agreement between the two fluxes is reasonable in the whole energy range, with a maximum difference below 5%. As described in §4.8, for the variables related to the energy deposit in CHD and IMC the GEANT4 and EPICS simulations feature discrepancies with respect to the flight data which are in opposite directions (i.e. less backscattered particles in EPICS and too much backscattering in GEANT4); it is reasonable to assume the results of this comparison as a first rough estimation of the systematic error of the measurement due to the accuracy of the MC simulations. The error bars in the figure represent the statistical error of the GEANT4 MVA flux only.

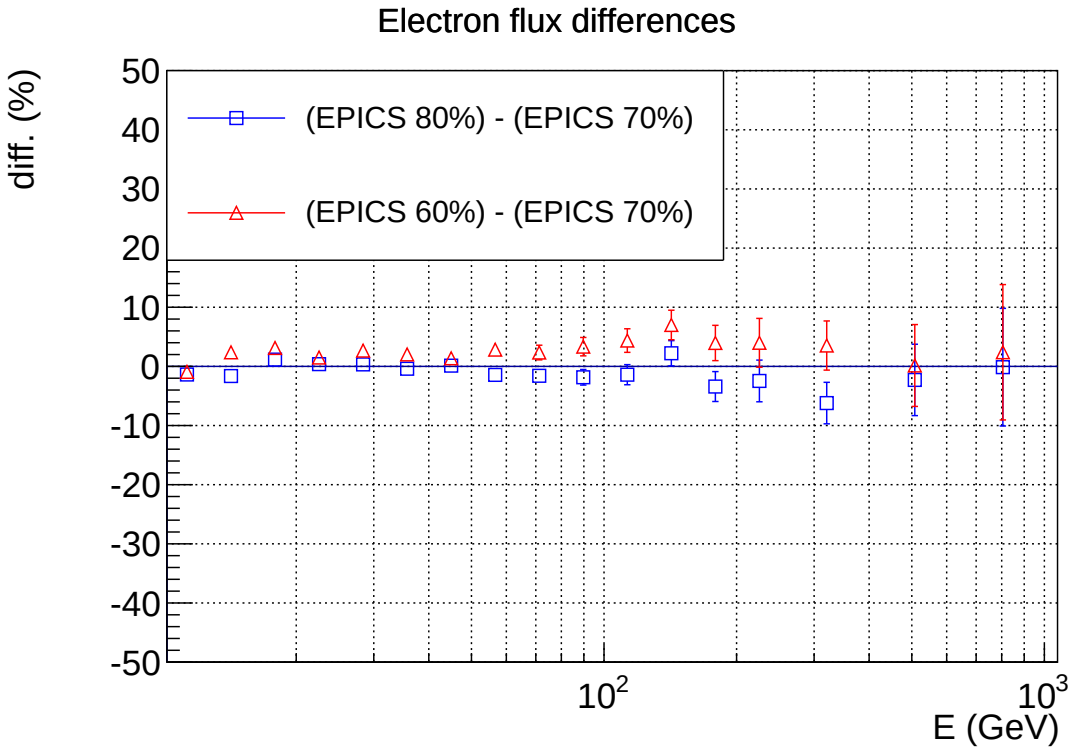

Figure 4.56. *Relative differences between the electron fluxes computed with the EPICS simulation by using the BDT cut corresponding to a constant efficiency of* 60% *and* 80% *and the reference flux (obtained with EPICS and the BDT cut corresponding to a constant efficiency of* 70%*).*

In order to check the stability of the rejection cut and of the accuracy of the

estimation of proton contamination two dedicated tests have been developed. The first one is the comparison between the flux obtained with EPICS using the K cut instead of the BDT cut (named *"EPICS Kcut"*) and the reference flux. The red triangles in fig. 4.55 show the result of this test: the maximum discrepancy is about 5%. The second check is based on the calculation of the electron flux by using BDT cuts corresponding to different electron selection efficiencies. The reference flux is calculated using a 70% efficiency for the proton rejection cut. Two other fluxes are calculated by using 80% and 60% efficiency cuts respectively. The results of these tests are shown in fig. 4.56. These tests feature a reasonable agreement between the tree fluxes, with differences of the order of 5%. Both the results about the stability of the rejection cut show that an approximated value of the systematic error related to the rejection cut, due to the limited accuracy of the EPICS simulation, is $\sim 5\%$. A more accurate evaluation of the stability of the BDT cut is discussed in the following section.

4.10 First measurement of the electron flux

The first measurement of the electron flux with the CALET experiment is described in the paper [88], accepted by "Physical Review Letters" (PRL) in the first days of October 2017 and currently in press. The paper is expected to be published in the first days of November 2017. During the drafting of this thesis, the final version of the data analysis used for the electron flux measurement has been completed. The latter exploits the studies described in this thesis, especially the comparisons among different MC simulations, which are used for the evaluation of the systematic error of the electron measurement, as described at the end of this section. The efforts of the entire CALET collaboration have led to an analysis procedure (hereafter, the "article analysis") slightly different with respect to the analysis developed during this Ph.D. work. In this section a brief summary of the content of the article accepted by PRL is presented, focusing on the main differences of article analysis with respect to the one described in this thesis. Furthermore, other important items, e.g the evaluation of the systematic errors, is discussed too, while a more complete description of the article analysis and the final result is given in [88].

The flight data analysed used in the article analysis are collected with the HET in 627 days, from October 13, 2015 to June 30, 2017. The total live time of the measurement is about ~ 526 days. The MC simulations involved in the analysis are the same

used for this thesis (see §4.2).
In order to increase the number of observed electrons and decrease the statistical error, especially in the high-energy range, the used acceptance region is A+B, corresponding to a geometrical factor of (570.3 ± 1.3) cm^{2}sr (see §4.1). The performance of the detector is very similar to the one obtained with the acc. A only, with differences below 1% for the selection efficiency, the energy resolution and the residual proton contamination obtained with the MC simulations.
The tracking algorithm used in this analysis, named *"ElectroMagnetic shower tracking"* (EM track), is different from the Kalman filter algorithm used in this thesis and it is specifically designed for tracking electrons [89], while it is not optimized for protons and nuclei. The Kalman filter algorithm is used instead for comparison as described below.
The algorithm for energy reconstruction is the same described in this thesis, see §4.5. The absolute energy scale depends on the calibration of the detector calibrated with MIPs; this calibration is commonly checked in space experiments by analysis of the geomagnetic cut-off energy [90]. For this study, data samples obtained with the LET are selected inside an interval of the McIlwain L parameter [22] of $[0.95, 1.25]$. By dividing the interval of L into three bins: $[0.95, 1.00]$, $[1.00, 1.14]$ and $[1.14, 1.25]$, different rigidity cut-off regions are selected corresponding to $\sim$ 15 GV, $\sim$ 13 GV and $\sim$ 11 GV respectively. The cut-off energy is calculated by using the trajectory tracing code ATMNC3 [91] and the International Geomagnetic Reference Field, IGRF-12 [92]. It is found that the average ratio of the expected to measured cut-off position in the electron flux is 1.035 ± 0.009 (stat.). As a result, a correction of the energy scale by 3.5% was implemented in the analysis.

The pre-selection applied before the rejection cut that has been developed by the CALET collaboration for the article analysis is very similar to the one studied during this Ph.D. work:

- the software high energy trigger (SW-HET) is the same of the one described in §4.6.1,
- the IMC shower concentration (IMC-SC) is the same of the one described in §4.6.4,
- the consistency check of the reconstructed EM track with the development of the TASC shower (TASC-C) is applied but using only the first layer of the TASC.

- the charge cut is the CHD cut described in §4.6.4.

The total efficiency of the pre-selection of the final version of the analysis is very similar to the one described in §4.7, with difference of only few percent below 50 GeV and smaller above.

About electron/proton discrimination, the analysis employed the same cuts used for this thesis (K cut and BDT, see below) complemented by an additional cut which requires a shower developments in TASC consistent with those of electrons. The variable used for this selection is derived from a log-likelihood function (L_{TASC}) built from the probability distribution of electron showers in TASC, calculated as follows:

$$L_{TASC} = \frac{1}{n_{TASC}} \sum_{i=1}^{n_{TASC}} (\ln p_i^{TASC} - \ln < p_i^{TASC} >),$$

where $n_{TASC} = 12$ is the number of TASC layers, p_i^{TASC} is the probability of observing the measured energy deposit in i-th layer obtained with EPICS electron simulations and $< p_i^{TASC} >$ denotes the expectation value of p_i. This cut slightly increases the proton rejection power, especially in the low-energy range, and it further reduces the acceptance contamination. Another similar cut (L_{IMC}), based on a log likelihood functions about the energy deposit in the IMC, and calculated with the same formula of L_{TASC}, is also used. These cuts reject events with $L_{TASC} < -1$ and $L_{IMC} < -3$, and the combined efficiency for electrons of these two cuts is higher than 95% in the entire energy range.

Besides the log-likelihood cuts, the rejection cuts used in this analysis are the K cut, described in §4.7.1, and an updated version of the BDT cut, very similar to the one developed during this Ph.D. work. With respect to the MVA described in §4.7.2, a parameter named $t_{5\%}$ is added to the algorithm: $t_{5\%}$ is the depth (in units of X_0) of the shower in TASC corresponding to the 5%-quantile of the fitted gamma function (eq. 4.8). The residual proton contamination obtained with the final version of the BDT analysis is consistent with the one derived in §4.7.2.
For the flux measurement, in order to maximize the rejection power against the abundant protons, the MVA has been used above 500 GeV, while the K cut was used below 500 GeV since in this energy range it features a good rejection power and a more complex analysis is not needed. The thresholds of the K and BDT cuts are selected

in order to obtain a constant efficiency of this selection of 80%, in order to increase the number of observed electrons with respect to the selections corresponding to 70% efficiency used as references in this thesis. The residual proton contamination obtained with EPICS after the pre-selection and the rejection cuts (log-likelihood and alternatively K cut or BDT) is $\sim 5\%$ up to 1 TeV and $10\% \div 15\%$ in $1 \div 3$ TeV region.

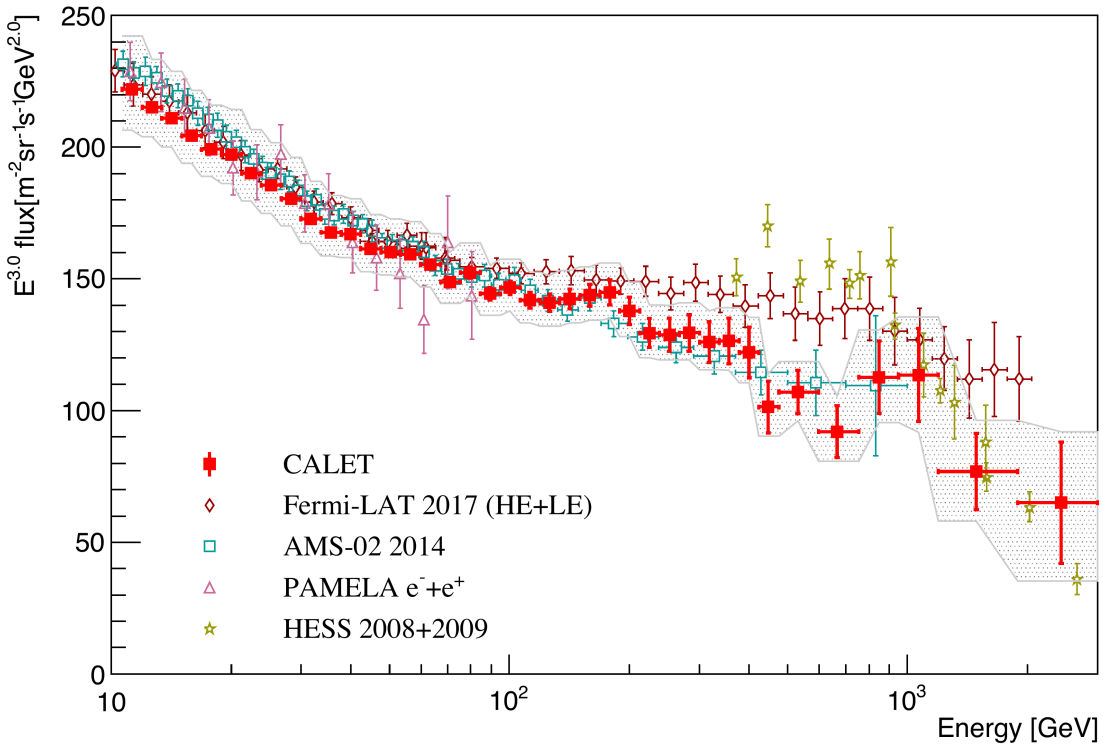

Figure 4.57. *CR electron spectrum measured by CALET [88] from* 10 GeV *to* 3 TeV*, where systematic errors (not including the uncertainty on the energy scale) are drawn as a grey band. Other measurements in space [40][41][93] and from ground based experiments [42] are also plotted.*

The electron+positron spectrum measured by CALET, calculated with the eq. 4.5, is shown in fig. 4.57 (red squares). The present analysis is limited to almost fully-contained events, rejecting events inside acc. C and D, thus only 55% of the full CALET acceptance is involved. The presented flux is fairly consistent with AMS-02 [41], although it is lower than the recent Fermi-LAT result [40] above a few hundred GeV. The spectrum can be fitted with a single power-law with spectral index -3.152 ± 0.016 above 30 GeV. The structures at the highest energies are within the (stat. + syst.) errors and therefore no conclusion can be drawn at the moment about their significance.

The main sources of systematic uncertainties include both energy-dependent and -independent uncertainties. The evaluation of the systematic error follows the procedure described in §4.9 based on the comparison of the value of the electron flux computed with different analysis techniques or data samples. A brief description of the most important sources of the systematic error is reported below in this section while a more accurate description of this item is presented in the supplementing material of the incoming publication [88].

The energy-independent uncertainties affect the absolute normalization of the flux and are mainly due to the geometrical factor, the live time measurement, and the long-term stability of the detector.
The geometrical factor, measured by using the EPICS MC simulation with the procedure described in §4.1, is only related to the detector geometry which was accurately measured on the ground, thus the systematic error due to the accuracy of the geometrical factor measurement is negligibly small.
To confirm the long-term stability of detector sensitivity, spectrum stability was investigated by dividing the whole observation period into 4 equal sub-periods and comparing the electron spectra obtained in these periods. For each energy bin in the $[20, 100]$ GeV interval, the differences between the reference and the test fluxes are computed (4 values per bin). The distribution of these $4 \times N_{bins}$ differences is centred around 0 and has a standard deviation of about 1.4%. This number is mostly consistent with pure statistical fluctuation but a systematic uncertainty of 1.4% is conservatively associated with the long-term stability. A similar approach is used to evaluate the systematic error related to the live time: the whole data-set is divided into 4 sub-samples corresponding to events with live time fractions (defined as the cumulative live time divided by the total observation time) larger than 0.88, 0.72–0.88, 0.60–0.72 and less than 0.60. A standard deviation of 3.4% is found. This factor is larger than the expected one, estimated with ground tests of the CALET electronics and logics, and it could be due to the fact that in the 4 data-sets the contiguous time intervals selected are not much larger than dead time sampling interval of 1 sec. As described in §4.4, in such a case, the first and last events in the time interval introduce an approximation error, which is not present in the regular flux. Therefore, a systematic uncertainty of 3.4% is comfortably conservative.

The energy dependent systematic errors are mainly related to the MC simulation

of the event selection efficiencies and of the electron/proton discrimination. In order to estimate the tracking-related systematics, for example, the difference between electron spectra obtained using the EM track and the Kalman filter tacking is computed. This difference remains below 5% in almost all the energy bins. The systematics related to the pre-selection are checked by calculating the electron flux using different thresholds for these selections; e.g. one spectrum is computed without applying the IMC-SC cut, and another one using a more strict IMC-SC selection than the standard procedure, and a good consistency among the fluxes is found. Using this approach, the systematic errors associated to each cut used in the pre-selection are evaluated. The quadratic sum of these uncertainties is considered the total systematic error associated to the pre-selection and it is below 5% in almost all the bins.

The electron/proton identification cut is the most important source of systematics. To address the uncertainty in the BDT analysis, 100 independent training+test data set pairs were created and the stability of the resulting flux was checked in each energy bin by changing the electron efficiency from 70% to 90% in 1% steps for the test sample corresponding to each training set. The stability of the BDT analysis is shown in the top panel of fig. 4.59: for each energy bin, the values of the mean and of the standard deviation of the distribution of the electron fluxes are obtained. The value of these parameters in each energy bin is shown in fig. 4.59. Two other important checks, already explained in §4.9, are the comparison of the reference flux with the flux obtained with the GEANT4 simulation and with a different rejection cut. The results of these checks are shown in fig. 4.60: these results are compatible with the preliminary results shown in fig. 4.55, since the differences below 1 TeV are of order of 5%. Above this energy the difference between the electron flux computed with GEANT4 with respect the one obtained with EPICS is larger, reaching 25% at 3 TeV: as expected by the comparison shown in §4.7, the pre-selection efficiency and the residual proton contamination above 1 TeV obtained with EPICS and GEANT4 feature larger discrepancies with increasing energy. The relative differences shown in fig. 4.60 are fitted with a 7th-order log-polynomial to avoid too much statistical fluctuations while preserving possible energy dependent structures.

The total systematic error shown as a grey band in fig. 4.57 is computed as the quadratic sum of all the systematic errors described above: all the energy-dependent sources of systematic errors are individually fitted with log-polynomial functions, and

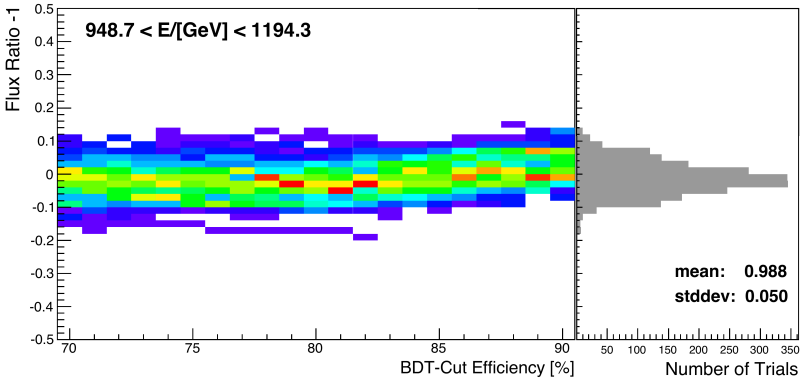

Figure 4.58. *Stability of BDT analysis with respect to independent training samples and BDT-cut efficiency in the* $[949, 1194]$ GeV *bin [88]. Colour maps show the flux ratio dependence on efficiency, where the bin value (number of trials) increases as colour changes from violet, blue, green, yellow to red. A projection onto the Y -axis is shown as a rotated histogram (in grey colour).*

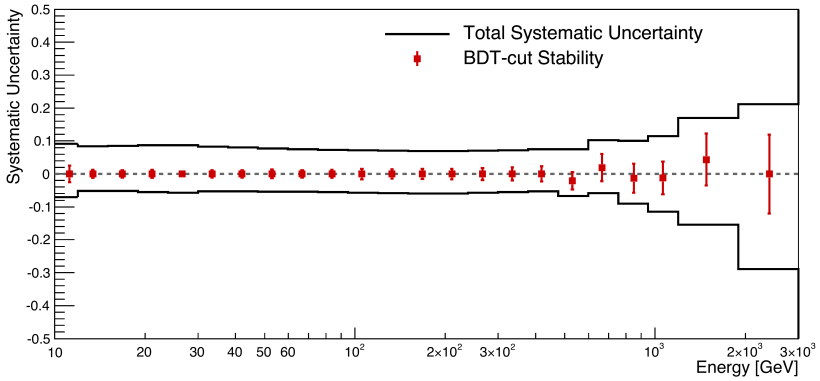

Figure 4.59. *Energy dependence of systematic uncertainties related to the BDT stability [88]. The red squares represent the mean of the fluxes obtained with the different training samples at different BDT selection efficiencies while the red bars are the standard deviation. Since the K cut is used below* 500 GeV *for the calculation of the final flux, the centre value is set to zero for these energy bins. The bands defined by black lines show the sum in quadrature of all the sources of systematics, except the energy scale uncertainties.*

the values of these functions in each energy bin are used for this calculation. The only source of systematics not included in this sum is the uncertainty related to the absolute energy scale. The energy scale determined with a study of the rigidity cut-off is $(3.5 \pm 0.9)\%$ (stat.) higher than that obtained with MIP calibrations. As the two methods are totally independent, the causes of this difference have to be further investigated to clarify their contribution to the systematic error on the energy scale. For this reason, this uncertainty is not included in the present analysis and this issue will be addressed by further studies.

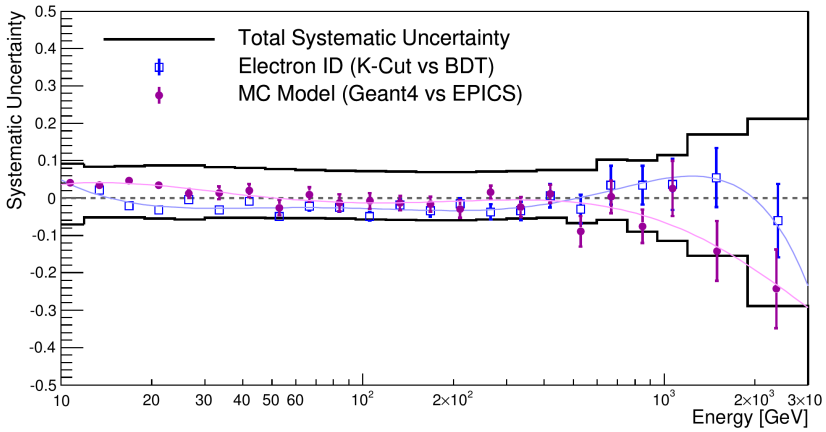

Figure 4.60. *Energy dependence of systematic uncertainties in electron identification methods (K cut vs BDT cut) and MC models (GEANT4 vs EPICS), which are fitted with 7th-order log-polynomial [88]. Note that uncertainties in electron identification are estimated by (BDT - K cut) below* 500 GeV *and (K cut - BDT) above.*

The published CALET electron+positron spectrum is summarized in the following table. The first and second errors represent the statistical uncertainties (68% confidence level) and systematic uncertainties, respectively.

Energy Bin (GeV)	Mean Energy (GeV)	Flux ($m^{-2}sr^{-1}s^{-1}GeV^{-1}$)
10.6–11.9	11.3	$(1.546 \pm 0.005\,^{+0.117}_{-0.108}) \times 10^{-1}$
11.9–13.4	12.6	$(1.065 \pm 0.004\,^{+0.072}_{-0.055}) \times 10^{-1}$
13.4–15.0	14.2	$(7.404 \pm 0.026\,^{+0.500}_{-0.383}) \times 10^{-2}$
15.0–16.9	15.9	$(5.073 \pm 0.020\,^{+0.344}_{-0.261}) \times 10^{-2}$
16.9–18.9	17.8	$(3.504 \pm 0.015\,^{+0.238}_{-0.180}) \times 10^{-2}$
18.9–21.2	20.0	$(2.457 \pm 0.012\,^{+0.174}_{-0.136}) \times 10^{-2}$
21.2–23.8	22.5	$(1.679 \pm 0.009\,^{+0.119}_{-0.093}) \times 10^{-2}$
23.8–26.7	25.2	$(1.159 \pm 0.007\,^{+0.082}_{-0.066}) \times 10^{-2}$
26.7–30.0	28.3	$(7.988 \pm 0.037\,^{+0.568}_{-0.457}) \times 10^{-3}$
30.0–33.7	31.7	$(5.411 \pm 0.029\,^{+0.354}_{-0.287}) \times 10^{-3}$
33.7–37.8	35.6	$(3.715 \pm 0.023\,^{+0.243}_{-0.197}) \times 10^{-3}$
37.8–42.4	39.9	$(2.620 \pm 0.018\,^{+0.163}_{-0.139}) \times 10^{-3}$
42.4–47.5	44.8	$(1.794 \pm 0.014\,^{+0.111}_{-0.095}) \times 10^{-3}$
47.5–53.3	50.3	$(1.261 \pm 0.011\,^{+0.075}_{-0.067}) \times 10^{-3}$
53.3–59.9	56.4	$(8.883 \pm 0.087\,^{+0.525}_{-0.475}) \times 10^{-4}$
59.9–67.2	63.3	$(6.129 \pm 0.068\,^{+0.338}_{-0.328}) \times 10^{-4}$
67.2–75.4	71.0	$(4.162 \pm 0.053\,^{+0.230}_{-0.223}) \times 10^{-4}$
75.4–84.6	79.7	$(3.009 \pm 0.043\,^{+0.158}_{-0.166}) \times 10^{-4}$
84.6–94.9	89.4	$(2.023 \pm 0.033\,^{+0.106}_{-0.111}) \times 10^{-4}$
94.9–106.4	100.4	$(1.45 \pm 0.03\,^{+0.07}_{-0.08}) \times 10^{-4}$
106.4–119.4	112.6	$(9.94 \pm 0.21\,^{+0.51}_{-0.57}) \times 10^{-5}$
119.4–134.0	126.3	$(7.00 \pm 0.16\,^{+0.34}_{-0.41}) \times 10^{-5}$
134.0–150.4	141.8	$(4.99 \pm 0.13\,^{+0.25}_{-0.29}) \times 10^{-5}$
150.4–168.7	159.1	$(3.57 \pm 0.10\,^{+0.17}_{-0.21}) \times 10^{-5}$
168.7–189.3	178.8	$(2.53 \pm 0.08\,^{+0.12}_{-0.15}) \times 10^{-5}$
189.3–212.4	200.1	$(1.72 \pm 0.06\,^{+0.08}_{-0.10}) \times 10^{-5}$
212.4–238.3	224.5	$(1.14 \pm 0.05\,^{+0.05}_{-0.07}) \times 10^{-5}$
238.3–267.4	252.4	$(8.01 \pm 0.39\,^{+0.39}_{-0.46}) \times 10^{-6}$
267.4–300.0	282.9	$(5.72 \pm 0.31\,^{+0.28}_{-0.33}) \times 10^{-6}$
300.0–336.6	317.6	$(3.93 \pm 0.24\,^{+0.20}_{-0.22}) \times 10^{-6}$
336.6–377.7	355.9	$(2.80 \pm 0.19\,^{+0.15}_{-0.15}) \times 10^{-6}$
377.7–423.8	400.3	$(1.90 \pm 0.15\,^{+0.11}_{-0.10}) \times 10^{-6}$
423.8–475.5	446.7	$(1.14 \pm 0.11\,^{+0.06}_{-0.06}) \times 10^{-6}$
475.5–598.6	530.3	$(7.18 \pm 0.56\,^{+0.40}_{-0.48}) \times 10^{-7}$
598.6–753.6	665.1	$(3.13 \pm 0.33\,^{+0.28}_{-0.18}) \times 10^{-7}$
753.6–948.7	848.8	$(1.84 \pm 0.23\,^{+0.16}_{-0.16}) \times 10^{-7}$
948.7–1194.3	1065.4	$(9.39 \pm 1.46\,^{+0.92}_{-1.04}) \times 10^{-8}$
1194.3–1892.9	1489.2	$(2.33 \pm 0.44\,^{+0.36}_{-0.34}) \times 10^{-8}$
1892.9–3000.0	2432.8	$(4.51 \pm 1.60\,^{+0.89}_{-1.28}) \times 10^{-9}$

Conclusion

The results about CALET MC comparison obtained in this thesis work show that a reasonable agreement among the three simulations about the energy deposited and the shower profile in TASC. A reasonable agreement regarding the energy deposit in IMC and CHD between GEANT4 and FLUKA is also found, while there are significant differences between GEANT4 (FLUKA) and EPICS, more and more pronounced as the primary particle energy increases. To exclude the possibility to ascribe them to differences in the implementation of the CALETCAD in GEANT4 and FLUKA with respect to EPICS, the same comparisons were done with the same simulation package but using a simplified geometry. The analysis with the simplified geometry confirms a reasonable agreement of the 3 MC simulations for the TASC benchmarks and it also shows the same discrepancies in IMC and CHD obtained with the CALETCAD. These discrepancies are probably due to a different treatment of the backscattered particles coming from TASC in EPICS with respect to GEANT4 and FLUKA; this hypothesis was investigated with EPICS, FLUKA and GEANT4 by using the CALETCAD geometry without the TASC. This avoids the production of most of the backscattered particles and indeed a good agreement among the 3 simulations is found.

The algorithm for the reconstruction of the kinetic energy of electrons starting from the energy deposits in TASC+IMC, was developed by using both EPICS and GEANT4; the performance of this method is sufficient for the CALET measurement and a good agreement among the two MC simulations is found. The pre-selection, designed to select $\mid Z \mid = 1$ particles inside the acc. A, from 10 GeV to 3 TeV, and to avoid contamination due to out-of-acceptance events and nuclei, achieves a high efficiency ($> 90\%$) for electrons. These selection cuts are mainly based on the reconstructed track with the Kalman filter technique. The efficiency of the pre-selection obtained

with GEANT4 and EPICS is consistent below 1 TeV while some discrepancies of order of 5% are present at high-energy.
Since the main background for the electron spectrum measurement are protons, a strong proton rejection cut is needed. Two different techniques were discussed: the first one based on a selection (named K cut) involving a single discriminating variable, and a second approach based on a Multi Variate Analysis (MVA) algorithm. The K cut is based on a variable obtained from the development of the shower in the TASC, considering both the longitudinal and lateral profiles. This cut is able to properly discriminate electrons and protons below 1 TeV, with a residual proton contamination below 10%. To improve the e/p discrimination up to the multi-TeV region, a MVA using the Boosted Decision Trees (BDT) was adopted. This analysis includes 9 discriminating variables and features a contamination below 10% up to 3 TeV; a reasonable agreement between the residual contamination obtained with GEANT4 and EPICS is also found, with significant discrepancies (of order of 10%) above 1 TeV.
A preliminary validation of the MC simulation, based on comparisons between MC and flight data about distributions of meaningful variables, features a good agreement regarding the energy deposit in TASC and to the tracking method with both EPICS and GEANT4, while GEANT4 features considerable discrepancies with respect to the flight data regarding the energy deposit in IMC and CHD probably due to a non-realistic simulation of the backscattered particles. The EPICS simulation also features some discrepancy for the CHD and IMC variables at high-energy (above 500 GeV).
The discussed preliminary evaluation of the systematic errors, which affect the CALET electron flux measurement due to the discrepancy between MC and flight data, is based on the comparison of the electron fluxes obtained with different techniques. The comparison between the results obtained with EPICS and GEANT4 feature a reasonable agreement, by taking into account the described discrepancies between GEANT4 and EPICS, with differences below 5%. Similar results were obtained comparing the electron fluxes computed with the BDT at different selection efficiencies and the K cut.

The final version of the analysis for the electron measurement, completed during the drafting of this thesis, described in details in a paper accepted for publication by PRL, and currently in press, has some slight differences with respect the one presented in this thesis. The most important features, such as the residual proton contamination and the selection efficiency, are almost consistent with the ones discussed in this thesis. The measured electron flux is fairly in agreement with the measurement by AMS-02,

although it is lower than the recent Fermi-LAT result above a few hundred GeV. The estimated systematic error is quite large, of order of 8% below 1 TeV, and it is mainly due to the discussed discrepancies between the two MC codes. This will be reduced in future analysis by addressing the present discrepancies observed between MC and flight data, e.g. by employing different scattering models in GEANT4 to reduce the discrepancies about the backscattered particles. Furthermore, thanks to the next 3 years of observation, the increasing statistics will allow the extension of the CALET electron observation above 3 TeV.

Bibliography

[1] J. Beringer et al. (Particle Data Group)
Review of Particle Physics, Phys. Rev. D 86, 010001
http://pdg.lbl.gov

[2] E. Margaret Burbidge, G. R. Burbidge, William A. Fowler, and F. Hoyle
Synthesis of the Elements in Stars
Rev. Mod. Phys. 29, 547 (1957)

[3] O. Adriani et al.
Time dependence of the proton flux measured by PAMELA during the July 2006 - December 2009 solar minimum.
The Astrophysical Journal, 765:91 (8pp), 2013 March 10

[4] Jörg R.Hörandel
On the knee in the energy spectrum of cosmic rays
Astroparticle Physics Volume 19, Issue 2, May 2003, Pages 193-220

[5] K. Greisen.
End to the Cosmic-Ray Spectrum?
Phys. Rev. Lett., 16:748–750, 1966.

[6] G. T. Zatsepin and V. A. Kuzmin.
Upper Limit of the Spectrum of Cosmic Rays.
Soviet Journal of Experimental and Theoretical Physics Letters, 4:78–80, 1966

[7] Pasquale Blasi.
The origin of galactic cosmic rays.
Astron Astrophys Rev (2013) 21:70, DOI 10.1007/s00159-013-0070-7

[8] B. Wiebel-Sooth, P.L. Biermann, H. Meyer.
Cosmic rays. VII. individual element spectra: prediction and data.
Astron. Astrophys. 330, 389–398 (1998)

[9] E. Fermi.
On the Origin of the Cosmic Radiation.
Phys. Rev. 75, 1169, 15 April 1949

[10] E. Fermi.
Galactic magnetic fields and the origin of cosmic radiation.
Astrophys. J. 119, 1–6 (1954)

[11] Maurizio Spurio.
Particles and Astrophysics, A Multi-Messenger Approach.
Astrophysics. Astronomy and Astrophysics Library. Springer, Cham, https://doi.org/10.1007/978-3-319-08051-2˙3

[12] A. R. Bell.
The acceleration of cosmic rays in shock fronts.
Mon. Not. Roy. Astron. Soc. 182, 147-156 (1978).

[13] Pasquale Blasi, Elena Amato, Damiano Caprioli.
The maximum momentum of particles accelerated at cosmic ray modified shocks.
Mon Not R Astron Soc (2007) 375 (4): 1471-1478.

[14] P.O. Lagage and C.J. Cesarsky.
The maximum energy of cosmic rays accelerated by supernova shocks.
Astron. Astrophys. 125 249–257, 1983

[15] Katia M. Ferriére
The interstellar environment of our galaxy
Rev. Mod. Phys. 73, 1031

[16] M.S. Longair
High Energy Astrophys., 3rd edn.
Cambridge University Press, Cambridge, 2011, ISBN: 978-0521756181

[17] A. W. Strong, I. V. Moskalenko
Propagation of cosmic-ray nucleons in the Galaxy
Astrophys.J.509:212-228,1998

[18] A. Obermeier, P. Boyle, J.Hörandel and D.Müller
The Boron-Carbon abundance ratio and Galactic propagation of Cosmic Radiation
The Astrophysical Journal, 752:69 (7pp), 2012 June 10, doi: 10.1088/0004-637X/752/1/69

[19] N. E. Yanasak et al.
Measurement of the secondary radionuclides
Astrophys. J. 563:768 (2001).

[20] T. Kobayashi et al.
The most likely sources of high-energy cosmic ray electrons in SuperNova Remnants
The Astrophysical Journal, 601:340–351, 2004 January 20

[21] C. Störmer
The Polar Aurora.
Clarendon Press, Oxford, 1955.

[22] D.F. Smart, M.A. Shea
A review of geomagnetic cutoff rigidities for earth-orbiting spacecraft
Advances in Space Research 36 (2005) 2012–2020

[23] M. J. Owens, R. J. Forsyth
The Heliospheric Magnetic Field
Living Rev. Solar Phys., 10, (2013), 5, doi:10.12942/lrsp-2013-5

[24] J. A. Simpson
The cosmic ray nucleonic component: the invention and scientific uses of the neutron monitor
Space Science Reviews, July 2000, Volume 93, Issue 1–2, pp 11–32.

[25] M. S. Potgieter, E. E. Vos, M. Boezio, N. De Simone, V. Di Felice, V. Formato
Modulation of Galactic Protons in the Heliosphere During the Unusual Solar Minimum of 2006 to 2009.
Solar Physics, January 2014, Volume 289, Issue 1, pp 391–406

[26] A. Haungs et al.
KASCADE: Astrophysical results and tests of hadronic interaction models
Nuclear Physics B (Proc. Suppl.) 151 (2006) 167–174

[27] A. Aab
Spectral calibration of the fluorescence telescopes of the Pierre Auger Observatory
Astroparticle Physics, vol 95, Oct. 2017, Pages 44-56.

[28] O. Adriani et al.
The PAMELA Mission: Heralding a new era in precision cosmic ray physics
Physics Reports, Volume 544, Issue 4, 30 November 2014, Pages 323-370

[29] E. S. Seo et al.
CREAM: 70 days of flight from 2 launches in Antarctica
Advances in Space Research, 42, 1656-1663, 2008

[30] J. Chang et al.
An excess of cosmic ray electrons at energies of 300-800 GeV
Nature 456, 362-365 (20 November 2008) — doi:10.1038/nature07477

[31] Y. Asaoka et al.
Energy calibration of CALET onboard the International Space Station
Astroparticle Physics 91 (2017) 1–10

[32] A. D. Panov et al.
Energy spectra of abundant nuclei of primary cosmic rays from the data of ATIC-2 experiment: Final results
Bulletin of the Russian Academy of Sciences: Physics May 2009, Volume 73, Issue 5, pp 564–567.

[33] Y. Shikaze et al.
Measurements of 0.2–20 GeV/n cosmic-ray proton and helium spectra from 1997 through 2002 with the BESS spectrometer
Astroparticle Physics Volume 28, Issue 1, September 2007, Pages 154-167

[34] Y.S. Yoon et al.
Proton and Helium Spectra from the CREAM-III Flight
The Astrophysical Journal, Volume 839, Number 1.

[35] Y.S. Yoon et al.
Cosmic-ray proton and helium spectra from the first CREAM flight
The Astrophysical Journal, 728:122 (8pp), 2011 February 20,

[36] O. Adriani et al.
PAMELA Measurements of Cosmic-Ray Proton and Helium Spectra
Science 01 Apr 2011, Vol. 332, Issue 6025, pp. 69-72, DOI: 10.1126/science.1199172

[37] M. Aguilar et al.
Precision Measurement of the Proton Flux in Primary Cosmic Rays from Rigidity 1 GV to 1.8 TV with the Alpha Magnetic Spectrometer on the International Space Station
PRL 114, 171103 (2015)

[38] M. Aguilar et al.
Precision Measurement of the Helium Flux in Primary Cosmic Rays of Rigidities 1.9 GV to 3 TV with the Alpha Magnetic Spectrometer on the International Space Station
PRL 115, 211101 (2015)

[39] Pasquale Blasi, Elena Amato and Pasquale D. Serpico
Spectral Breaks as a Signature of Cosmic Ray Induced Turbulence in the Galaxy.
PRL 109, 061101 (2012)

[40] S. Abdollahi et al.
Cosmic-ray electron-positron spectrum from 7 GeV to 2 TeV with the Fermi Large Area Telescope
PHYSICAL REVIEW D 95, 082007 (2017)

[41] M. Aguilar et al.
Electron and Positron Fluxes in Primary Cosmic Rays Measured with the Alpha Magnetic Spectrometer on the International Space Station
PRL 113, 121102 (2014).

[42] F. Aharonian et al.
Probing the ATIC peak in the cosmic-ray electron spectrum with H.E.S.S.
AA, Volume 508, Number 2, December III 2009, https://doi.org/10.1051/0004-6361/200913323

[43] M. Aguilar et al.
Precision Measurement of the Boron to Carbon Flux Ratio in Cosmic Rays from 1.9 GV to 2.6 TV with the Alpha Magnetic Spectrometer on the International

Space Station
Phys. Rev. Lett. 117, 231102

[44] R. Cowsik, B. Burch, and T. Madziwa-Nussinov
The origin of the spectral intensities of cosmic-ray positron
The Astrophysical Journal, Volume 786, Number 2, doi:10.1088/0004-637X/786/2/124

[45] C. D. Orth et al.
Abundances and spectra for cosmic-ray nuclei from lithium to iron for 2 to 150 GeV per nucleon
Astrophys. J. 226, 1147 (1978), doi:10.1086/156692

[46] J. J. Engelmann et al.
Charge composition and energy spectra of cosmic-ray nuclei for elements from Be to NI - Results from HEAO-3-C2
Astron. Astrophys. 233, 96 (1990)

[47] W. R. Webber et al.
Cosmic ray isotope measurements with a new Cerenkov X total energy telescope
In NASA. Goddard Space Flight Center 19th Intern. Cosmic Ray Conf., Vol. 2 p 88-91 (SEE N85-34006 22-93)

[48] Aguilar, M. et al.
Relative Composition and Energy Spectra of Light Nuclei in Cosmic Rays: Results from AMS-01
The Astrophysical Journal, Volume 724, Issue 1, pp. 329-340 (2010), doi:10.1088/0004-637X/724/1/329

[49] A. D. Panov et al.
Relative abundances of cosmic ray nuclei B-C-N-O in the energy region from 10 GeV/n to 300 GeV/n. Results from ATIC-2 (the science flight of ATIC)
Proceedings of the 30th International Cosmic Ray Conference. July 3 - 11, 2007

[50] Ahn, H. S. et al.
Measurements of cosmic-ray secondary nuclei at high energies with the first flight of the CREAM balloon-borne experiment
Astropart. Phys. 30, 133 (2008)

[51] O. Adriani et al.
Measurement of boron and carbon fluxes in cosmic rays with the PAMELA experiment
The Astrophysical Journal, Volume 791, Number 2

[52] A. N. Kolmogorov
Dissipation of energy in the locally isotropic turbulence
Mathematical and Physical Sciences, Vol. 434, No. 1890

[53] O. Adriani et al.
An anomalous positron abundance in cosmic rays with energies 1.5 - 100 GeV
Nature 458, 607-609 (2 April 2009) — doi:10.1038/nature07942

[54] M. Aguilar et al.
Electron and Positron Fluxes in Primary Cosmic Rays Measured with the Alpha Magnetic Spectrometer on the International Space Station.
PRL 113, 121102 (2014)

[55] Beatty JJ et al.
New measurement of the cosmic-ray positron fraction from 5 to 15 GeV.
Phys Rev Lett. 2004 Dec 10;93(24):241102

[56] I. V. Moskalenko, A. W. Strong
Production and propagation of cosmic-ray positrons and electrons
Astrophys. J. 493, 694 (1998)

[57] A. Ibarra et al.
INDIRECT SEARCHES FOR DECAYING DARK MATTER
Int. J. Mod. Phys. A 28, 1330040 (2013)

[58] D. Gaggero et a.
Three-Dimensional Model of Cosmic-Ray Lepton Propagation Reproduces Data from the Alpha Magnetic Spectrometer on the International Space Station
Phys. Rev. Lett. 111, 021102

[59] P. Yin et al.
Pulsar interpretation for the AMS-02 result
Phys. Rev. D 88, 023001

[60] M. Aguilar et al.
Antiproton Flux, Antiproton-to-Proton Flux Ratio, and Properties of Elementary Particle Fluxes in Primary Cosmic Rays Measured with the Alpha Magnetic Spectrometer on the International Space Station
PRL 117, 091103 (2016)

[61] S. Torii for the CALET collaboration
The CALorimetric Electron Telescope (CALET): High Energy Astroparticle Physics Observatory on the International Space Station
PoS(ICRC2015)581

[62] O. Adriani et al.
Calet upper limits on X-ray and gamma-ray counterparts of GW 151226
Astrophysical Journal Letters, Volume 829, Issue 1, 20 September 2016, Article number L20

[63] Yuki Shimizu
The CALET CHD for determination of nuclear charge.
ICRC 2011, Beijing

[64] P.S. Marrocchesi et al.
Beam test performance of a scintillator-based detector for the charge identification of relativistic ions
Nuclear Instruments and Methods in Physics Research A 659 (2011) 477–483

[65] I. Daijito el al.
High-dynamic range readout system using dual APD/PD for the CALET-TASC
ICRC 2011, Beijing

[66] P. Brogi et al.
CALET measurements with cosmic nuclei: expected performances of tracking and charge identification
The 34th International Cosmic Ray Conference (ICRC2015)

[67] Taro Yamashita et al.
Performance of 64-multi-anode photomultiplier and scintillating fibre for the CALET detector
28th International Cosmic Ray Conference

[68] T.Tamura et al.
Development of a PMT Readout System with Viking Chips for the SciFi Detector of CALET
28th International Cosmic Ray Conference

[69] J.D. Sullivan et al.
Geometrical factor and directional response of single and multi-element particle telescope.
Nuclear instruments and methods 95, 1971, 097 5-11

[70] K. Kasahara
Proc. of 24th International Cosmic Ray Conference (Rome, Italy), Vol. 1 (1995) 399;
"EPICS Home Page" http://cosmos.n.kanagawa-u.ac.jp/EPICSHome/.

[71] K. Yoshida
The science objectives for CALET
ICRC2011, Beijing

[72] H. Motz
CALET's Sensitivity to Dark Matter and Astrophysical Sources
PoS(ICRC2015)1194

[73] S. Agostinelli et al.
Geant4 a simulation toolkit
Nuclear Instruments and Methods in Physics Research Section A, Volume 506, Issue 3, 1 July 2003, Pages 250-303

[74] G. Battistoni et al.
Overview of the FLUKA code
Annals of Nuclear Energy 82, 10-18 (2015)

[75] Francesco Palma
Study of the performance of the CALET calorimeter-based orbital observatory for High-Energy Astroparticle Physics
Ph.D. thesis, University of Roma Tor Vergata", XXV cycle, 2011-2012.

[76] GEANT4 website, Physics Reference Manual
"http://geant4.web.cern.ch/geant4/UserDocumentation/UsersGuides/PhysicsReferenceManual/BackupVersions/V10.1/fo/PhysicsReferenceManual.pdf"

[77] B.Andersson et al.
A model for low-pT hadronic reactions with generalizations to hadron-nucleus and nucleus-nucleus collisions.
Nuclear Physics B, Volume 281, Issues 1–2, 19 January 1987, Pages 289-309

[78] H.W. Bertini, M.P. Guthrie
News item results from medium-energy intranuclear-cascade calculation
Nucl.Phys. A169 (1971) 670-672, DOI: 10.1016/0375-9474(71)90710-X

[79] S. Roesler, R. Engel, J. Ranft
The Monte Carlo Event Generator DPMJET-III
doi: 10.1007/978-3-642-18211-2˙166

[80] L. Pacini et al.
Capability of electron identification for the CALET measurement.
ICRC2017, 163 (2017).

[81] R.Frühwirth
Application of Kalman filtering to track and vertex fitting
Nucl. Instr. and Meth. A, 262 (1987), 444-450

[82] P. Maestro, N. Mori
Particle tracking in the CALET experiment
PoS(ICRC2017)

[83] Christian W. Fabjan and Fabiola Gianotti
Calorimetry for particle physics.
Reviews of modern physics, Vol 75, Oct. 2003

[84] C. Clopper and E. S. Pearson
The use of confidence or fiducial limits illustrated in the case of the binomial
Biometrika. 26: 404–413. doi:10.1093/biomet/26.4.404

[85] A. Hoecker et al.
TMVA 4, Toolkit for Multivariate Data Analysis with ROOT, Users Guide
arXiv:physics/0703039, CERN-OPEN-2007-007

[86] F. Palma et al.(CALET Collaboration),
Simulation studies of the expected proton rejection capabilities of CALET
PoS(ICRC2015)1196.

[87] R. Brun, F. Rademakers
ROOT - An Object Oriented Data Analysis Framework
Nucl. Inst. and Meth. in Phys. Res. A 389 (1997) 81-86.

[88] O. Adriani et al.
Energy Spectrum of Cosmic-ray Electron + Positron from 10 GeV to 3 TeV Observed with the Calorimetric Electron Telescope on the International Space Station.
PRL 119, 181101 (2017).

[89] Y. Akaike et al.
CALET observational performance expected by CERN beam test.
Proc. of 33rd international cosmic ray conference (ICRC2013) 726 (2013).

[90] M. Ackermann et al.
In-flight measurement of the absolute energy scale of the Fermi Large Area Telescope
Astroparticle Physics, Volume 35, Issue 6, p. 346-353., DOI 10.1016/j.astropartphys.2011.10.007

[91] M. Honda et al.
New calculation of the atmospheric neutrino flux in a three-dimensional scheme
Physical Review D 70, 043008 (2004). DOI https://doi.org/10.1103/PhysRevD.70.043008

[92] E. Thébault et al.,
International Geomagnetic Reference Field: the 12th generation
Earth, Planets and Space 67:79 (2015), https://doi.org/10.1186/s40623-015-0228-9

[93] O. Adriani et al.
Ten years of PAMELA in space
La Rivista del Nuovo Cimento, vol. 40, N. 10, DOI: 10.1393/ncr/i2017-10140-x